New Silicon Nanocrystal Materials for Photovoltaic Applications

Dissertation
zur Erlangung des akademischen Grades

doctor rerum naturalium (Dr. rer. nat.)

seit 1558

vorgelegt dem Rat der Physikalisch-Astronomischen Fakultät
der Friedrich-Schiller-Universität Jena

von Dipl.-Phys. Charlotte Weiss
geboren am 05.12.1985

1. Gutachter:

Prof. Dr. rer. nat. Carsten Ronning (Friedrich-Schiller-Universität Jena)

2. Gutachter:

Prof. Dr. rer. nat. Stefan Glunz (Albert-Ludwigs-Universität Freiburg)

3. Gutachter:

Prof. Dr. rer. nat. Klaus Lips (Freie Universität Berlin)

Tag der Disputation: 31.01.2017

Contents

Introduction

The *Paris Agreement* adopted during the *2015 United Nations Climate Change Conference* (UNCCC) reinforces the long-term temperature goal of "*holding the increase in the global average temperature to well below 2°C above pre-industrial levels and pursuing efforts to limit the temperature increase to 1.5°C above pre-industrial levels, recognizing that this would significantly reduce the risks and impacts of climate change*" [1]. This proves that the world community is aware of the danger that the effects of climate change represent for the planet. The reason for this recognition is probably the increasing occurrence of extreme weather events such as hot extremes, precipitations and droughts [2]. Furthermore, there is mounting evidence suggesting that extreme weather events may have already contributed to armed-conflict outbreaks [3] such as the droughts in Syria and Somalia and the subsequent civil wars in both countries [4–6].

Despite the good intentions of the participants of the UNCCC, only the nationally determined contributions and their implementation will demonstrate if there is a chance to maintain the 1.5°C or at least the 2°C goal [2]. However, without doubt the currently installed and planned unmitigated coal-fired power generation capacities are inconsistent even with a well below 2°C limit [7,8]. Therefore, the changeover to renewable energies must take place as fast as possible. Not considering nuclear energy as it implies unpredictable risks and costs for humanity, electrical energy must be obtained from biomass, water, wind, geothermal heat and from solar radiation. Each of these technologies show their own characteristics in terms of favorable location, further increases in efficiency and up-scaling. The generation of electrical energy with solar cells (SC) is easily scalable, does not necessarily need a central power grid, is safe for flora and fauna and the resources for SC production are available in large quantities. However, the improvement of SC has come to the point where the theoretical limit of efficiency – the so-called Shockley Queisser limit – has nearly been reached. For Si based SC with a band gap $E_\mathrm{G} = 1.1\,\mathrm{eV}$ this maximum efficiency is $\eta = 29.43\%$ [9]. The reason for this limitation is schematically depicted in Fig. 1 (a). Conventional SC with a single band gap do not absorb photons with energies below E_G (transmission losses, red), whereas light with shorter wavelengths cannot be entirely transformed to electricity due to thermalization losses (blue). Thus, only a part (green) of the terrestrial solar spectrum can be converted to electrical power. The so called "third generation" SC overcome this efficiency limit by applying new cell concepts, as discussed by Green [10] and Würfel [11].

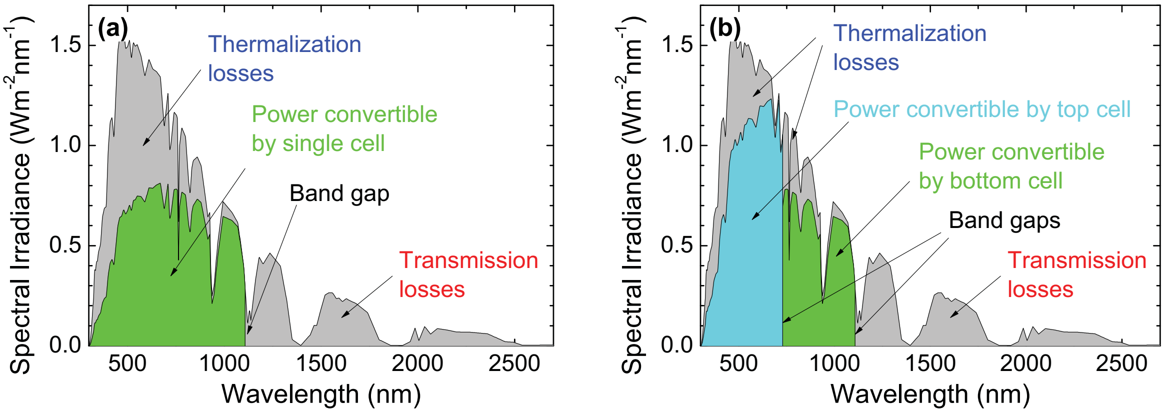

Figure 1: Terrestrial solar spectrum with maximum convertible part (green) for a single Si solar cells (a) (after Glunz *et al.* [12]) and a tandem on Si solar cell (b). The grey parts of the spectrum cannot be converted to electricity due to thermalization of electron-hole pairs in the high energy range and due to transmission of photons in the low energy range.

The only new concept which has been realized so far is the multi-junction SC where single cells with different band gaps are combined, for example by stacking them on top of each other. These cells must exhibit decreasing bandgaps from the illuminated side to the rear side to convert different wavelength ranges of the solar spectrum, minimizing thermalization and transmission losses [13], as demonstrated in Fig. 1 (b) for a two bandgap (tandem) SC. For this concept, the theoretical efficiency limit rises to $\eta = 42.5\%$ for tandem SC with optimized bandgaps [10]. The best multi-junction cells consist of III-V semiconductors and reach efficiencies of more than 38.8% under one sun [14]. However, their production is very cost-intensive and their application is therefore restricted to space applications and to concentrator systems [15]. Lower-cost multi-junction SC have been realized by a system of amorphous and microcrystalline Si (a-Si/μc-Si), showing efficiencies only up to $\eta = 13.6\%$, but which lies above the corresponding efficiencies of a-Si and μc-Si single junction cells [14]. This material is already widely used in Si tandem photovoltaics [16, 17]. However, these cells show poor carrier mobility and suffer from light-induced degradation [18]. Thus, a Si-based but more stable material system is of great interest.

A tandem cell with a bottom cell of conventional crystalline bulk Si and a top cell with a higher band gap of silicon nanocrystals (NC) embedded in a dielectric matrix represents a potential material system. Such a structure is sketched in Fig. 2. The ideal bandgap for a top cell on a crystalline Si (1.1 eV) bottom cell was calculated to be 1.7 eV [19]. This can be achieved in Si with the help of the quantum confinement effect [20], which means enlarging the Si bandgap by reduction of the Si crystals to the nano-scale. Due to

Heisenbergs' uncertainty principle, which states an increasingly undefined momentum for increasingly confined position, a transition from indirect to direct bandgap behavior and therefore enhanced absorption is expected from Si when downscaled to the nm range.

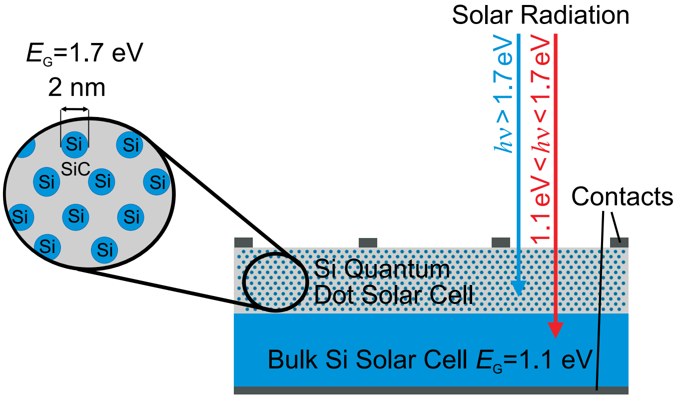

Figure 2: Schematic sketch of a Si-based tandem solar cell with a crystalline bulk Si solar cell as bottom cell and with Si nanocrystals embedded in a SiC matrix as top cell. The Si nanocrystals show a higher bandgap than bulk Si due to quantum confinement. Therefore, the top cell absorbs shorter wavelength and transmits longer wavelength, which are absorbed by the bottom cell.

Experimentally, a transition from indirect to quasi-direct behavior was observed by Hartel *et al.* for Si NC in SiO_2 [21, 22]. Not only the size of the NC, but also the band structure of the embedding dielectric matrix material and the interdot distance determine the properties of the Si NC [23]. Different review articles about the characterization of Si NC embedded in the technologically relevant matrices SiC, Si_3N_4 and SiO_2 and their characterization on material and on device level were published [24–26]. Here only the most relevant aspects for this thesis will be summarized.

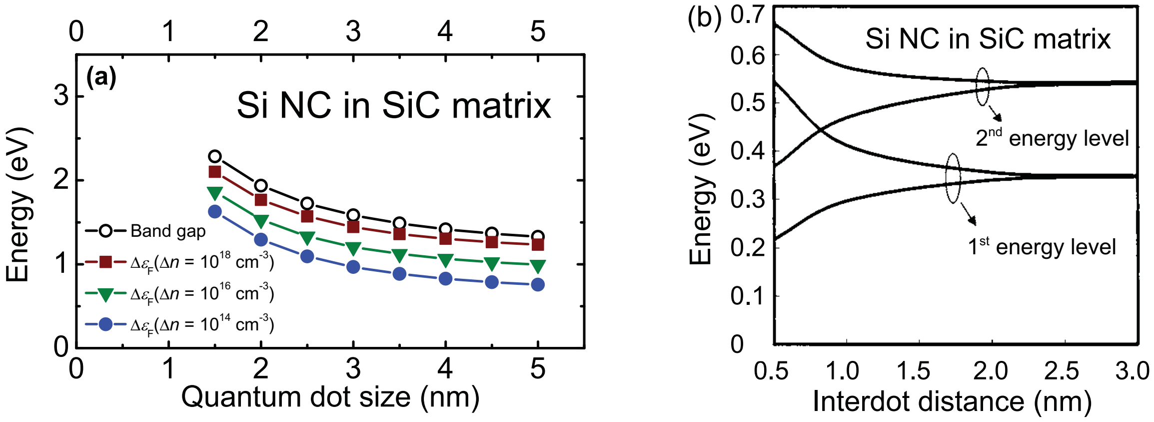

Figure 3: (a) Calculation of the quasi-Fermi level splitting $\Delta\epsilon_F$ for different Si excess carrier densities Δn (coloured) and the bandgap (black) of Si nanocrystals with an interdot distance of 2 nm embedded in a SiC matrix as a function of the nanocrystal size (after [27]). (b) Calculation of the position and bandwidth of the first two conductions bands in 2 x 2 x 2 nm^3 Si nanocrystals embedded in SiC as a function of the interdot distance (after [23]).

Several groups use 3C-SiC as a matrix material since it provides a small conduction band offset of 0.5 eV compared with other typical matrix materials (1.9 eV for Si_3N_4 or 3.2 eV for SiO_2 [20]), with the same trend expected for the valence band. A small band offset increases the tunneling probability from one Si NC to the other and hence the conductivity of the material, making transport less sensitive to variations in NC separation [20, 23]. On the other hand, a small band offset decreases the confinement efficiency, but is still high enough to result in the ideal bandgap of 1.7 eV as calculated by Löper *et al.* [27] and depicted in Fig. 3 (a) for Si NC with an interdot distance of 2 nm in a SiC matrix. The coloured lines represent the quasi-Fermi level splitting $\Delta\epsilon_F$ for different excess carrier densities Δn, whereas the black line represents the bandgap. The calculation suggests that a Si NC size of 2...3 nm corresponds to the ideal bandgap of 1.7 eV. This is assumed to be valid for a wide interdot range due to simulations of Jiang *et al.* [23] which show an influence of the interdot distance of Si NC in SiC mainly on the bandwidth and less on the bandgap. This is shown in Fig. 3 (b) for $2 \times 2 \times 2\,nm^3$ Si NC in SiC for the first two conduction bands. These show significant broadening for decreasing NC sizes without notable energy shift. Another advantage of SiC as matrix material compared to the insulators Si_3N_4 of SiO_2 is that it can contribute to the absorption of the sunlight, since it has a bandgap of only 2.3 eV.

The so-called multilayer (ML) approach has been developed to reach Si NC size control for the adjustment of the Si bandgap (see Fig. 4 (a)).

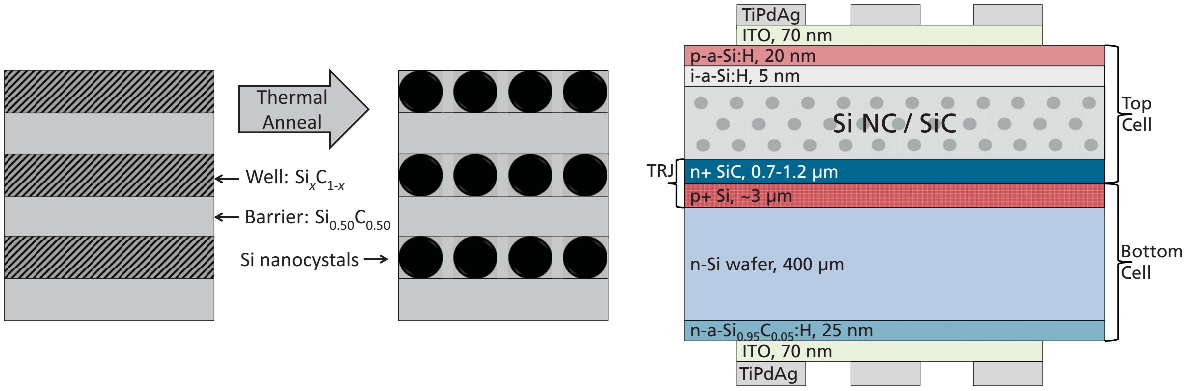

Figure 4: (a) The multilayer approach: A stack of SiC/Si_xC_{1-x} bilayers are deposited and annealed. Ideally, Si_xC_{1-x} sublayer thickness controls Si nanocrystal size, while the SiC sublayer thickness has no effect on crystallization. (b) Structure of the first all-Si tandem solar cell with Si nanocrystal top cell. After Schnabel *et al.* [28].

Alternating layers of stoichiometric SiC barriers (SiC) and Si rich SiC wells (SRC) with thicknesses in the range of 1...10 nm are deposited. Typically the deposition is performed by plasma enhanced chemical vapour deposition (PECVD) [29–31], but also magnetron sputtering [32, 33] is reported or – in the case of SiO_2/SiO_x ML – by evaporation of SiO powder [34]. In all cases, it follows an annealing step typically at 1100°C, either by furnace anneal [29–31, 33, 34] or by rapid thermal annealing [35, 36]. Chen *et al.* [37] give an

up-to-date overview of all groups reporting on Si NC embedded in a dielectric matrix with the corresponding deposition and annealing methods.
During the annealing step, phase separation and Si NC formation are expected to occur in the SRC layers while the SiC layers should serve as diffusion barrier. Furthermore, the annealing causes hydrogen (H) effusion as the films are usually deposited from the precursor gases SiH_4 and CH_4 (e.g. [38, 39]). The ML approach is known to work very well for Si NC size control in SiO_2 [24, 40, 41], but is much more challenging in SiC because interdiffusion of the SiC and the SRC layer occurs [29, 33, 42, 43]. In addition, co-crystallization of Si and SiC NC was observed [33, 35, 38, 39, 44–48]. It was only recently that Summonte *et al.* [29] managed to obtain size-controlled Si NC in SiC by optimizing the ML parameters. Using transmission electron microscope (TEM) images, they proved that for an as-deposited SRC thickness between 3 and 4 nm, the ML structure survives the annealing for 3 nm and 9 nm thick SiC barrier layers. In the case of the 3 nm barrier layers, no size controlled Si NC were achieved, but either a continuous crystallized well (for 4 nm SRC) or an outgrowth of the Si NC in the barrier layers was observed (for 3 nm SRC). For the thicker barrier of 9 nm, both outgrowth and continuous crystallization were less pronounced, but it could still not be excluded that the Si NC touch each other. An interconnection of the Si NC seems probable because the Si content in the SRC layers is quite high ($x = 0.85$). However, the authors claim that separated, ordered Si NC should be achieved for a certain combination of Si content and thickness of the SRC layers.

Recently, the first all-Si tandem SC with a Si NC top cell absorber (Fig. 4 (b)) based on the ML from Summonte *et al.* [29] was presented. The device shows tandem SC characteristics, but low efficiency and no clear evidence of quantum confinement [28]. Therefore, further investigation of Si NC in SiC is necessary and this thesis is focusing on this. The main reason for the poor Si NC/SiC material quality are the high defect and interface density due to H effusion and co-crystallization during annealing [30]. The high defect densities must be strongly reduced in order to develop a good absorber material for SC. This thesis proposes two alternative approaches for defect reduction. The first one aims to **prevent the SiC crystallization** to reduce the interfaces and stress in the material. Successful reduction of the SiC crystallinity is reported either by reduction of the thermal budget [35] or by the incorporation of O [49] or N [50] atoms during layer deposition. Both methods will be applied in this thesis. The second attempt to reduce the defect density in Si NC/SiC layers is by **H passivation**. H passivation is reported to work well for Si NC/SiO_2 [51, 52] layers, but turns out to be much less effective in Si NC/SiC material systems [53]. The only group that report successful H passivation of Si NC/SiC layers works on samples with a significant O content and only at low annealing temperatures (900°C), where crystallization is still incomplete [54, 55].

The indispensable precondition for material improvement is an in-depth material characterization. Therefore, this work focuses on the **structural characterization** of $\mathrm{Si}_x\mathrm{C}_{1\text{-}x}$ in order to understand and control the crystallization mechanism. Reliable evaluation procedures for grazing incidence X-ray diffraction (GIXRD), Fourier transform infrared spectroscopy (FTIR), and Raman spectroscopy will be introduced and discussed to obtain complementary information about Si/SiC NC size and crystallinity. These results are completed by **optical methods**: Photoluminscence spectroscopy (PL) and spectrophotometry. These are used to evaluate the relation between structure and absorption behavior in terms of band structure and defects. The advantage of all mentioned characterization methods is that they yield averaged information over a macroscopic sample area and depth.

This work continues a series of Ph.D. theses on Si NC/SiC systems completed at the *Fraunhofer ISE*: First, M. Künle [56] developed the $\mathrm{Si}_x\mathrm{C}_{1\text{-}x}$ layers for Si NC/SiC systems and characterized their structure. Then P. Löper [57] developed a membrane device to examine the SC application relevant electrical properties of Si NC single and multilayer. Finally, M. Schnabel [58] realized the first crystalline all Si tandem SC. This revealed that the next step must be an improvement of the material in terms of defect reduction. This in turn requires a better understanding of the processes during annealing. Therefore, characterization and understanding of the crystallization process and defect reduction are the main challenges of this work, rather than building complete solar cells or improving any given efficiency.

Thus, the **main tasks of this thesis** are:

1. Deposition of $\mathrm{Si}_x\mathrm{C}_{1\text{-}x}$ singlelayers and $\mathrm{Si}_x\mathrm{C}_{1\text{-}x}/\mathrm{Si}_{0.50}\mathrm{C}_{0.50}$ multilayers with varying Si contents.
2. Si NC formation in SiC matrix by temperature treatment in a wide parameter range.
3. Comprehensive structural and optical characterization of Si NC/SiC samples.
4. Deeper understanding of Si/SiC co-crystallization process.
5. Reduction of SiC crystallinity.
6. Si NC size control.
7. Defect reduction by H passivation or O incorporation.

Chapter 1

Background

Firstly, we introduce the effect of quantum confinement, which represents the motivation for the growth of Si nanocrystals in SiC. A description of the most important properties of Si and SiC in their crystalline and their amorphous state follows. The classical crystallization theory is outlined in terms of nucleation and crystal growth and the experimental accessible quantity of transformed crystalline fraction is also introduced. Against this background, the expectations regarding Si and SiC crystallization are formulated.

1.1 Quantum confinement in nanocrystals

If a solid material is spatially limited by interfaces with other materials or by surfaces, its properties change from that of a solid material of infinite extension [59]. Drastic changes of the properties occur if the size of the material in one, two or three spatial directions gets smaller than the de Broglie wavelength of the particles in the material, e.g. the electrons. In this case, spatial confinement occurs in one, two or three directions. The spatial confinement influences the movement of the electrons in the material and therefore the distribution of the allowed energy bands. The confinement of an electron with effective mass m^* at the position $\vec{x}$ in the material can be described by the stationary Schrödinger equation

$$\left[-\frac{\hbar^2}{2m^*}\Delta_{\vec{x}} + V_{\mathrm{conf}}(\vec{x})\right]\phi(\vec{x}) = \epsilon\phi(\vec{x}). \tag{1.1}$$

Thereby, V_{conf} describes the potential, which leads to the spatial confinement, ϵ are the allowed energies of the electrons and $\phi(\vec{x})$ are the electrons' wave functions. In the case of 3D confinement – which means quantum dots (QD) – the allowed energies become infinitely narrow energy levels. This can be characterized with three quantum numbers

n, m, l ($\epsilon = \epsilon_{nml}$). With the definition of the density of states $D(\epsilon)$ to be the sum over all Dirac functions at the allowed energy states, we get the case for 3D confinement

$$D(\epsilon) = 2 \sum_{n,m,l} \delta(\epsilon - \epsilon_{nml}). \tag{1.2}$$

This means that the spatial confinement in QD leads to discrete contribution of electronic states. If the size of the QD in x, y and z directions is d and the potential well is of infinite height,

$$V_{\text{conf}} = \begin{cases} 0 & \text{for} \qquad -\frac{d}{2} < x, y, z < \frac{d}{2} \\ \infty & \text{otherwise} \end{cases} \tag{1.3}$$

we deal with the well-known problem of an electron in a box with the following solution for the electronic states:

$$\epsilon_{n,m,l} = \frac{\hbar^2}{2m^*} \left(\frac{\pi}{d}\right)^2 [n^2 + m^2 + l^2]. \tag{1.4}$$

The QD consist of confined electrons and holes in Si nanocrystals (NC) embedded in dielectric SiC for this thesis. The potential well occurs due to the fact that the SiC bandgap (E_G(SiC) $= 2.3\,$eV) is larger than the Si bandgap (E_G(Si) $= 1.1\,$eV). This situation is depicted schematically for one dimension in Fig. 1.1 (a).

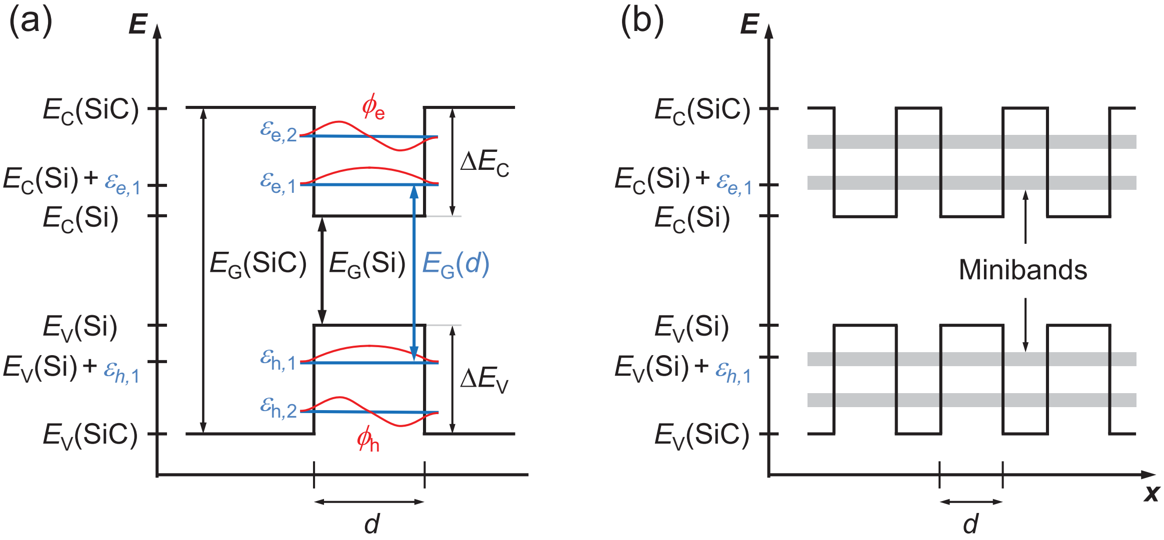

Figure 1.1: Schematic band diagrams of Si QD in a SiC matrix. In (a), the quantum confinement effect is illustrated. In (b), the formation of minibands due to a series of Si QD is sketched.

The band diagram shows the conduction and valence band edges for SiC ($E_{\text{C/V}}$(SiC)) and Si ($E_{\text{C/V}}$(Si)), the first two energy levels due to quantum confinement for electrons ($\epsilon_{\text{e},1/2}$) and holes ($\epsilon_{\text{h},1/2}$) and the corresponding electron and hole wave functions (ϕ_e and ϕ_h). The fact that $\epsilon_{\text{e},1}$ lies above E_C(Si) and $\epsilon_{\text{h},1}$ lies below E_V(Si) leads to an enlarged bandgap, which depends on the QD size d

$$E_{\mathrm{G}}(d) = E_{\mathrm{G}} + \frac{\hbar^2}{2}\left[\frac{1}{m^*_{\mathrm{C}}} + \frac{1}{m^*_{\mathrm{V}}}\right]\left(\frac{\pi}{d}\right)^2, \tag{1.5}$$

where m^*_{C} and m^*_{V} are the effective masses of electrons and holes in the conduction and the valence band, respectively. This effect allows bandgap engineering by specifically changing d.

For Eq. 1.4 and 1.5, we assumed infinite quantum wells for simplicity, but the complete confinement of the wave functions inside the quantum well would mean that no conduction through the material is possible. The finite height of $\Delta E_{\mathrm{C/V}}$ leads to an exponentially decaying penetration of the wave function into the potential barrier, as shown in Fig. 1.1 (a). If the QD lie close enough together, the penetrating wave functions can superpose each other and build so-called minibands, as depicted in Fig. 1.1 (b). These minibands can enhance the conductivity of the material significantly.

1.2 Si and SiC

1.2.1 Properties of Si and SiC

Si crystallises in the face-centered cubic structure with the base $\{(0,0,0),\ ({}^1/_4,{}^1/_4,{}^1/_4)\}$, which is called the diamond structure and depicted in Fig. 1.2 (a). In the case of 3C-SiC (also called β-SiC), the crystalline structure is the same as for Si, but half of the Si atoms are replaced by carbon (C) atoms. This is called the zinc blende structure, depicted in Fig. 1.2 (b).

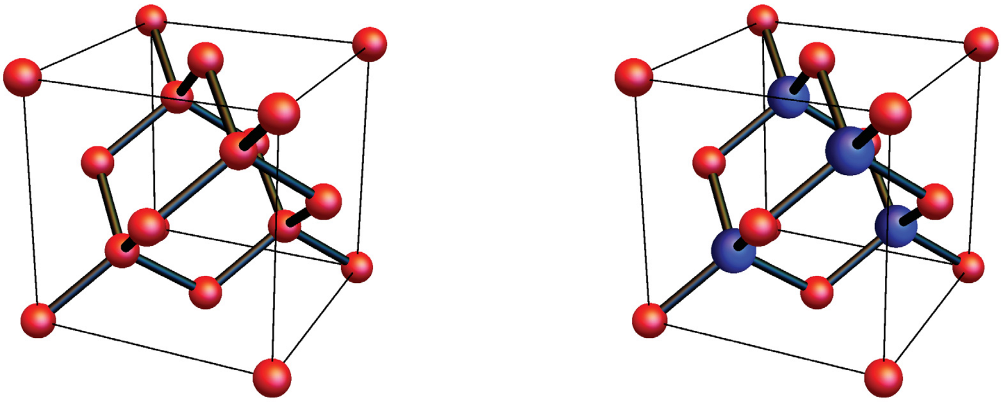

Figure 1.2: The diamond crystal structure of Si (a). The zinc blende crystal structure of SiC (b). All Si atoms are depicted in red whereas all C atoms are depicted in blue.

3C-SiC is only one of more than 200 polytypes of SiC, which differ strongly in their properties. All of them are known for their high hardness (number 9.2...9.3 in Mohs scale [60]) and strong chemical resistance [61]. Only the properties of 3C-SiC are important for this thesis, as listed in Table 1.1. A summary of the properties of other SiC polytypes are given for example in the review of W. Wesch [61] or in the book by G. Harris [62].

Table 1.1: List of important parameters of Si and SiC in the crystalline and the amorphous state. For well-known textbook values, no specific reference is given.

	c-Si	**a-Si**	**3C-SiC**	**a-SiC**
Bandgap (eV)	1.1	1.6...1.8 [18, 63]	2.3	~ 2.6 eV [64]
Melting Point (°C)	1414 [65]	1147 [66]	decomposition at 2545 [67]	-
Density (g/cm^3)	2.33 (solid) 2.57 (liquid)	2.30 (1000°C)	3.21	2.5 ± 0.1 [68]
Molar mass (g/mol)	28.09	28.09	40.1	40.1
Lattice constant (Å)	5.43	-	4.36	-
Refractive index at 2 eV	4.2 [69]	3.3 [70]	2.64 [62]	3.05 [71] (a-SiC) 2.55 [68] (a-SiC:H)
Thermal conductivity (W/cm K)	1.56 [72]	0.007 [72]	5.0 [61]	1.3 - 1.6 [73]
Heat capacity (J/g K)	0.71 [72]	0.77 [72]	0.67 [74]	0.7 (poly SiC) [75]

The bandgap of 3C-SiC is significantly higher than the bandgap of c-Si. Therefore, quantum confinement is expected to occur in the Si NC/SiC-matrix system. In contrast to Si, SiC shows no liquid phase, but dissociate above a certain temperature. SiC has a higher density and molar mass than Si, due to the small C atoms filling the space between the Si atoms. The lattice constant between c-Si and 3C-SiC differ significantly. This leads to strain and defects at interfaces if both phases crystallize next to each other. Although c-Si is a good heat conductor, the thermal conductivity of 3C-SiC is even higher.

Some representative values for the amorphous Si and SiC (a-Si and a-SiC) phases are additionally listed in Table 1.1. At low temperatures, a-Si and a-SiC are usually hydrogenated (see next paragraph). The values for a-Si and a-SiC can serve as a comparison between the amorphous and the crystalline phase, but cannot be treated as material constants because a-Si and a-SiC properties vary with the structural properties of the material. These are closely related to the deposition method, the deposition parameters, and the H content (cf. references in Table 1.1).

Here we want to comment on some significant differences between amorphous and crystalline Si/SiC phases. The indicated bandgaps of a-Si and a-SiC are larger than for crystalline Si and SiC. This widening of the bandgap is mainly caused by the Si-H$_n$ and

C-H_n bonds in the network as calculated e.g. by Robertson *et al.* [76]. In this publication, a number of references can be found, which proof the relation between the hydrogen (H) content and the bandgap experimentally. When talking about the bandgap, one has to keep in mind that there is no well-defined crystalline structure in amorphous semiconductors. The bandgap of an amorphous semiconductor depends on the short range order – that is the coordination number, the chemical bond type, bond length, bond angle and so on [76]. This explains why there is no distinct but instead a range of bandgap values for a-SiC and a-Si.

A comparison of the refractive constants reveals that the difference between a-SiC and 3C-SiC is smaller than in case of a-Si/c-Si. This reflects the fact that the optical properties of Si in the visible spectrum range differ much more as a function of the structure than the optical properties of SiC.

1.2.2 Production of Si and SiC

High-purity c-Si for electronic applications is mostly produced by bulk crystal growth methods either with the help of the Czochralski process (CZ Si) or by the Float zone process (FZ Si) [77]. The epitaxial layer growth of Si by chemical vapour deposition (CVD) is also possible, but of small importance for the Si industry [77]. Precisely the opposite is true for SiC. Bulk crystal growth is possible, but epitaxial layer growth by CVD is mostly used [61].

The amorphous material is deposited either by PECVD from the precursor gases SiH_4 and CH_4 (e.g. [18, 78, 79]) or by sputtering (e.g. [80]). These deposition methods lead to hydrogenated a-Si (a-Si:H) and a-SiC (a-SiC:H). Unhydrogenated a-Si and a-SiC can be produced by a subsequent annealing step for H effusion and amorphisation by high energy irradiation [79] or by high energy irradiation of c-Si [66, 81] and c-SiC [71, 82, 83]. It is possible to deposit a-$Si_xC_{1\text{-}x}$:H alloys of any desired composition by PECVD or sputtering (e.g. [84–86]). This is not possible for crystalline material due to the SiC phase diagram, which shows that Si and C is practically not soluble in SiC [67].

The properties of a-$Si_xC_{1\text{-}x}$:H are even more difficult to define than the properties of a-Si and a-SiC because they depend on the amount of H, on the density of the films, on the deposition conditions and on the Si/C composition. For the a-$Si_xC_{1\text{-}x}$:H deposited in this work, one can use the properties of a-Si/a-SiC/c-Si and 3C-SiC as rough indications, but the only reliable values are the ones, which are accessible experimentally for each individual process.

1.3 Classical crystallization theory

The following short introduction into the classical crystallization theory is based on the book from K. Meyer [87]. An amorphous solid can be considered as undercooled melt [87]. Therefore, the classical nucleation theory, which describes the phase transition from the liquid to the crystalline phase, can be used to describe the crystallization process of a-$\mathrm{Si}_x\mathrm{C}_{1\text{-}x}$:H samples.

1.3.1 Nucleation

The driving force of crystallization is the reduction of the free enthalpy, also called Gibbs energy ΔG of the system. In principle, at temperatures below the melting point T_S, the transformation from amorphous to crystalline phase is always connected with a reduction in Gibbs energy of ΔG_V. However, a certain undercooling $\Delta T = T_\mathrm{S} - T$ is necessary for nucleation. The reason for this is the formation of an interface between the old and the new phase, and the introduction of a misfit strain in the system – both related to a increase in Gibbs energy of ΔG_I for the interface and ΔG_M for the misfit. It follows for ΔG of the complete system:

$$\Delta G = -\Delta G_\mathrm{V} + \Delta G_\mathrm{I} + \Delta G_\mathrm{M} \tag{1.6}$$

ΔG_M plays an important role in nucleation in crystals, but can be neglected for nucleation in melt and is therefore not considered in classical nucleation theory. No general statement about ΔG_M is possible for amorphous to crystalline transitions. But in the case of a-Si crystallization, it can be neglected [88]. Therefore, ΔG_M will not be considered further in this section. ΔG_V is proportional to the volume and ΔG_I is proportional to the surface of the crystalline particle. When we consider a spherical particle with radius r, Eq. 1.6 becomes

$$\Delta G(r) = -\frac{4}{3}\pi r^3 \Delta g_\mathrm{V} + 4\pi r^2 \sigma, \tag{1.7}$$

where σ is the free interface enthalpy between the melt and the crystal and Δg_V is the change in free volume enthalpy at the phase transition. Δg_V can also be expressed with the help of T_S, the melting enthalpy $\Delta_\mathrm{S} H$ and ΔT, leading to the expression

$$\Delta G(r) = -\frac{4}{3}\pi r^3 \Delta_\mathrm{S} H \frac{\Delta T}{T_\mathrm{S}} + 4\pi r^2 \sigma. \tag{1.8}$$

The function $\Delta G(r)$ has a maximum at the so-called **critical nucleus radius** r^*

$$r^* = \frac{2\sigma T_\mathrm{S}}{\Delta_\mathrm{S} H \Delta T} \quad \text{with} \quad \Delta G(r^*) = \Delta G^* = \frac{16\pi\sigma^3 T_\mathrm{S}^2}{3(\Delta_\mathrm{S} H \Delta T)^2}, \tag{1.9}$$

where ΔG^* is the **critical free activation energy of nucleus formation**. If the radius of a particle is of subcritical size ($r < r^*$), it costs energy to increase the size of the particle. Whereas if the particle is of supercritical size ($r > r^*$), energy is released if the particle grows further. In the latter case, the particle is called nucleus. We see from Eq. 1.9 that for decreasing ΔT, which corresponds to increasing annealing temperatures, r^* and ΔG^* increases, which means that nucleation decreases. This can be expressed with the help of the **nucleation rate per unit volume** υ_N. The probability for particles to overcome ΔG^* can be described by the Boltzmann statistics. However, this is not the only energy barrier, which must be taken into account to describe the nucleation rate. One also has to consider the diffusion barrier ΔG_D. This leads to the expression

$$\upsilon_\mathrm{N} = \upsilon_{\mathrm{N}0} e^{-(\Delta G^* - \Delta G_\mathrm{D})/k_\mathrm{B} T}, \tag{1.10}$$

where $\upsilon_{\mathrm{N}0}$ is the temperature-independent nucleation rate and k_B is the Boltzmann constant. We know from Eq. 1.9 that ΔG^* decreases with increasing ΔT whereas ΔG_D increases with increasing ΔT because diffusion obeys the Arrhenius law. This leads to the characteristic of the $\upsilon_\mathrm{N}(\Delta T)$ curve – depicted in cyan in Fig. 1.3.

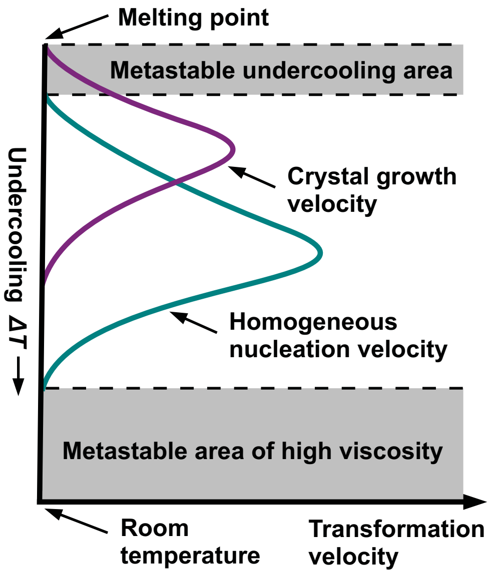

Figure 1.3: Basic curve shape of nucleation velocity (υ_N, cyan) and growth velocity (υ_G, purple) as a function of undercooling ΔT (from [87]).

Starting from the melting point, no nucleation occurs for small ΔT because the formation of a new interface would increase the overall Gibbs energy of the system. At higher ΔT, the energy gain of the amorphous to crystalline phase transition overcomes the energy loss due to interface formation and nucleation starts. The nucleation rate increases with increasing ΔT and reaches a maximum value. For lower temperatures, nucleation is hindered by the decreasing diffusion in the system and the nucleation rate decreases again. The nucleation process described so far is referred to as **homogeneous nucleation**. The second possible nucleation process is called **heterogeneous nucleation** and occurs at discontinuities such as precipitates, interfaces, extended defects and impurities – hereafter called surfaces. These discontinuities have a catalytic effect on nucleation if the **critical free activation energy of heterogeneous nucleus formation** (ΔG^*_{H}) is smaller than ΔG^*. This is the case if the wetting angle of contact on the surface is smaller than 180°, which is true if the crystalline phase wets the surface. In other words, heterogeneous nucleation catalyzes homogeneous nucleation because less energy-intensive interfaces must be built due to the additional surface.

1.3.2 Crystal growth

The **crystal growth rate per unit volume** v_{G} shows the same characteristic as v_{N} only with the **free activation energy for crystal growth** ΔG_{G} instead of ΔG^*:

$$v_{\mathrm{G}} = v_{\mathrm{G0}} e^{-(\Delta G_{\mathrm{G}} - \Delta G_{\mathrm{D}})/k_{\mathrm{B}}T}, \tag{1.11}$$

where v_{G0} is the temperature-independent growth velocity. Usually $\Delta G_{\mathrm{G}} < \Delta G^*$ because the further grow of an existing surface is less energy-intensive than the formation of a new surface. This explains why crystal growth starts directly below the melting point (purple curve in Fig. 1.3). Strictly speaking, the diffusion barrier from the matrix to a subcritical particles during nucleation (ΔG^N_{D}) can differ from the diffusion from the matrix to a crystal during crystal growth (ΔG^G_{D}). However, both are reported to be in the same order of magnitude [88] and therefore considered as equal (ΔG_{D}) in this work.

Experimentally, it is difficult to distinguish between v_{N} and v_{G}. The combination of both leads to the velocity of amorphous to crystalline phase transformation, expressed as transformation rate per unit volume v with the effective activation energy Q, which depends on ΔG_{G}, ΔG_{D} and ΔG^* and with the temperature-independent growth velocity v_0:

$$v = v_0 e^{-Q(\Delta G_{\mathrm{G}}, \Delta G_{\mathrm{D}}, \Delta G^*)/k_{\mathrm{B}}T}. \tag{1.12}$$

This is still not necessarily a measurable quantity, as it is only a thermodynamic consideration for an infinite volume of amorphous phase. As a real measurable quantity, one therefore introduces the **transformed crystalline fraction** f, which is defined as the ratio between the crystalline volume (V_{cryst}) and the total volume (V_{tot}) of a crystallising phase [89]. Its time development can be described with the general expression of the *Johnson-Mehl-Avrami* equation for isothermal crystallization processes:

$$f = 1 - \mathrm{e}^{-At^n}. \tag{1.13}$$

In general, the parameter A depends on v_{N} and v_{N} and therefore on Q. Q in turn as well as n depend on time and temperature. If the mode of nucleation and growth is known, the determination of A and n allows an analytical description of the crystallization process [89]. Little is still known about these processes in $\mathrm{Si}_x\mathrm{C}_{1\text{-}x}$ samples, which are furthermore expected to by highly complex because the exact structure of the amorphous material is not known and due to the co-crystallization of Si and SiC. Therefore, a detailed analysis is not possible. However, Eq. 1.13 will be used for a rough estimation of Q in Sec. 4.2.

Ostwald ripening

The term Ostwald ripening describes an annealing effect in polycrystalline material [90]. Small crystallites shrink whereas large crystallites grow further for long annealing times. The driving force of Ostwald ripening is energy minimisation by interface reduction. If the crystallites of element A are surrounded by the matrix material B, the large crystallites are surrounded by a larger depletion area of element A than the smaller crystallites. Therefore, a diffusion current of element A occurs from the smaller towards the larger crystals. Lifshitz and Slyozov [91] derived the average crystallite radius to be proportional to the third root of the annealing time $r \propto t^{\frac{1}{3}}$ under the following conditions: The volume fraction of the crystallites is low, the crystallites are spherical and do not touch each other. Furthermore, mass transport only occurs via diffusion through the matrix and diffusion occurs in a steady-state regime. Finally, the matrix is considered as stress free.

Grain distribution

The grain size distribution resulting from classical nucleation theory complies with the following rules [92, 93]: At low annealing temperatures, thus at high ΔT, r^* is small and the growth rate is low. This leads to the formation of small, slowly growing grains. The formation and growth continue until all amorphous phase is transformed into the crystalline phase. Neglecting the effect of Ostwald ripening, a low temperature annealing leads to a high number of small grains. In the case of high annealing temperatures, which corresponds to low ΔT, r^* is large and the growth rate is high. If all amorphous phase is crystallised, the resulting structure contains a low number of large grains. In both processes a crystalline fraction of 100% is reached, whereby the corresponding annealing time is shorter for high temperature anneal than for low temperature anneal.

Expectation regarding Si/SiC crystallization

The idea of growing Si NC in an amorphous SiC matrix via solid phase crystallization is based on the fact that the melting point of Si ($T_{\mathrm{T}}^{\mathrm{Si}} = 1414°\mathrm{C}$ [65]) is far below the decomposition temperature of SiC ($T_{\mathrm{T}}^{\mathrm{SiC}} = 2545°\mathrm{C}$ [67]). Consequently, one can expect the onset of Si crystallization at lower temperatures than the onset of SiC crystallization. This seems even more plausible with a view to the individual a-Si and a-SiC systems described in literature. For the formation of c-Si from a-Si:H, an activation energy of 2.7 eV was reported by Olson *et al.* [94], and Wu *et al.* [95] reported a nucleation energy of 3.9 eV and a growth energy of 3.2 eV. Much higher activation energies of respectively 5.2 eV [79] and 5.0 eV [96] were reported for unhydrogenated and sputtered a-SiC. However, reviewing the literature shows that the results from the individual systems a-Si and c-SiC cannot be transferred directly to $\mathrm{Si}_x\mathrm{C}_{1\text{-}x}$ layers. A co-crystallization of Si NC and SiC NC at temperatures between the temperature expected for c-Si and c-SiC formation is reported by many groups [29, 35, 49, 97].

Chapter 2

Experimental

All steps included in sample preparation, from cleaning via plasma enhanced chemical vapour deposition to the different annealing methods (furnace annealing (FA), rapid thermal annealing (RTA), zone melting recrystallization (ZMR), and flash lamp annealing (FLA)), and the subsequent hydrogen passivation by forming gas anneal (FGA) and remote plasma H passivation (RPHP) are described below. The wet chemical cleaning was done by the cleanroom staff from Fraunhofer ISE. The establishment of FA, RTA and ZMR was carried out in collaboration and within the scope of the bachelor thesis of M. Rumpel [98], the master thesis of A. Reichert [99] and the bachelor thesis of T. Fehrenbach [100], which were supervised in the framework of this Ph.D. thesis. FLA was done by Dr. S. Prucnal from Helmholz-Zentrum Dresden-Rossendorf. FGA and RPHP were done at Fraunhofer ISE by H. Steidl and F. Feldmann. Then, two optical and standard characterization methods (photoluminescence spectroscopy and spectrophotometry) which were used in this work are described.

2.1 Sample preparation

Two types of substrates were used for layer deposition: (i) 250 μm thick p-doped FZ Si, (100)-oriented with a resistivity of 10 Ωcm ($\approx 1 \cdot 10^{15}$ cm^{-3}). These samples were subsequently characterized by grazing incidence X-ray diffraction (GIXRD), Fourier transform infrared spectroscopy (FTIR), and photoluminescence (PL) measurements. (ii) 1 mm thick fused silica (Suprasil®1) substrates were used for subsequent spectrophotometry and Raman measurements. Both types of substrates were cleaned in hot HNO_3 and dilute HF prior to film deposition. The fused silica was subjected to an additional cleaning step of hot HCl/H_2O_2 solution followed by a second HF etching step before film deposition.
All multilayer (ML) and singlelayer (SL) samples used in this work were deposited by

plasma-enhanced chemical vapor deposition (PECVD) conducted in a *Roth&Rau* AK400 reactor. The pressure during deposition was kept at 0.3 mbar and the substrate temperature at 270°C. The plasma power density was 100 mW/cm^2 at a frequency of 13.56 MHz. The variation of the gas fluxes of SiH_4, CH_4 and H_2 allows the deposition of hydrogenated a-SiC (a-$Si_xC_{1\text{-}x}$:H) with varying stoichiometry. The three different layer compositions used in this work were determined by Rutherford Backscattering Spectrometry with an accuracy of 1% [57] and are listed in Tab. 2.1 with the associated gas fluxes.

Table 2.1: Reactant gas fluxes used for PECVD in sccm.

Layer type	SiH_4	CH_4	H_2
Stoichiometric SiC a-$Si_{0.50}C_{0.50}$:H	7	60	100
Si rich SiC 1 a-$Si_{0.63}C_{0.37}$:H	7	20	100
Si rich SiC 2 a-$Si_{0.77}C_{0.23}$:H	10	10	100

The development of the deposition parameters used in this work was done in the framework of the thesis of M. Künle [56]. The reader is referred to this work for further details about PECVD deposition of a-$Si_xC_{1\text{-}x}$:H layers.

2.2 Annealing

2.2.1 Furnace annealing (FA)

The inside of the furnace is metal free and therefore the setup can be used to anneal samples for photovoltaic applications. The advantage of FA compared to the other annealing methods used is the possibility to anneal samples on FZ Si and samples on quartz substrates in one run under very similar annealing conditions. The maximum annealing temperature in the FA setup is 1100°C, which can be kept for 30 min. At lower annealing temperatures, annealing times of several hours are possible. A sketch of the FA setup is depicted in Fig. 2.1. The annealing process takes place in a quartz tube of 140 cm length and a diameter of 16 cm. The samples are placed upright in a quartz carrier, which stands on a quartz plate, which lies on a U-shaped quartz pipe at the bottom of the quartz tube. The quartz tube is surrounded by a heating coil, regulated by three temperature controllers with three thermocouples TC_L (left), TC_M (middle) and TC_R (right). This leads to a wide area with a homogeneous temperature where up to 40 samples can be annealed at once. The sample temperature is monitored by another thermocouple TC_{ex}, which is placed in a extra pipe underneath the samples. The tuning of the heating ramp is done via TC_{M} and therefore a calibration between TC_{M} and TC_{ex} was necessary. The temperature calibration curves and further details about the FA process and the FA setup can be found in the bachelor thesis by M. Rumpel [98].

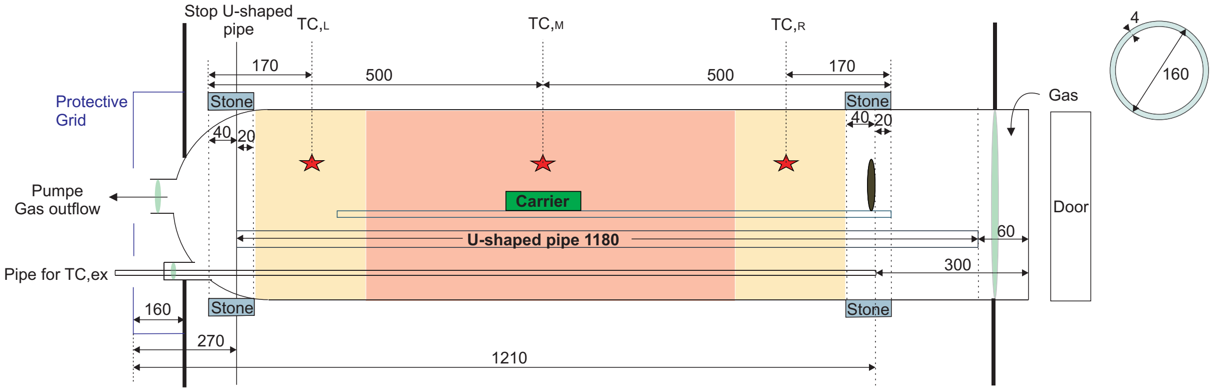

Figure 2.1: Sketch of the FA setup. All values are given in cm.

A typical annealing process was conducted as follows: After placing the samples in the quartz tube, the interior of the quartz tube was pumped down to about $2{\cdot}10^{-5}$ mbar. Then a cleaning step at 150°C for 30 min was done under vacuum conditions in order to remove H_2O molecules from the tube walls and the samples. Then the desired annealing temperature was reached with a heating ramp of 10°C/min under an N_2 flow of 10 slm. After the annealing time, the heating was switched off and the samples cooled down to room temperature inside the furnace under N_2 flow.

2.2.2 Rapid thermal annealing (RTA)

By RTA, the same temperatures can be reached as by FA with significantly higher heating rates. However, the maximum annealing times are much shorter for RTA than for FA processes and lie usually in the range of a few seconds up to several minutes.

RTA was conducted in an *RTP Sol Invictus 156 PV* tool from *Centrotherm*, which was put into operation specifically for this work. The samples were placed on a 4" FZ Si support wafer on a four point quartz sample holder in a quartz chamber. Only one sample can be annealed in one run. The front side of the samples are heated by the halogen lamp field located above. The RTA setup is equipped with a pyrometer for temperature monitoring, which points towards the FZ Si support wafer. As the temperature of the support wafer is not necessarily the sample's temperature, a calibration between the pyrometer temperatures and the sample's surface temperatures was necessary for both substrate types. This was done by bonding an S-type thermocouple to the sample surface with the help of the ceramic adhesive *Cerastil V-336*. The temperature calibration was

done for samples on quartz and on FZ Si substrate separately. All RTA processes were completed with a heating rate of 50°C/s under an N_2 flow of 5 slm.
The temperature calibration curves and further details about the RTA process and the RTA setup can be found in the master thesis of A. Reichert [99].

2.2.3 Zone melting recrystallization (ZMR)

The ZMR setup *ZMR100* was developed at *Fraunhofer ISE* for recrystallization of microcrystalline Si deposited by chemical vapor deposition (CVD) [101, 102]. Samples in the ZMR setup can be heated optically to more than 1400°C. The setup features a lamp array for back side heating and a lamp surrounded by a focusing elliptical reflector for front side heating. With the focused lamp, zone melting processes can be realised. As zone melting processes are not the topic of this work, they will not be considered further. The back side lamp array consists of 12 halogen lamps with a power of 4.5 kW each. Above the lamp field, a quartz tube is mounted wherein a quartz plate serves as sample holder. In order to reduce the differences in heating-up behavior of samples on FZ Si substrate and samples on quartz substrate, the samples were placed on a ceramic plate on top of the quartz sample holder. In one run, two samples on Si FZ or two samples on quartz substrate were annealed at once. Whereas the quartz tube with the samples is stationary, the furnace is movable and can be centered relative to the samples with the help of a CCD camera in the housing of the furnace. Ar with a flux of 10 slm was chosen as annealing gas in contrast to N_2 in FA and RTA because a strong incorporation of N into the samples during ZMR annealing under N_2 gas at temperatures $\geq$ 1200°C was observed [99].
The ZMR is controlled by varying the lamp power. Therefore, an individual temperature calibration for both substrate types is necessary. This was done by bonding an S-type thermocouple to the sample surface with the help of the ceramic adhesive *Cerastil V-336*, analogously to RTA temperature calibration. In this way, the desired annealing temperatures were assigned to certain lamp powers and the heating curve for every annealing temperature was determined. Additionally, the heating curve resulting from the maximum power of the lamp field was measured.
On the basis of this temperature calibration, the annealing processes were as follows: In order to keep the heating-up period as short as possible, every annealing process was started with the maximum lamp power and switched to the distinct lamp power for the particular annealing temperature just before this temperature was reached.
In the bachelor thesis of T. Fehrenbach [100], the temperature calibration curves, a detailed description of the ZMR setup, sketches of the sample arrangement and a list of all annealing parameters used in this work can be found.

The interest of using ZMR additionally to RTA lies in the fact that higher temperatures and longer annealing times can be realised with this method. The disadvantage is the contamination of the ZMR setup with impurity atoms. Therefore, no FTIR measurements were possible because they require low-doped substrates. For all other structural measurements conducted during this work, the contamination of the ZMR samples showed no influence.

2.2.4 Flash lamp annealing (FLA)

The FLA setup used in this work was described by Prucnal *et al.* [103]. The setup features an RTA system for back side preheating and an FLA system for front side heating. The RTA system consists of halogen lamps and can reach a maximum temperature of approximately 950°C for silicon wafers. The FLA system is equipped with Xe lamps and can reach temperatures above 1400°C for annealing times between 0.8 and 20 ms. A special reflector is mounted above the Xe lamps to ensure a homogeneous temperature distribution across the sample surface. The spectrum of the Xe lamps used for this experiment has its maximum intensity between 400 and 600 nm (see Fig. 4.23). FLA was performed under Ar flow and for films grown on Si substrates only. The preanneal step was performed at temperatures between 600 and 800°C for 2, 3 or 4 min. For the subsequent FLA step, flash energies ranging from 34 up to 62 $\mathrm{J/cm^2}$ were applied for 20 ms. Because of the short pulse times, direct temperature measurements during the flash are not possible [104], but a change in FLA energy of 7 $\mathrm{J/cm^2}$ corresponds to a change in surface temperature of $\approx$ 100°C.

2.3 Hydrogen (H) passivation

H passivation was conducted either by forming gas anneal (FGA) for 60min@500°C in a quartz furnace with a gas mixture of 95% N_2 and 5% H_2 or by remote plasma H passivation (RPHP) for 90min@450°C. The FGA parameters were adopted from SiO_2 passivation [105], whereas a RPHP temperature of $\approx$ 400°C was reported to be appropriate for the passivation of Si-rich oxycarbides [54].

2.4 Optical characterization methods

2.4.1 Photoluminescence (PL) spectroscopy

PL spectroscopy is widely used to determine the band gap energy and the energetic position of radiative defect levels in semiconductors. The sample is irradiated by monochromatic light of wavelength λ ($hc/\lambda > E_{\mathrm{G}}$) and the resulting luminescence spectrum gives information about the band structure of the sample.

PL measurements on $\mathrm{Si}_x\mathrm{C}_{1\text{-}x}$ samples are particularly challenging because the quantum yield of annealed $\mathrm{Si}_x\mathrm{C}_{1\text{-}x}$ samples is very low [53,106] due to the very small carrier lifetimes. Therefore, a lot of work was done in our group to establish a highly sensitive PL setup (see App. 3) in the framework of the Ph.D. thesis of M. Schnabel [58]. A comprehensive description of the PL setup, the measurement procedure and the data analysis is given therein, whereas the corresponding PL results can be found in two journal publications [107,108]. One important result was the observation that the PL light generated in the samples is modulated by **Fabry-Pérot interferences** (because the $\mathrm{Si}_x\mathrm{C}_{1\text{-}x}$ layer thickness corresponds to an optical path length in the optical wavelength range). Schnabel [58] recommended to estimate the influence of interferences on a distinct PL spectra by comparing it with the transmittance (%T) (or reflectance (%R)) spectrum of the sample. If the modulation of the PL spectrum is the same (or opposite) as the modulation of the %T (or %R) spectrum, the PL peak position should not be evaluated without any correction. If the %T (or %R) spectra show a different shape than the PL spectra, the influence of interferences can be neglected.

A new laser with $\lambda = 405\,\mathrm{nm}$ with a beam size of $\approx 4.5\,\mathrm{mm}$ (DLM-405NL-200 from *EksmaOptics*) was used due to it's stronger absorption in the samples compared to the lasers used in Schnabel's work [58]. Unfortunately, the wavelength range between 405 nm and 550 nm could not be exploited because a 550 nm long-pass (LP) filter had to be used to shield the detector from the stray light of the laser. LP filters with shorter cut-off wavelengths were tested, but the filters themselves showed PL signal with higher intensities than the $\mathrm{Si}_x\mathrm{C}_{1\text{-}x}$ samples.

The PL light from the samples was focused on an *Andor Shamrock* 202i spectrometer, where it was dispersed by a grating with 300 lines/mm. The spectra were acquired between 400 and 1000 nm with a charge-coupled device (CCD) detector (DU401A-BRDD from *Andor*), which was thermoelectrically cooled-down to -95°C. To acquire the whole wavelength range, the grating had to change its position three times to measure four overlapping parts of the spectra, which were subsequently put together by the software. All PL measurements were done at room temperature after an HF cleaning step of the samples. During this

work, only samples on Si substrates were measured for two reasons. First, as no laser light is transmitted through the Si substrate, the problem of producing additional PL signal behind the sample is circumvented. Second, Schnabel reported that the disturbing influence of Fabry-Pérot interferences on the PL spectra is less pronounced in samples prepared on Si substrates compared to samples prepared on quartz substrate due to the smaller difference in refractive indices between substrate and $\mathrm{Si}_x\mathrm{C}_{1\text{-}x}$ layer [58, 107].
The **measuring routine** was the following: 1. Laser beam alignment with GaInP reference sample, as described by Schnabel [58]. 2. Taking a spectrum with blocked laser beam and a spectrum of the "empty" beam path to ensure the absence of a PL signal from the environment. 3. Mounting the HF cleaned sample and looking for a spot on the surface without dust particles or cracks with the help of the CCD camera using the spectrometer as a mirror. 4. Measurement with the following parameter: 2500 μm input slit width (wider than reported by Schnabel) – 60 s integration time per grating position (corresponds to 4 min acquisition time per spectrum) – 0.04 mA laser current (corresponds to $\approx$ 13 mW).
The **data analysis routing** was the following: 1. Subtraction of the laser-bocked PL spectrum from the PL spectrum of the sample. 2. Wavelength correction with the laser wavelength as reference. 3. Plotting PL spectra together with the reflectance spectra to check to which extent the Fabry-Pérot interferences influence the PL spectrum.
In contrast to the data treatment by Schnabel [58], neither an intensity correction nor a multiplication with the transfer function (which takes into account the wavelength dependency of the detectors' sensitivity and the reflectance of the collecting and dispersing optics) was done. The intensity correction is not necessary for the new laser, whereas the transfer function was not available for the new setup. Therefore, a systematic underestimation of all PL signal for $\lambda > 950$ nm must be take into account.

2.4.2 Spectrophotometry

The spectrophotometry (R&T) spectra of the samples in the UV-Vis wavelength range (250-1000 nm) were measured using a *Varian Cary 500i* photo spectrometer with an Ulbricht sphere. An example of R&T data from an as-deposited $\mathrm{Si}_{0.77}\mathrm{C}_{0.23}$ sample is plotted in Fig. 2.2 (a). Pronounced thin-film interference maxima and minima occur in the R&T data. If the sample thickness s is known, the absorption coefficient α can be calculated from R&T measurements by means of the following relation:

$$\alpha = \frac{\ln(\frac{1-R}{T})}{s}. \tag{2.1}$$

Due to internal reflection, the effective distance covered by the light in the layer is longer than s. Therefore, Eq. 2.1 leads to a systematic overestimation of α. Nevertheless, this method allows a comparison of α in samples series. The α spectrum is plotted in Fig. 2.2 (b) for the a-$Si_{0.77}C_{0.23}$:H example. To avoid a distortion of the α spectrum by the interferences, R&T data must be acquired at exactly the same position of the sample because the smallest difference in samples thickness will lead to a displacement of the R&T interference peaks relative to each other and therefore to a distortion of the α curve. For this work, a special mounting was constructed for the spectrometer to assure an accurate positioning of the samples.

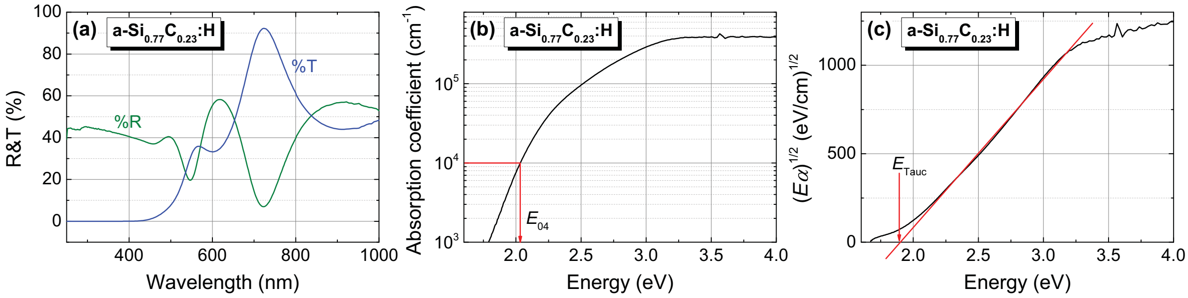

Figure 2.2: Example of an R&T measurement of an a-$Si_{0.77}C_{0.23}$:H sample (a), the absorption coefficient α derived from the R&T measurement (b) and the corresponding Tauc plot to determine the bandgap E_{Tauc} (c).

There are two common ways two determine a value for the effective bandgap from R&T measurements: The Tauc bandgap E_{Tauc} and the so-called E_{04} bandgap. Both values are useful to compare samples properties, but should not detract from the fact that in amorphous semiconductors there is no precise location of the gap because the band tail density of states decays continuously with energy [18]. One method was developed by Tauc *et al.* [109] for amorphous Ge, which is therefore referred to as "Tauc plot". An extrapolation of the density of states is performed by a linear fit of the plot of $(E\alpha)^{1/2}$ over the energy E. The intercept of the fit with the x-axes gives a value for the bandgap (E_{Tauc}). This method is demonstrated in Fig. 2.2 (c). The deviation of the Tauc plot from its linear shape at low energies results from the exponential energy dependence of the optical absorption in the vicinity of the band gap energy – the so-called Urbach tails – which are observed in all amorphous semiconductors [18]. If the Tauc plot shows no linear region, for example because the sample is not completely amorphous, it is still possible to determine the E_{04} bandgap, which corresponds to an α of $1{\cdot}10^4\,\mathrm{cm}^{-1}$ (see Fig. 2.2 (b)). This example shows that E_{Tauc} and E_{04} are close but not equal. This is important to have in mind when comparing literature bandgap values.

Finally, the term "bandgap" is used in this work for simplicity, understanding well that in most cases the term "mobility gap" would be more suitable due to the pronounced tail states in the material.

Chapter 3

Adaptation of structural measurements to nanomaterial

An essential requirement for the understanding and controlling of the crystallization process in $Si_xC_{1\text{-}x}$ *samples is their comprehensive structural characterization. For this purpose, grazing incidence X-ray diffraction (GIXRD), Fourier transform infrared spectroscopy (FTIR), and Raman spectroscopy complement each other especially well. All three methods yield statistically relevant bulk information of the samples. GIXRD gives an estimation of SiC and Si nanocrystal sizes whereas FTIR allows a quantification of the SiC crystallinity and Raman of the Si crystallinity. The effort undertaken for a successful application and reproducible analysis of these three methods is presented in this chapter. The GIXRD setup was aligned and the signal to noise ratio significantly improved. A reproducible background correction and fitting algorithm leads to very reliable results. New FTIR and Raman analysis were adopted from literature and established in the form of Mathematica® programs with the assistance of A. Reichert, as described in detail in his master thesis [99]. Furthermore, the accuracy of all three methods will be discussed. Parts of the analysis procedures were published in references [44, 45].*

3.1 Grazing incidence X-ray diffraction (GIXRD)

3.1.1 Basics of XRD measurements

For detailed insight into the principles of X-ray diffraction, the reader is referred to standard literature like *X-Ray Diffraction in Crystals, Imperfect Crystals, and Amorphous Bodies* from Guinier *et al.* [110]. The short introduction given in this section is based on this book.

Structural analysis by X-ray diffraction is based on the fact that the wavelength of X-rays and the structural size of crystalline solids are both in the range of some Ångström. Therefore, crystalline structures act as diffraction grating for X-rays and the resulting interference pattern allows conclusions about the underlying crystal structure. This can be demonstrated by the general relation for the diffracted amplitude of a group of atoms with the electron density $\rho(\vec{x})$:

$$A(\vec{s}) = \int \rho(\vec{x}) \exp(-2\pi i \vec{s}\vec{x}) d\nu_x, \tag{3.1}$$

where $\vec{x}$ and $\vec{s}$ define points in the object space and in reciprocal space, respectively, and the integration is carried out over the whole object space. This expression shows that the amplitude of the diffraction pattern is the Fourier transformation of the electron density. This means that in principle all information of the structure of an object is present in the diffracted amplitude. In reality, only the diffracted intensity can be observed in XRD measurements. In the case of a multicrystalline sample with a very large number of small crystals, whose orientations are perfectly isotropic, the intensity of a reflex as a function of the diffraction angle θ is called **Powder pattern** and given by the following equation:

$$I(\theta) = I_0\, r_e^2\, \frac{1+\cos^2 2\theta}{2} \frac{1}{16\pi\, x \sin^2\theta \cos\theta}\, \lambda^3\, F_{hkl}^2\, m\, \frac{1}{V_e^2}\, D\, dV. \tag{3.2}$$

I_0 is the intensity of the incident beam; $r_e = 2.8 \cdot 10^{-15}$ m is the classical radius of the electron; θ is the diffraction angle under which a reflex occurs, defined in Eq. 3.3; x is the distance from the sample; λ is the wavelength of the X-rays; F_{hkl} is the structure factor for the lattice plane (hkl) defined in Eq. 1 in App. 4; V_e is the volume of the unit cell of the crystal; D is the Debye-Waller factor, which takes into account the decrease of intensity with increasing temperature due to the vibration of the lattice; m is the multiplicity factor for the planes (hkl), which increases with increasing symmetry of the crystal system; dV is the volume of the diffracting crystals.

The diffraction angle can be deduced with the help of simple geometrical considerations on the reflection of X-rays at the lattice planes of a crystal leading to the well known **Bragg equation** for the prediction of constructive interference

$$2b \sin\theta = n\lambda, \qquad n = 1, 2, 3, ... \tag{3.3}$$

where b is the interplanar distance of the considered lattice planes and n is a positive integer. Every lattice plane can be characterized unambiguously by its **Miller indices** (hkl). The interplanar distance can be calculated from the Miller indices for cubic crystals with the lattice constant a:

$$b = \frac{a}{\sqrt{h^2 + k^2 + l^2}}. \tag{3.4}$$

Due to interference effects, only lattice planes with a non-vanishing structure factor F_{hkl} show reflexes in the powder pattern. The calculation of F_{hkl} for Si and SiC can be found in App. 4. All lattice planes of c-Si and 3C-SiC giving rise to reflexes in the measured range between 10° and 90° are listed in Table 3.1.

Table 3.1: List of all detection angles between 0° and 90° under which X-ray reflexes for c-Si and 3C-SiC are expected and their corresponding lattice planes. The 4H-SiC reflex under 34.8° is not the only possible 4H-SiC reflex in the measured range, but the only one observed during this work.

Phase	**hkl**	**2θ (°)**
c-Si	(111)	28.4
4H-SiC	(110)	34.8
3C-SiC	(111)	35.7
3C-SiC	(200)	41.4
c-Si	(220)	47.3
c-Si	(311)	56.1
3C-SiC	(220)	60.0
c-SiC	(400)	69.1
3C-SiC	(311)	71.8
c-Si	(331)	76.4
c-Si	(422)	88.0

The corresponding diffraction angles 2θ are calculated with Eq.s 3.3 and 3.4 for $a_{\mathrm{Si}} = 5.43\,\mathrm{Å}$, $a_{\mathrm{SiC}} = 4.36\,\mathrm{Å}$ and $\lambda = 1.5418\,\mathrm{Å}$. All predicted c-Si and 3C-SiC peaks were observed during this work. At very high annealing temperatures, the most intense reflex of the hexagonal 4H-SiC structure occurs and is therefore listed in Table 3.1 for completeness.

So far, only the **position of the reflexes** in the diffraction pattern were discussed, which show what kind of crystalline phases are present in a multicrystalline sample. The other important parameter is the **width of the reflexes**. Analogous to a diffraction grating, the position of the diffraction maximum depends only on the slit spacing and the width of the reflex decreases as the number of slits increases. In the case of X-rays, the distance of lattice planes corresponds to the slit spacing while the number of slits corresponds to the number of reflecting lattice planes and therefore the size of the crystallites d. The *Scherrer equation* [110] gives the relation between the full width at half maximum (FWHM) and d

$$d = \frac{K \cdot \lambda}{FWHM \cdot cos\theta} \tag{3.5}$$

where K is a form factor, which is 0.9 for spherical crystals in the cubic crystal system [111]. It should be emphasized that this size determination does not provide information on the grain size distribution and is therefore referred to as an estimation of the mean grain size.

3.1.2 Realization of GIXRD measurements

The dependency from $I(\theta)$ on dV in Eq. 3.2 explains the interest of GIXRD measurements for the investigation of NC. GIXRD increases the number of irradiated NC and therefore dV because the gracing angle of incidence ω leads to the radiation of a maximum volume in the thin layer as demonstrated in Fig. 3.1 (a) and Fig. 3.2. Whereas ω is kept constant, the detector scans over the diffraction angles $10° < 2\theta < 90°$. If the crystallites in the sample are randomly orientated, all reflexes of the powder pattern are detected by this method.

In this work, GIXRD was successfully established to determine the crystal phases present in the $Si_xC_{1\text{-}x}$ samples based on the positions of the reflexes, and to estimate the sizes of the NC in the different crystalline phases. The precondition for this analysis is a good signal to noise ratio in the GIXRD patterns. Taking a look at Eq. 3.2 again, one notices that the only accessible parameter to increase the intensity of the GIXRD pattern is I_0 and dV. Both parameters were improved significantly during this work by the careful choice and alignment of the optical components in the GIXRD setup and by the optimisation of the sample mounting and orientation. All GIXRD patterns were recorded using a *Philips X'Pert MRD* system equipped with a CuK_α X-ray source.

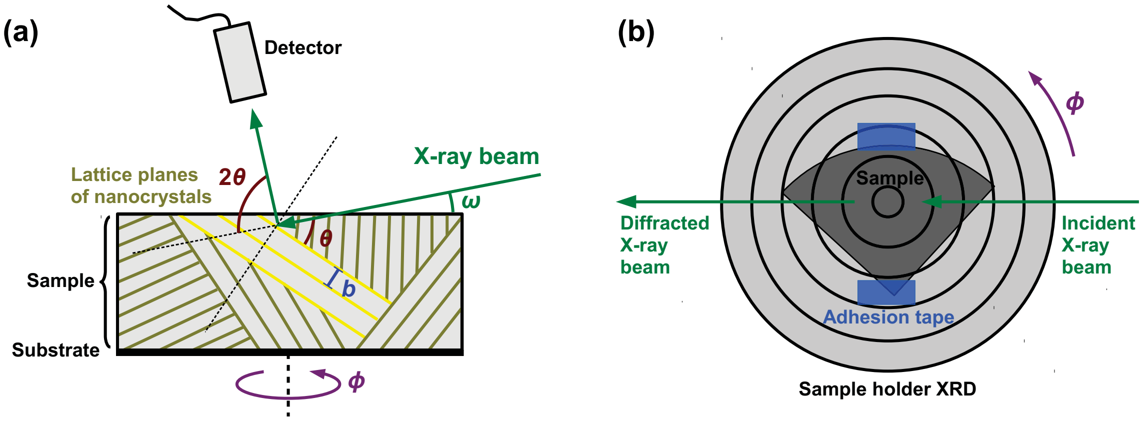

Figure 3.1: (a) The principle of GIXRD is illustrated: A X-ray beam hits the surface of a multicrystalline sample under a fixed small angle ω. The beam is diffracted at the randomly oriented lattice planes of the crystallites in the sample. The detector scans over the diffraction angles $10° < 2\theta < 90°$. If the orientations of the crystallites is perfectly isotropic, the diffraction pattern is independent from the ϕ orientation of the sample. (b) The mounting of the samples on the upright sample holder is sketched. The adhesion tape must be kept out of the beam path and the ϕ orientation must be chosen in a way to avoid a signal from the Si substrate in the measured patterns.

GIXRD setup: The GIXRD setup is sketched in Fig. 3.2. In the incident beam directly in front of the X-ray tube, a slit with an aperture of 1/16° was used for an optimal signal to noise ratio. For maximal X-ray intensity, only a mirror for parallelization of the beam was used as prefix module instead of a monochromator. In the diffracted beam, a parallel plate collimator with an aperture angle of 0.27° was mounted in front of the detector to select the X-rays diffracted under 2θ from the randomly scattered X-rays.

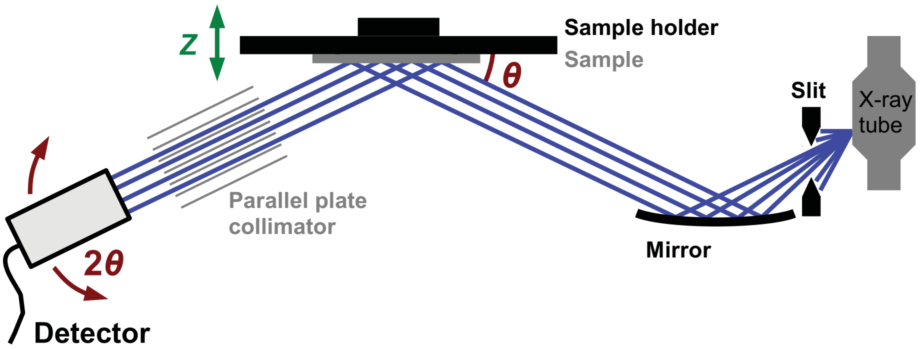

Figure 3.2: Sketch of the GIXRD setup.

Sample mounting: The sample holder and a sample are sketched in Fig. 3.1 (b). As the sample holder is upright, the samples must get attached to it as flatly as possible without irradiating the adhesion tape as it shows sharp X-ray reflexes. This defines a lower limit for the samples size, since the irradiated area on the samples is about 3 cm x 3 cm large. Due to the grazing angle used and due to the varying thickness of the samples, the Z-position (marked in Fig. 3.2) must be adjusted prior to each measurement. It turned out that a certain ϕ orientation of the sample must be chosen to avoid an unintended reflex from the substrate. A change in ϕ direction corresponds to a rotation in the plane perpendicular to the plane of incidence and therefore in the plane of the sample surface (see Fig. 3.1 (a) and (b)). The substrate peak is marked with a black circle in the green spectrum in Fig. 3.3 (b). It consists of a sharp peak at 51.7° and a broad peak around 56°. The sharp peak is attributed to the Si(311) planes of the Si substrate according to the following consideration: As sketched in Fig. 3.3 (a), the X-ray hits the sample surface and therefore also the substrate surface under the small angle ω. In the present experiment, $\omega = 0.65°$. As the substrate is (100)-oriented and the angle between the Si(100) and the Si(311) lattice planes is $\beta = 25.2°$, the incident angle of the beam to the Si(311) plane in the substrate is $\theta = \beta + \omega = 25.85°$. This matches exactly with the observed peak position at $2\theta = 51.7°$. Only the Si(311) lattice planes lead to a substrate peak in the GIXRD pattern because only the Si(311) lattice planes are hit by the grazing X-rays approximately under their Bragg angle θ. According to Eq. 3.3, this corresponds to an X-ray wavelength of 1.43 Å diffracted at the Si(311) lattice planes. The deviation from the used CuK$_\alpha$ line of $\lambda_{\mathrm{CuK}_\alpha} = 1.54$ Å can be explained by the fact that no monochromator is used in our experiment and consequently a large distribution of wavelength of lower intensities are expected in addition to the CuK$_\alpha$ line. This was proven by conducting an X-ray rocking curve measurement of the Si substrate at the Si(400) lattice planes. The resulting XRD pattern can be found in App. 5. It shows residues of the bremsstrahlung at lower angles, a broad main reflex at 69.1°, resulting from the CuK$_\alpha$ line, a reflex at 61.6°, resulting from the CuK$_\beta$ line ($\lambda_{\mathrm{CuK}_\beta} = 1.39\,$Å) and various foreign lines. This confirms the attribution of the sharp peak in the GIXRD pattern in Fig. 3.3 (b) to the reflex from the Si(311) lattice planes of the Si substrate, generated by the not fully monochromatic X-rays.

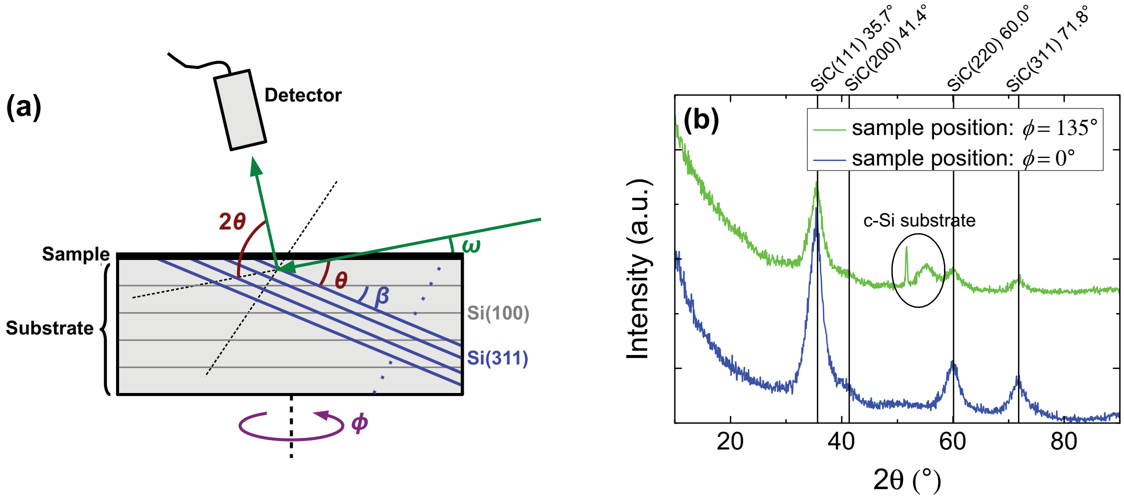

Figure 3.3: The sketch in (a) illustrates the origin of the signal coming from the substrat. The incidence angle ω and the angle β between the Si(100) and the Si(311) planes in the substrate have the effect that the Si(311) lattice planes are hit by the beam under an incidence angle θ which nearly fulfils the Bragg condition and therefore causes a reflex. This results in two additional peaks as marked in (b) with a black circle. If the ϕ orientation of the sample is chosen thoughtfully, no substrate peak occurs, as demonstrated by the blue pattern.

In contrast to the sharp substrate peak, the broad peak stays around 56° for all incident angles and therefore at the Si(311) position for $\lambda_{\mathrm{CuK}_\alpha}$. One proposes to explain this peak by the fact that the incident beam is not completely parallel but shows a certain divergence. Therefore, at the set ω of 0.65° there is a small amount of the CuK$_\alpha$ line with the effective incidence angle of 2.85°, leading to $\theta = \beta + \omega = 28.05°$ and $2\theta = 56.1°$ – giving rise to the observed broad substrate peak.

The substrate signal can be avoided by an appropriate ϕ orientation of the GIXRD samples by ensuring that the plane of incidence and the Si(311) planes are not perpendicular to each other. This orientation is examined experimentally and sketched in Fig. 3.1 (b) for a 1/4 4" sample typically used for GIXRD measurement in this work. This sample orientation is referred to as $\phi = 0°$ position during this work and is equivalent to the $\phi = 90°$, $\phi = 180°$ and $\phi = 270°$ position. The difference of a measurement with and without the substrate peak is demonstrated in Fig. 3.3 (b) by the green, and the blue pattern, respectively.

For GIXRD patterns recorded under the described conditions, a fast and reproducible evaluation algorithm for the Si and SiC NC sizes was developed:

Background correction: Since the signal obtained in GIXRD measurements is very close to the direct beam for small detection angles and since the X-rays are not monochromatic, the GIXRD patterns show a strong background signal, which decreases with increasing detection angle. Therefore, a background correction (BGC) was performed by fitting the background signal and subtracting it. An exponential decay proved to be a suitable fitting function. In Fig. 3.4 (a), the GIXRD measurement of an annealed $Si_{0.63}C_{0.37}$ sample before (green) and after (blue) BGC is shown. The red points indicate, which data is utilized for the fitting of the exponential decay function (black).

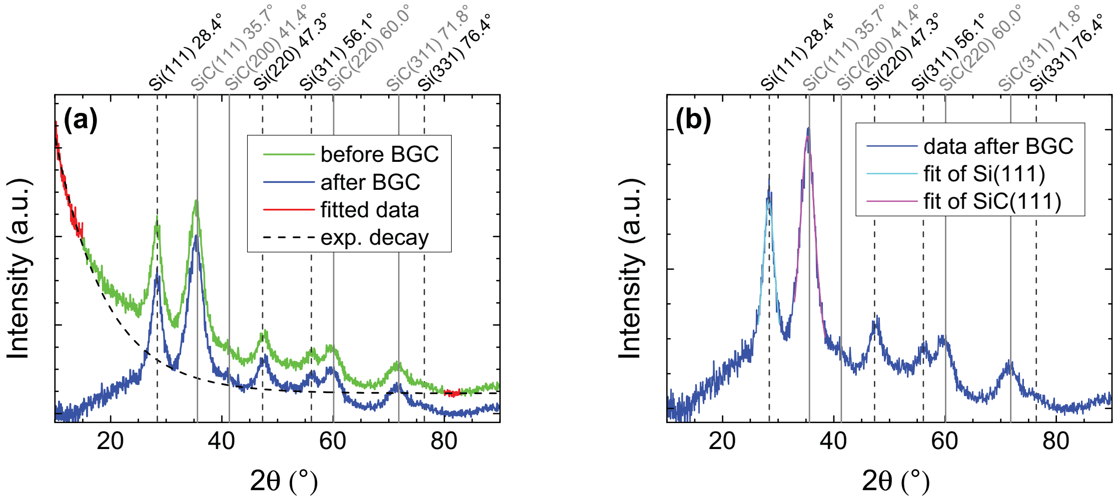

Figure 3.4: The evaluation of GIXRD patterns is demonstrated with the help of a $Si_{0.63}C_{0.37}$ sample annealed at 1100°. In (a) the BGC process is demonstrated: A exponential decay function (black) is fitted to the data (green) and subtracted, resulting in the blue pattern. Then the peak fitting of the two most intense reflexes (Si(111) and SiC(111)) is performed as demonstrated in (b).

Peak fitting: For the peak fitting and the determination of the Si and SiC NC sizes, each peak from the patterns can be used in principle. First it was assured that the evaluation of all peaks lead to the same Si and SiC NC sizes within the experimental error and then only the strongest Si and SiC peaks were used for evaluation – which are the Si(111) and the SiC(111) reflexes. They were fitted by two Lorentz functions (cyan and magenta peaks in Fig. 3.4 for Si(111) and SiC(111), respectively). The appearance of the pattern in Fig. 3.4 (b) suggests that there might be still some broad background signal underneath the sharp reflexes, especially around 30°. Probably this comes from the part of the samples, which are amorphous even after annealing. This superposition of broad amorphous and sharp crystalline peaks makes it impossible to fit the entire pattern. Therefore, only the upper parts of the peaks were fitted to minimise the influence of the background. For this purpose, it must be decided if the constant offset of the fitting function is set to 0 or also fitted. To take into account the amorphous signal, it would be more accurate to chose a variable baseline. But it was observed that this free variable brings a high inaccuracy into the fitting process. Therefore, the baseline was set to zero, accepting a systematic but uniform error.

The FWHM of the peak fits was used to estimate the mean grain size d of the Si and SiC NC by means of Eq. 3.5. The described algorithm for the evaluation of the GIXRD patterns gives rise to an error of $\pm$ 0.5 nm in the absolute value of the grain size. In the case that a batch of samples are measured all together and the fitting procedure is performed for all of them in exactly the same way, the relative changes in grain size between the samples can be determined with a smaller error, specified at the respective measurements.

The described measurement procedure is also possible for layers on quartz substrates. However, the weight of the quartz substrates makes a flat upright mounting challenging. Furthermore, the patterns of layers on quartz substrate are superposed by a broad SiO_2 peak around $2\theta = 20°$. Therefore, such measurements were used only to prove that there is no difference in crystallization of layers on quartz and on Si substrates.

Let us finally say a word about the intensities of the GIXRD reflexes. In principle, it is not possible to draw conclusions from them as they change not only with the thickness of the samples and the size of the scattering nano particles, but also with the slightest change of incidence angle. Such a small change can unintentionally occur due to bending of the sample as well as a dust particle between the sample and the sample holder or a rough sample surface. Furthermore, the intensity of the X-ray tube is not constant but decreases slowly over the time. However, within one pattern the ratio of intensities of the Si(111) and the SiC(111) reflexes can be used to observe qualitatively the increase or decrease of the c-Si phase with respect to the 3C-SiC phase.

3.2 Fourier transform infrared spectroscopy (FTIR)

3.2.1 Basics of FTIR measurements

Infrared spectroscopy is based on the interaction between light and matter in the infrared (IR) wavelength range. The inter-atomic bonds in molecules or lattices in the investigated material are excited to a higher energy level by the IR radiation. These energy levels correspond to quantized vibrational modes of the molecules. Every vibrational transition is characterized by the absorption of a specific wavelength, which changes with both the kind of atoms in the molecule and the strength of the bonds between them. As a descriptive idea of a vibration of the frequency ν, the representation of the molecule bond as a harmonic

oscillator with a certain spring constant κ can serve: When a specific bond gets stronger due to either phase transition (e.g. crystallization) or to a change in the atoms located in the vicinity of the investigated bond – the so-called back bonding – this corresponds to an increasing κ. Because $\nu \propto \sqrt{\kappa}$ [112], a higher κ leads to a higher oscillation frequency, corresponding to a higher wavenumber. Therefore the IR absorption spectrum of a sample provides not only information about the type of molecules in the sample and their bond density but also about the nature of the bonds (crystalline or amorphous, strained or relaxed) and their back bonding, which corresponds to the surrounding network. To be classified as IR active, a molecule must show a variable dipole momentum under radiation. This applies to most heteronuclear molecules and is the case for Si-C, Si-H and C-H bonds.
The FTIR technique is widely used to perform IR measurements. It circumvents the problem of dispersion the probing light into its spectral components [113]. For this, the sample is placed in a Michelson interferometer with one fixed arm and one arm closed with a mobile mirror. By shifting this mirror, an interferogram (IF) occurs in the spacial domain, which is transformed to the frequency domain by a Fourier transformation. The resulting spectrum is divided by the background spectrum taken without the sample. Its negative logarithm is the absorbance spectrum of the investigated sample. The resolution of FTIR measurements is proportional to the scan width, which is the maximum displacement of the mobile mirror. The signal to noise ratio can be improved by increasing the number of scans per sample. For further details on IR and FTIR spectroscopy the reader is referred to standard literature as for example *Solid-State Spectroscopy* by H. Kuzmany [113].

3.2.2 Realization of FTIR measurements

Fourier transform infrared spectroscopy was conducted in the range of $400\,\mathrm{cm}^{-1}$ to $4000\,\mathrm{cm}^{-1}$ with $6\,\mathrm{cm}^{-1}$ resolution using a *Bruker IFS 113v* instrument on layers processed on Si substrates. The measurements were performed under vacuum conditions to avoid the influence of CO_2 and H_2O absorption bands. All absorbance spectra show the superposition of a sinusoidal disturb signal, which results from the constructive interference of the probe light within the plan-parallel substrate. As this interference manifests itself as additional peak in the measured IF in the spacial domain (the so-called echo peak), the sinusoidal disturb signal in the frequency domain can be eliminated by the linearisation of the corresponding part of the IF. This procedure poses a fundamental limit for the resolution of the measurements because a high scan width is always connected to a high number of echo peaks. Their elimination from the IF compensates the gain in resolution through the extension of the scan width.
To remove the absorbance signal caused by the Si substrate, a reference substrate was

measured under identical conditions, and its signal was subtracted from the absorbance of all samples. The absorption coefficient $\alpha(\nu)$ can be calculated from the Lambert-Beer law

$$I_{\mathrm{t}} = I_0 e^{-\alpha(\nu)s} \tag{3.6}$$

were I_{t} and I_0 are the transmitted and the incident intensity, respectively and s is the sample thickness. As the measured absorbance is defined as

$$B(\nu) = -log(\frac{I_{\mathrm{t}}}{I_0}), \tag{3.7}$$

$\alpha(\nu)$ can be calculated by the following relation:

$$\alpha(\nu) = ln10\frac{B(\nu)}{s}. \tag{3.8}$$

To gain further information from FTIR measurements beyond the identification of the vibration modes, accurate peak fitting and a careful interpretation of the results are needed. The FTIR peak fitting was performed by the following routine: First, the background (BG) was fitted and subtracted from the raw data as demonstrated in Fig. 3.5 (a).

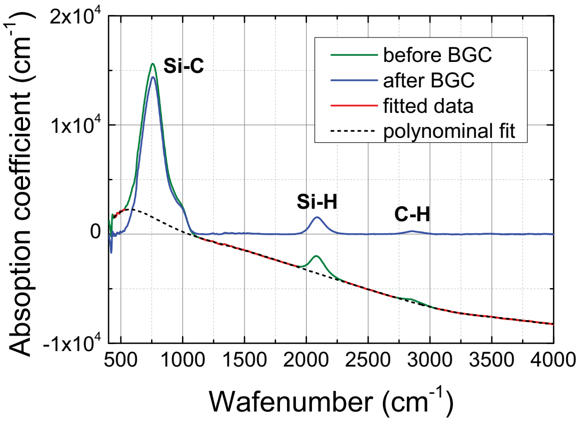

Figure 3.5: Background correction (BGC) procedure of a typical FTIR measurement. The raw data (green) is freed from the main vibration modes (red) and fitted by a polynominal of higher order (black). The subtraction of the polynominal leads to the BG corrected sprectra (blue).

This BG signal is caused by the characteristics of the light source and by the optical elements in the light path, including the sample itself [113]. Because there is, to the author's knowledge, no analytical approach to FTIR BGC, a manual fitting was deemed more reliable than an automated BGC routine. Therefore, the main absorption bands of Si-C, Si-H and C-H were excluded from the raw data (green line in Fig. 3.5 (a)) and the remaining data (red) was fitted by a higher order polynomial (black). Subtraction of this polynomial leads to the corrected data depicted in blue. As a second step, peak assignment and fitting of some of the vibrational modes was performed.

3.2.3 Peak assignment and peak fitting

An unambiguous peak assignment for FTIR spectra of solids is demanding as the precise absorption wavelength changes not only with the atoms involved in the investigated bond vibration but also with the back bonding, the stress in the network, and its degree of crystallization.

Prior to the attempt of a peak assignment, the possible atomic components of the samples must be considered. There are obviously Si, C and H atoms in the as-dep samples, which can build Si-C, Si-H and C-H bonds. The homonuclear Si-Si and C-C bonds in the samples show none or only weak infrared activity and must therefore not be considered for peak assignment. We know from secondary ion mass spectroscopy (SIMS) measurements that there is also a considerable amount of O and N in the as-dep samples. Therefore we have to take into account the Si-N and Si-O main modes for the peak assignment.

Amorphous samples – peak assignment

Good summaries of reported wavenumber positions of absorption bands were published by King *et al.* for a-SiC$_x$:H [68] and Peter *et al.* for a-SiCN:H [114]. For our as-dep samples, three absorption regions can be identified as shown in Fig. 3.6:

1. Absorption around 800 cm^{-1}: **Si-C** vibration dominated [115–118]
2. Absorption around 2000 cm^{-1}: **Si-H$_n$** vibrations [115, 116, 119, 120]
3. Absorption around 2900 cm^{-1}: **C-H$_n$** vibrations [115, 116, 119]

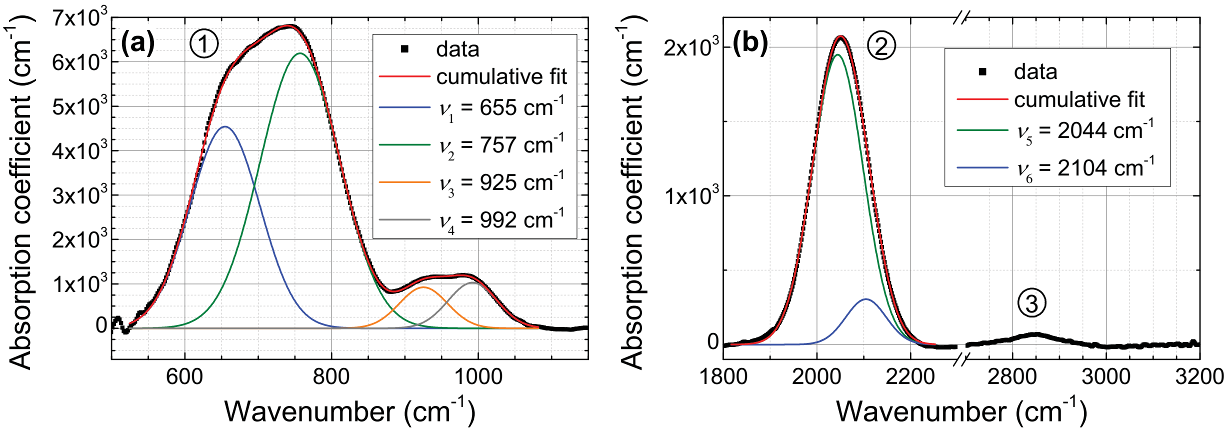

Figure 3.6: Typical FTIR spectrum of an a-Si$_x$C$_{1-x}$:H sample. (a) SiC vibration dominated region ①. The fitting shows that the main Si-C mode (green) strongly overlaps with at least three other vibrations. (b) Si-H$_n$ vibration region ② and C-H$_n$ vibration region ③.

We will demonstrate now that the peak assignment is particularly challenging for amorphous samples due to the large amount of H-related absorptions.

Region 1 can be fitted with at least four Gaussian absorption modes as demonstrated in Fig. 3.6 (a). The main mode $\nu_2 = 757\,\mathrm{cm}^{-1}$ can be assigned to the Si-C stretching vibration [115–118] but could overlap with an Si-H_2 bending mode at $840\,\mathrm{cm}^{-1}$ and higher wavenumbers [116, 119, 120] or with the main Si-N vibration between 830 and $890\,\mathrm{cm}^{-1}$ [121, 122]. For $\nu_1 = 655\,\mathrm{cm}^{-1}$, there are different possible vibrations: Another Si-C stretching mode around $670\,\mathrm{cm}^{-1}$ [86, 116] as well as Si-H and Si-H_2 rocking modes [116, 120]. The absorption at $\nu_3 = 925\,\mathrm{cm}^{-1}$ could result either from Si-H_2 or from C-SiH_2 bending vibrations [116, 119]. The $\nu_4 = 992\,\mathrm{cm}^{-1}$ mode can be assigned to C-H_n rocking vibrations [115, 116, 119] or to one of the numerous Si-O vibrations starting at $1000\,\mathrm{cm}^{-1}$ [123].

Region 2 (Fig. 3.6 (b)) consists of a number of strongly overlapping Si-H_n modes. In all investigated samples, two Gaussian peaks were necessary to obtain a good fit. The two peaks were not assigned to a specific Si-H_n mode due to their strong overlapping.

Further fitting and specific peak assignment to the different C-H_n modes were not performed in **Region 3** due to the weak intensity of these vibrations, as Fig. 3.6 (b) demonstrates.

Amorphous samples – Hydrogen effusion

As described above, the peak assignment is highly uncertain for the amorphous Si-C region. Therefore, only the Si-H region was evaluated in amorphous samples. The peak around $2000\,\mathrm{cm}^{-1}$ was fitted with two Gaussian peaks, as depicted in Fig. 3.6(b), and the area of this peak is used to investigate the progress of H effusion in the samples.

Crystalline samples – Peak assignment

The annealing of the samples leads to H-effusion, the formation of more Si-C bonds, and their crystallization. In the FTIR spectra, this leads to vanishing of all Si-H related bonds (region 1, 2 and 3), increase of the Si-C mode in region 1, and its peak shift to higher wavenumbers. This can be observed in Fig. 3.7 (a) where an as-dep (black) and an annealed FTIR spectrum (red) are compared. Please note that the as-dep spectrum in Fig. 3.7 (a) and in Fig. 3.6 (a) are the same. All peaks around $1000\,\mathrm{cm}^{-1}$ disappear during annealing, which shows that these were H-related vibrations and that the O content in the samples is too small to cause an FTIR signal. The main mode after annealing can clearly be assigned to Si-C. But depending on the Si content of the investigated sample, there were either two or three peaks necessary to obtain a good peak fit. Two peaks occur at wavenumbers under $800\,\mathrm{cm}^{1}$. Both of them were attributed to Si-C vibrations following the argumentation from Musumeci *et al.* [124, 125]: The mode at lower wavenumbers represents the amorphous part of the network while the peak at higher wavenumbers is assigned to the crystalline Si-C vibration. The third peak arises above 800 cm^{-1} for high Si contents or/and after high temperature annealing. Its assignment will be discussed in detail in the course of the next section.

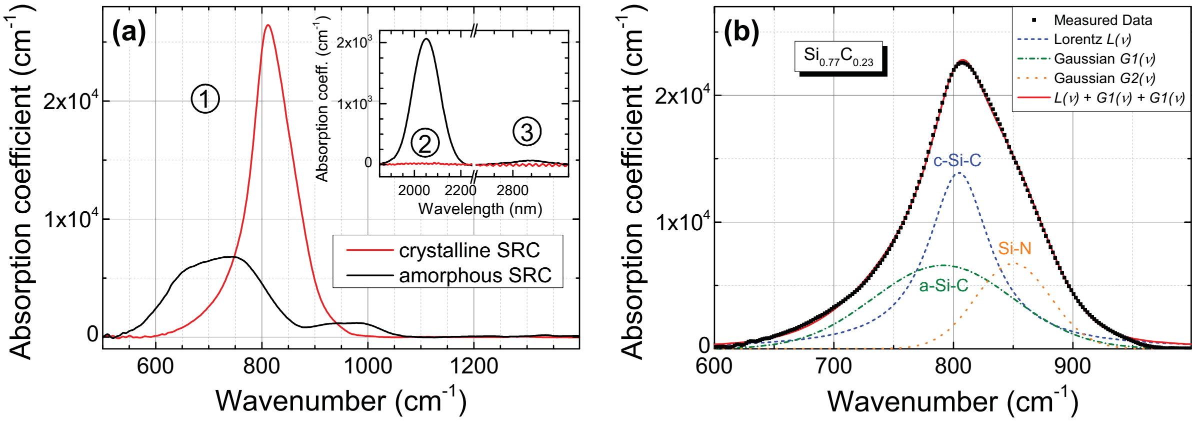

Figure 3.7: (a) Typical change of an FTIR spectrum from amorphous (black) to crystalline (red) samples. The Si-C mode ① increases and shifts to higher wavenumbers while all H-related modes in regions ① , ② and ③ vanish. (b): Si-C vibration mode of an exemplary FTIR spectrum fitted with one Lorentzian $L(\nu)$ and two Gaussian peaks $G1(\nu)$ and $G2(\nu)$. $L(\nu)$ represents the crystalline and $G1(\nu)$ the amorphous part of the Si-C network while $G2(\nu)$ is attributed to the asymmetric Si-N stretching vibration.

Crystalline samples – SiC crystallinity

During this work, two different methods to determine the SiC crystallinity from FTIR spectra were taken from the literature and checked for their applicability and reproducibility.
1. The **peak-shift method** [33] exploits the above mentioned fact that the strengthening of the Si-C bonds is accompanied by a peak shift to higher wavenumbers. This means that for samples with the same composition, the Si-C peak position can directly be used as a value for the SiC crystallinity. The position of the Si-C mode is determined as follows: For mainly amorphous spectra, the center of the Gaussian shaped Si-C mode defines the Si-C position. As soon as the Lorentz peak occurs due to the crystallization of Si-C bonds at higher temperatures, its center is referred to as Si-C position. This method has the advantage of being independent of a fitting process. However, it also has the disadvantage of being applicable only for samples with the same composition. Therefore, a second method was also applied in this work.
2. The **fitting method** [79,124,126] comprises a fitting of the Si-C mode at approximately 800 cm^{-1} by a combination of a Lorentzian $L(\nu)$ and a Gaussian $G(\nu)$ peak. It is known that the Si-C network after annealing consists of both crystalline and amorphous domains. The Lorentz part of the peak area can be attributed to the crystalline Si-C phase in the

samples while the Gaussian part arises from a random and hence amorphous Si-C bond distribution [79, 117, 124, 127]. Thus, the fit function can be written as

$$\alpha(\nu) = L(\nu) + G(\nu) \tag{3.9}$$

$$L(\nu) = A_{\mathrm{L}} \cdot \frac{2}{\pi} \cdot \frac{\sigma_{\mathrm{L}}}{4(\nu - \nu_{\mathrm{L}})^2 + \sigma_{\mathrm{L}}^2} \tag{3.10}$$

$$G(\nu) = A_{\mathrm{G}} \cdot \frac{1}{\sigma_{\mathrm{G}}} \sqrt{\frac{4\ln(2)}{\pi}} \cdot \exp\left[-4\ln(2) \cdot \left(\frac{\nu - \nu_{\mathrm{G}}}{\sigma_{\mathrm{G}}}\right)^2\right], \tag{3.11}$$

where A_{L} (A_{G}) is the area of the peak, ν_{L} (ν_{G}) is the peak position, and σ_{L} (σ_{G}) is the FWHM of the Lorentz (Gaussian) peak. The peak area A is proportional to the bond density of the corresponding absorption mode [68, 125]:

$$N(\text{Si-C}) = Q_{\text{Si-C}} A = Q_{\text{Si-C}} \int_{\nu_1}^{\nu_2} \alpha(\nu) d\nu \approx \frac{K_{\text{Si-C}}}{\nu_{\mathrm{G/L}}} \int_{\nu_1}^{\nu_2} \alpha(\nu) d\nu \tag{3.12}$$

with the proportionality constants $Q_{\text{Si-C}}$ or $K_{\text{Si-C}}$. In literature, the ratio $\frac{A_{\mathrm{L}}}{A_{\mathrm{L}}+A_{\mathrm{G}}}$ is often used to estimate the crystalline fraction of the Si-C phase [29, 79, 127]. Strictly speaking, this approach is only valid if the bond density in the amorphous phase is connected to the Gaussian peak area by the same $Q_{\text{Si-C}}$ by which the bond density in the crystalline phase is connected to the Lorentzian peak area. $K_{\text{Si-C}}$ for 3C-SiC is reported to be approximately $2.1 \cdot 10^{19}\,\mathrm{cm}^{-2}$ [117, 125] while for a-SiC, $K_{\text{Si-C}}$ ranges from $2.1 \cdot 10^{19}\,\mathrm{cm}^{-2}$ to $3.6 \cdot 10^{19}\,\mathrm{cm}^{-2}$ [68, 125]. Using $\nu_L = 790\,\mathrm{cm}^{-1}$ and $\nu_G = 740\,\mathrm{cm}^{-1}$ for the c- and the a-SiC modes, respectively, we estimate $Q_{\text{Si-C}} = 2.7 \cdot 10^{16}\,\mathrm{cm}^{-1}$ for c-SiC and $2.8 \cdot 10^{16}\,\mathrm{cm}^{-1} < Q_{\text{Si-C}} < 4.9 \cdot 10^{16}\,\mathrm{cm}^{-1}$ for a-SiC. The trends in crystallinity investigated in this work are maintained for all these values of $Q_{\text{Si-C}}$. This result means that the formula above cannot be used to calculate the absolute crystallinity but is useful for investigating the crystallinity trends of the Si-C network.

To ensure a fast and reproducible evaluation of the FTIR spectra by the fitting method, a corresponding *Mathematica*® program was developed within the scope of the master thesis of A. Reichert, which was supervised in the framework of this Ph.D. thesis [99].

As mentioned above, for samples with a high Si content after annealing at higher temperatures, one Lorentzian $L(\nu)$ and two Gaussian peaks ($G1(\nu)$ and $G2(\nu)$) were necessary to obtain a good peak fitting, as shown in Fig. 3.7 (b) for an $\mathrm{Si}_{0.77}\mathrm{C}_{0.23}$ sample annealed at 1100°C. First, $G2(\nu)$ at $850\,\mathrm{cm}^{-1}$ was assigned to a second amorphous Si-C mode. Further measurements showed an increasing $G2(\nu)$ mode with increasing temperature, disproving the a-SiC assignment. Secondary ion mass spectroscopy measurements reveal that there are up to $3{\cdot}10^{21}$ at/cm^3 nitrogen atoms in our annealed Si-rich layers [128]. Therefore, $G2(\nu)$ was assigned to the **asymmetric N-Si$_3$ stretching mode** ($830\dots890\,\mathrm{cm}^{-1}$ [114,121,122]). This assumption was verified by estimating the Si-N bond density [38, 57] analogously to Eq. 3.12 from the area of the fitted $G2(\nu)$ mode, the proportionality constant $K_{\text{Si-N}}$ and the central wavelength of the $G2(\nu)$ mode $\nu_{\text{Si-N}}$. With $K_{\text{Si-N}} = 2{\cdot}10^{19}\,\mathrm{cm}^{-2}$ [33] and $\nu_{\text{Si-N}} = 850\,\mathrm{cm}^{-1}$ we obtain $N(\text{Si-N}) = 1.2{\cdot}10^{23}$ bonds/cm^3 for the example in Fig. 3.5 (b), which corresponds to a nitrogen concentration of $4{\cdot}10^{21}$ at/cm^3 assuming threefold coordination. This matches surprisingly well with the SIMS value and supports the assignment of $G2(\nu)$, which is thus not taken into account for the evaluation of SiC crystallinity. Nevertheless, the Si-N peak leads to increasing uncertainty of the SiC crystallinity for increasing Si content and increasing temperature because $G1(\nu)$ and $G2(\nu)$ correlate strongly with each other. Whereas the relative error in SiC crystallinity for samples with the same Si content is in the range of few percent (depending on the quality of the fit), the error in SiC crystallinity comparing samples with different Si content is roughly 20%. In the case of the peak shift method, the determination of the peak position is very precise, but cannot be converted to an absolute SiC crystallinity because the relation between peak position and SiC crystallinity is not necessarily linear. Therefore, conclusions about the SiC crystallinity were drawn only in cases where both evaluation methods (peak-shift method and fitting method) lead to the same trends.

Origin of nitrogen

In order to clarify the origin of the large amount of N in the Si$_x$C$_{1\text{-}x}$ layers, first the most obvious possibility was checked: The annealing under N$_2$ flow. Therefore, one sample annealed under N$_2$ and one sample annealed under Ar gas were investigated by SIMS. The resulting N profiles are depicted in Fig. 3.8 (a).

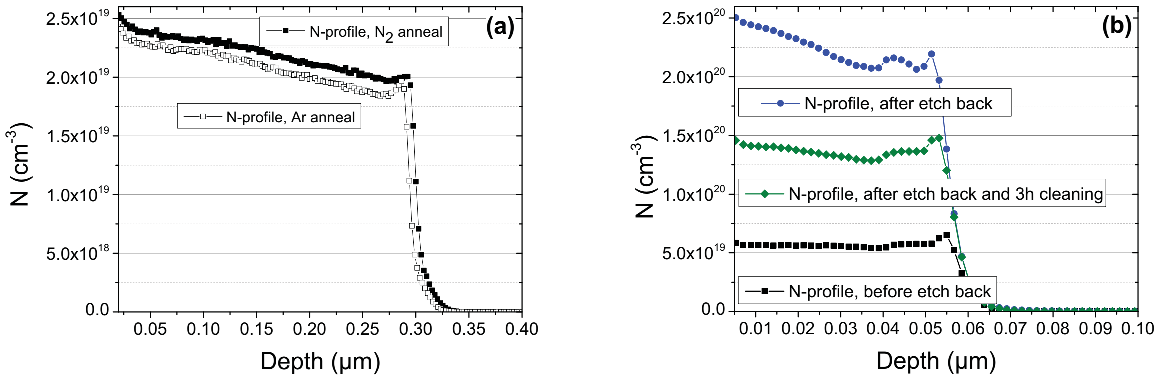

Figure 3.8: N profiles from SIMS measurements: (a) SiC samples annealed under Ar (open squares) and under N$_2$ (filled squares). (b) SiC samples deposited in the plasma chamber before (black) and after (blue) the etch back step. After the subsequent encapsulation of the sample tray another SiC samples is deposited and shows the green N-profile.

The sample annealed under Ar (open squares) shows just a small decrease in N content compared to the samples annealed under N_2 (filled squares). Consequently, the majority of N atoms must be incorporated into the layers during the deposition process and not during the annealing step. The most probable source of N in the plasma chamber is the etch back process performed with a mixture of Ar, NF_3 and N_2O. This was verified by the SIMS profiles in Fig. 3.8 (b). A sample, deposited before the etch back step (black) shows an N content of about $6{\cdot}10^{19}\,\mathrm{cm}^{-3}$ (black squares). This increases up to $2.5{\cdot}10^{20}\,\mathrm{cm}^{-3}$ for a sample directly deposited after the etch back step (blue circles) and reduces by half when the sample tray is encapsulated with about 300 nm SiC after the etch back step (green diamonds). This result is confirmed by another measurement. The plasma chamber was investigated using H_2/Ar plasma by optical emission spectroscopy (OES) and observed a clear emission line at 387.1 nm after the etch back step, which results from CN molecules. This emission line decreases with increasing thickness of the SiC encapsulation layer. This behaviour of the CN emission line correlates qualitatively with the amount of N determined by SIMS.

One can conclude that the majority of N atoms is incorporated into the layers during the plasma deposition and that the incorporation of N atoms during the annealing step is marginal up to a temperature of 1100°C. The condition of the plasma chamber determines the amount of incorporated N. A different chamber condition probably explains the different amounts of N in the black curves in Fig. 3.8 (a) and (b), which result from a nominal equivalent SiC sample. An even greater influence on the N content than the condition of the plasma chamber is the Si content of the $Si_xC_{1\text{-}x}$ layers. With increasing Si content, the N content increases also. This is not surprising as an increasing availability of Si obviously favours the formation of Si_3N_4. As N atoms lead to n-doping in SiC [61], we must consider our $Si_xC_{1\text{-}x}$ layers to be increasingly n-doped with increasing Si content.

3.3 Raman spectroscopy

3.3.1 Basics of Raman measurements

This short introduction into Raman spectroscopy is based on the book by H. Kuzmany [113] where a comprehensive description of the method can be found. Raman spectroscopy exploits the inelastic scattering of photons at molecules or crystals. The photons excite vibrational modes of molecules or phonon modes in crystals. If this excitation of phonon modes causes a change in the polarizability of molecules or the susceptibity of crystals, they are classified as **Raman active**. In this case, photons are emitted, which show either the

same wavelength (Rayleigh scattering), a higher wavelength (Stokes scattering), or a lower wavelength (anti-Stokes scattering) than the incident light. The Stokes and the anti-Stokes scattering lines contain information about the nature of the scattering molecules or the network of the crystal. As the Stokes line is the more intense one at elevated and low temperatures in respect to the Debye temperature, it is usually used in experiments as well as in this work. The energy of the Stokes line is usually presented in wavenumbers relatively to the Rayleigh line and referred to as "Raman shift". As homonuclear diatomic molecules are Raman active, Raman spectroscopy is used as a complementary method to FTIR spectroscopy in this work to investigate Si-Si and C-C.
As light source for Raman measurements, a frequency-doubled Nd:YAG laser with a wavelength of 532 nm was used. For investigations of the samples' crystallinity, it is necessary to ensure that the laser power is low enough to avoid laser induced crystallization of the samples. Therefore, the laser power was limited to 500 μW. To avoid an overexposure of the detector, an optical filter for the elastically scattered light of 532 nm was installed – leading to a cut-off of the Raman spectra below 150 cm^{-1}.

3.3.2 Peak attribution in Raman spectra

Every Raman active molecule and crystal lattice can be characterized on the basis of its characteristic Raman spectrum. In the case of Si, the amorphous, the semicrystalline and the crystalline phase show their own distinctive Raman modes [129]. This is demonstrated in Fig. 3.9 with the a-Si spectrum in black, the semicrystalline one in green and the monocrystalline one in red. These different Raman modes can be used to investigate the Si crystallinity in $\mathrm{Si}_x\mathrm{C}_{1\text{-}x}$ samples.

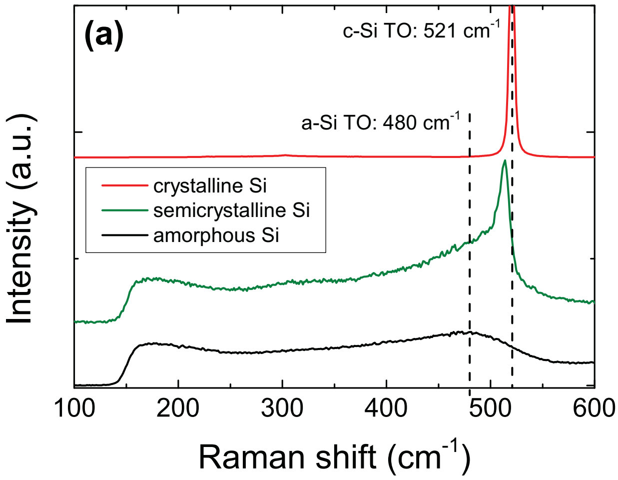

Figure 3.9: Example of Raman spectrum of an amorphous (black), semicrystalline (green) and monocrystalline (red) silicon sample. The amorphous spectrum results from a typical as-dep sample, the semicrystalline one from $\mathrm{Si}_{0.63}\mathrm{C}_{0.37}$ and the crystalline one from the Si substrate.

Because of the conservation of momentum in the crystalline lattice, monocrystalline Si shows only one Raman mode at 521 $\mathrm{cm^{-1}}$ (Fig. 3.9, red). It represents the transversal optical phonon (TO) mode and is Lorentzian shaped due to the crystalline character of the underlying lattice vibration [130]. In the amorphous state, Si shows four Gaussian shaped Raman modes due to the lack of long-range order [131] (Fig. 3.9, black). All of them are located between 100 and 500 $\mathrm{cm^{-1}}$ starting with the transveral acoustical (TA) mode at 150 $\mathrm{cm^{-1}}$ followed by the longitudinal acoustical (LA) mode at 310 $\mathrm{cm^{-1}}$. The mode at 380 $\mathrm{cm^{-1}}$ is attributed to the longitudinal optical (LO) mode and at 480 $\mathrm{cm^{-1}}$ the most intensive a-Si mode is located, which belongs to the transversal optical (TO) vibration [131, 132]. The semicrystalline spectrum (Fig. 3.9, green) is a superposition of the amorphous and the crystalline spectrum, resulting in a sharp peak between 512 and 520 $\mathrm{cm^{-1}}$ with a shoulder at a shorter wavenumber. This peak results from small Si crystals and shifts to higher wavenumber with increasing crystal size as well as strain in the samples [133]. The shoulder on the lower wavenumber side of the c-Si peak consists of the strongly overlapping a-Si TO mode at 480 $\mathrm{cm^{-1}}$ and an additional peak around 500 $\mathrm{cm^{-1}}$, attributed to defect rich micro- and nanocrystalline Si [134, 135].

3.3.3 Realization of Raman measurements

In this work, Raman measurements were established to determine the Si crystallinity χ_{Si} of the $\mathrm{Si}_x\mathrm{C}_{1\text{-}x}$ samples. Usually, χ_{Si} is given by the ratio between the c-Si TO mode and the total area of the TO mode [136–138], resulting from the fitting of the semicrystalline spectrum. Due to the large amount of overlapping a- and c-Si modes involved – leading to a high degree of freedom – an unambiguous fitting is impossible for the $\mathrm{Si}_x\mathrm{C}_{1\text{-}x}$ samples. Therefore, this method is not considered as suitable. Instead, the so-called **subtraction method** [139], which waives the fitting of the semicrystalline spectrum was applied. It was found that this method is suitable to quantify χ_{Si} of the $\mathrm{Si}_x\mathrm{C}_{1\text{-}x}$ samples reproducibly. The subtraction method takes advantage of the fact that the transformation from an amorphous to a c-Si sample involves only the appearance of one additional mode, which is the c-Si TO mode at 520 $\mathrm{cm^{-1}}$. The amorphous spectrum decreases uniformly with progressing crystallization and vanishes completely in the case of fully crystallized Si. To determine χ_{Si} from a semicrystalline sample, the spectrum from the same sample in the fully amorphous state must also be measured. Then, in a first step, this amorphous spectrum of the sample is fitted with the help of the four Gaussian vibrations mentioned above, as representatively shown in Fig. 3.10 (a). In a second step, the amorphous spectrum is rescaled down to the semicrystalline spectrum, as demonstrated in Fig. 3.10 (b): The amorphous spectrum I_{amo} (black) is scaled down (blue) to represent the amorphous part of the semicrystalline spectrum I_{semi} (green). This is the most delicate part of the procedure. For this purpose, a scaling factor S must be determined in a reproducible way.

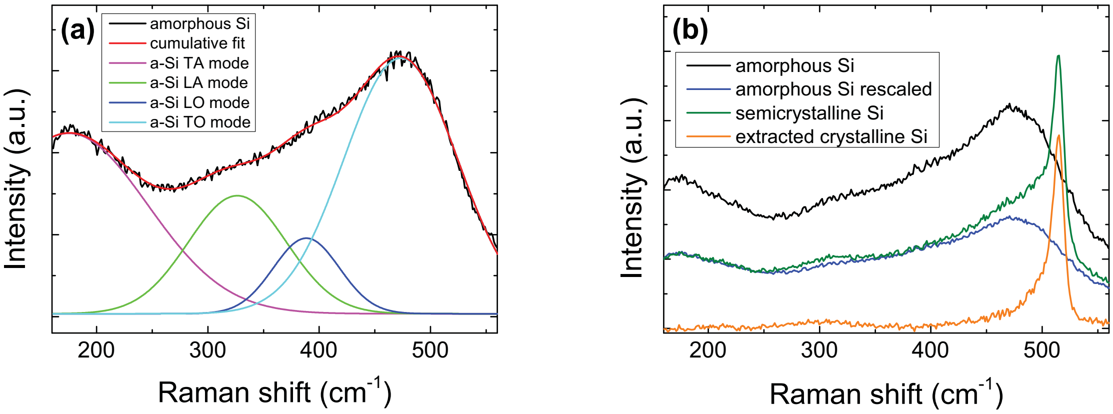

Figure 3.10: Demonstration of the subtraction method to determine the Si crystallinity χ_{Si}. (a) The fully amorphous spectrum of a sample is fitted with four Gaussian shaped a-Si modes. Only the TO mode at 480 cm^{-1} (cyan) is used in the further evaluation. The other three a-Si modes are taken into account to obtain a good fit. (b) The amorphous spectrum (black) and the corresponding semicrystalline spectrum (green) of one sample before and after annealing are depicted. The blue curve represents the downscaled amorphous spectrum, which is subtracted from the semicrystalline one to extract the only crystalline part of the semicrystalline spectrum (orange). The fraction of this extracted peak on the area of the downscaled a-Si TO mode provides a value for χ_{Si}.

This was done by forming the ratio of intensities between the semicrystalline and the amorphous spectrum for all data points p, summing them up and averaging over the number of utilised data points P

$$S = \frac{1}{P}\sum_{p}\frac{I_{\mathrm{semi},p}}{I_{\mathrm{amo},p}}. \tag{3.13}$$

It was experimentally found that a suitable range of utilised data points is between 380 and 420 cm^{-1}.

Thirdly, the downscaled amorphous spectrum (blue) is subtracted from the semicrystalline spectrum (green). The resulting peak represents the crystalline part of the semicrystalline sample I_{cry} (orange):

$$I_{\mathrm{cry}} = I_{\mathrm{semi}} - S \cdot I_{\mathrm{amo}}. \tag{3.14}$$

As the final step, the ratio between the area of the extracted crystalline peak and the downscaled a-Si TO mode is calculated giving a value for χ_{Si}:

$$\chi_{\mathrm{Si}} = \frac{\int\limits_{\mathrm{TO}} I_{\mathrm{cry}} d\nu}{yS \cdot \int\limits_{\mathrm{TO}} I_{\mathrm{amo}} d\nu + \int\limits_{\mathrm{TO}} I_{\mathrm{cry}} d\nu}. \tag{3.15}$$

The factor y takes into account the different scattering cross sections for amorphous and crystalline phases and is 0.88 in the case of Si [130]. To determine $\int\limits_{\mathrm{TO}} I_{\mathrm{amo}} d\nu$, the area of the fitted and downscaled Gaussian peak at 480 cm^{-1} is used (cyan peak in Fig. 3.10 (a)). $\int\limits_{\mathrm{TO}} I_{\mathrm{cry}} d\nu$ is calculated by interpolation and integration of the extracted crystalline peak from the semicrystalline spectrum between 440 and 560 cm^{-1} because the crystalline distributions are expected in this wavenumber range.

To ensure a fast and reproducible evaluation of the Raman spectra by the subtraction method, a corresponding *Mathematica*® program was developed within the scope of the master thesis of A. Reichert, which was supervised in the framework of this Ph.D. thesis [99].

As a reference value, the subtraction method was also applied to a 100% crystalline FZ Si wafer and determined an $\chi_{\text{c-Si}}$ of around 80%. Hence, one can conclude that χ_{Si} is underestimated by the subtraction method. Anyway it is not clear how much χ_{Si} deviates from the real absolute value for the Si crystallinity in the samples. But it is a reliable method to observe trends in crystallization. Therefore, the estimated experimental error refers to the relative differences in crystallinity and not to the absolute value. It was estimated experimentally by the systematic application of the fitting procedure to be ± 3%. The main uncertainty results from the downscaling process of the amorphous to the semicrystalline spectrum. If an absolute value for the Si crystallinity is needed during this work, we add 20% crystallinity to the determined value due to the underestimation and assume an error of ±10%.

A number of **additional measurement techniques** were used in this work without focusing on their further improvement. They are summarized in App. 6.

Chapter 4

Crystallization of a-Si_xC_{1-x}:H layers

As mentioned in Sec. 1.3.2, a straightforward transformation of a-Si_xC_{1-x}*:H samples into Si NC in an a-SiC matrix upon annealing has not been realized experimentally so far, despite the differences in crystallization activation energies of the individual a-Si and a-SiC systems. Therefore, we targeted the separation of Si and SiC crystallization by other parameters than the temperature in several experiments. The first experiment describes a-*Si_xC_{1-x}*:H crystallization with a reduced thermal budget by comparing the conventional FA process with the faster RTA process. Parts of the annealing and characterization were done in the scope of A. Reichert's master thesis [99]. We observed a strong dependence of crystallization on time and temperature and investigated this further in a second experiment by isothermal FA, which allows a rough estimation of the effective activation energy of crystallization. The third experiment describes a two-step anneal in the ZMR setup to separate the process of nucleation and crystal growth. The ZMR annealing and parts of the characterization were done in the scope of the bachelor thesis of T. Fehrenbach [100]. The temperature of maximum Si conversion just below the melting point of Si was estimated and a successful two-step annealing process to partly separate Si nucleation and crystal growth was established. These results suggest a beneficial influence of a further reduction of annealing time on Si NC growth. Therefore, nonequilibrium FLA annealing was used in the fourth experiment, carried out by Dr. S. Prucnal from Helmholz-Zentrum Dresden-Rossendorf. After a careful adjustment of the* Si_xC_{1-x} *sample parameters and the annealing conditions, FLA has been successfully used to produce Si NC layers with a reduced SiC crystallinity. Parts of the FLA discussion are supported by simulations by J. Hofmann and will be described in detail in his upcoming master thesis, which is supervised in the framework of this Ph.D. thesis and is still ongoing. The FLA results were published in the Journal of Applied Physics [140].*

4.1 Reduction of thermal budget

The replacement of FA by RTA is reported to be beneficial for the ratio between c-Si and c-SiC phase in Si_xC_{1-x} layers by Wan *et al.* [35]. Additionally, the reduction of annealing time is interesting from a technological point of view as it implies a reduction of energy and therefore a cost benefit together with the time benefit.

4.1.1 Nanocrystal growth

The crystallization of Si_xC_{1-x} samples with Si contents of 50%, 63% and 77% was investigated by a temperature series between 270°C (deposition temperature (as-dep)) and 1100°C carried out in both the FA and the RTA setup. All samples were characterized by GIXRD measurements shown in Fig. 4.1 to observe the progressive crystallization.

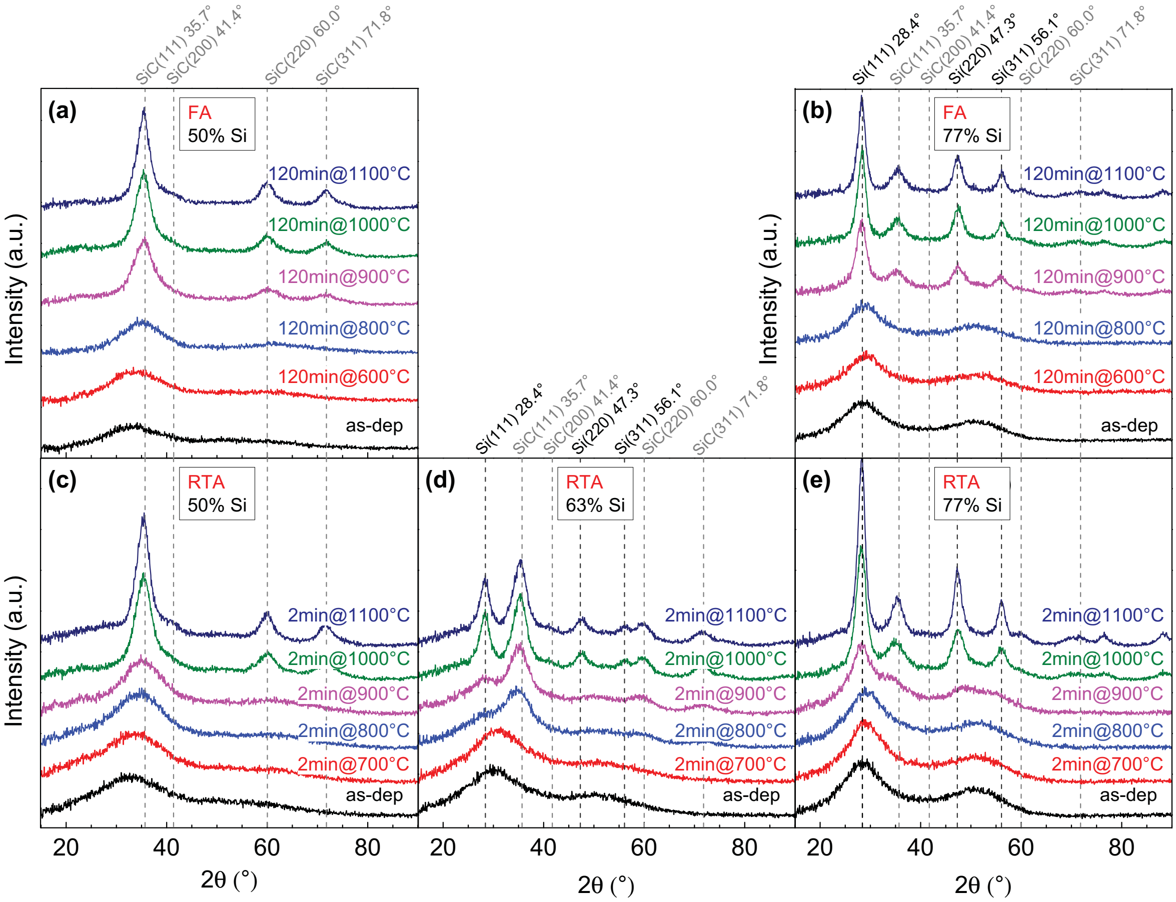

Figure 4.1: GIXRD spectra of anneling temperature series conducetd by FA ((a) and (b)) and by RTA ((c),(d) and (e)). The Si content varies from 50% in (a) and (c) over 63% in (d) up to 77% in (b) and (e).

The stoichiometric $Si_{0.50}C_{0.50}$ samples in Fig. 4.1 (a) (FA) and (c) (RTA) show a broad peak around 30° already in the as-dep state. This indicates the presence of SiC clusters with a short range order similar to the crystalline lattice. This peak narrows and shifts to the SiC(111) position at 35.6°C for increasing temperatures. At 900°C and 1000°C for FA and RTA, respectively, the SiC(220) and SiC(311) reflex appears as well as the SiC(200) peak in the form of a shoulder of the SiC(111) reflex. In contrast, all Si-rich layers (Fig. 4.1 (b), (d) and (e)) show two broad reflexes in the as-dep state, indicating the presence of both Si and SiC clusters. The broad reflex around 30° transforms into the Si(111) and the SiC(111) reflex at 900°C for both $Si_{0.63}C_{0.37}$ and $Si_{0.77}C_{0.23}$ samples, which continue growing and narrowing for increasing temperatures. Between 900°C and 1100°C, all Si and SiC reflexes from the Si and SiC powder patterns appear. For layers with a Si content of 63%, only RTA samples exist (Fig. 4.1 (d)). But for 77% samples, the comparison between FA (Fig. 4.1 (b)) and RTA (Fig. 4.1 (e)) show clearly more crystalline phase for FA than for RTA samples at 900°C and also do the 50% samples. Comparing the Si(111)/SiC(111) ratio for the 1100°C patterns of all three Si contents, it is obvious that it increases with increasing Si content, indicating the greater fraction of Si phase.

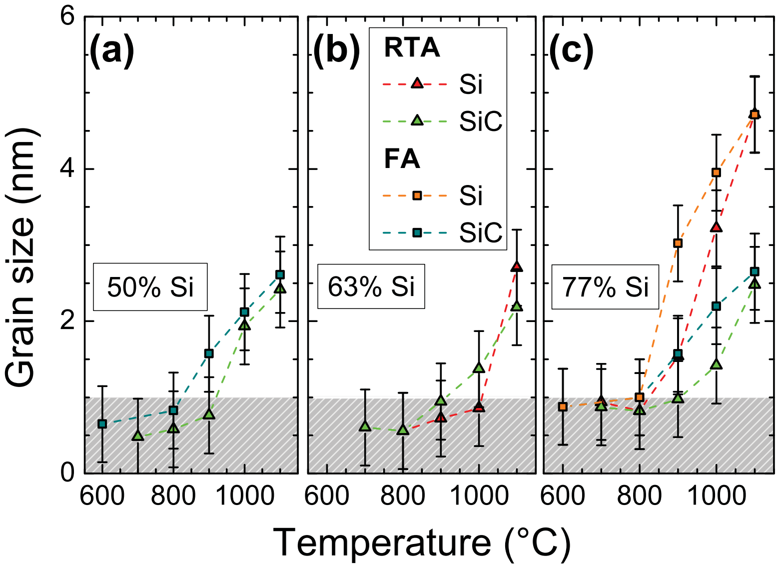

Figure 4.2: Si and SiC grain sizes over the annealing temperture during FA (squares) and RTA (triangles) for $Si_{0.50}C_{0.50}$ (a), $Si_{0.63}C_{0.37}$ (b) and $Si_{0.77}C_{0.23}$ (c) samples. The grey cross-hatched areas indicate NC sizes under 1 nm.

The results of the grain size determination from the Scherrer formula (Eq. 3.5) of the Si(111) and SiC(111) reflex for 50%, 63% and 77% Si content are depicted in Fig. 4.2 (a), (b) and (c), respectively. The grey cross-hatched areas indicate NC sizes under 1 nm. Although they can be determined, it is not straightforward to talk about NC in this case because the critical nucleus radius for a stable Si NC is reported to be around 1 nm [88]. It is also worth noting that, since Si and SiC have a lattice constant of $a_{\mathrm{Si}} = 5.43$ Å and $a_{\mathrm{SiC}} = 4.36$ Å, respectively, and both crystallize in the diamond structure, a cubic NC with a side length of 1 nm would contain only 12 unit cells (less than 100 atoms) in case of SiC and 6 unit cells (less than 50 atoms) in case of Si. It is questionable if this can already be defined as crystal or must still be considered as amorphous clusters.

The SiC NC size is shown as green and cyan data points in Fig. 4.2. For RTA, a SiC grain size over 1 nm is reached at 1000°C for all Si contents. All SiC NC show a grain size of around 2.5 nm for both annealing processes and all Si contents after 1100°C. For FA, corresponding SiC NC form already at 900°C. In the case of Si NC (red and orange data points), the final grain size depends strongly on the Si content. While the NC size is only (2.7 ± 0.5) nm in the $Si_{0.63}C_{0.37}$ samples, it reaches (4.7 ± 0.5) nm in $Si_{0.77}C_{0.23}$. For the $Si_{0.77}C_{0.23}$ samples (Fig. 4.2 (c)), there occurs a discrepancy in Si NC size between FA and RTA samples for 900°C and 1000°C and a disappearance of this discrepancy for 1100°C as analogically observed for SiC NC. Both the annealing time and the ramping-up time are much longer in FA compared to RTA. Therefore, the Si and SiC NC have no time during RTA at 900°C and 1000°C to reach the FA grain size. Since crystallization is a thermally activated process, its velocity increases with increasing temperature. Consequently, the same NC size at 1100°C is reached for both annealing methods, the slow FA and the fast RTA. It will be aimed at examining the characteristic of this thermally activated process in Sec. 4.2 by estimating the activation energy of Si and SiC crystallization.

So far, one can state that an increasing Si content leads to an increasing Si NC size. But does not influence the SiC NC size at all. This fact is not as self-evident as it appears and will be discussed in Sec. 4.5. The replacement of the FA by the faster RTA process shows an influence on the Si and SiC NC size for temperatures below 1100°C. However, as Si and SiC NC size are both influenced in the same way, and as the effect is not present any more after annealing at 1100°C, the simple replacement of FA by RTA does not resolve the problem of c-SiC formation. Therefore, the formation of c-SiC upon annealing must be investigated more closely in order to clarify a possible connection between the H content of the layers and the SiC crystallization.

4.1.2 Hydrogen effusion and SiC crystallinity

The as-dep layers contain a considerable amount of H, bonded as Si-H_n and C-H_n. During annealing, the Si-H_n and C-H_n bonds break and H effusion takes place combined with a shrinkage of the layers by about 30%. The open bonds recombine to either Si-C, Si-Si or C-C bonds. Therefore, a careful analysis of the H effusion via FTIR gives an insight into the crystallization process. Temperature series of samples of varying Si content were conducted between 270°C (as-dep) and 1100°C by FA (50 and 77% Si) and RTA (50, 63 and 77% Si) as depicted in Fig. 4.3. In Fig. 4.3 (a) and (c) the FTIR spectra of the $Si_{0.50}C_{0.50}$ samples treated by FA and RTA are depicted, respectively. Fig. 4.3 (d) shows the $Si_{0.63}C_{0.37}$ RTA samples and Fig. 4.3 (b) and (e) the $Si_{0.77}C_{0.23}$ FA and RTA samples.

The typical annealing time for FA was 30 min for 1100°C and 2 h for all other temperatures. The main plots show the development of the Si-C mode under annealing while the Si-H mode is depicted in the insets.

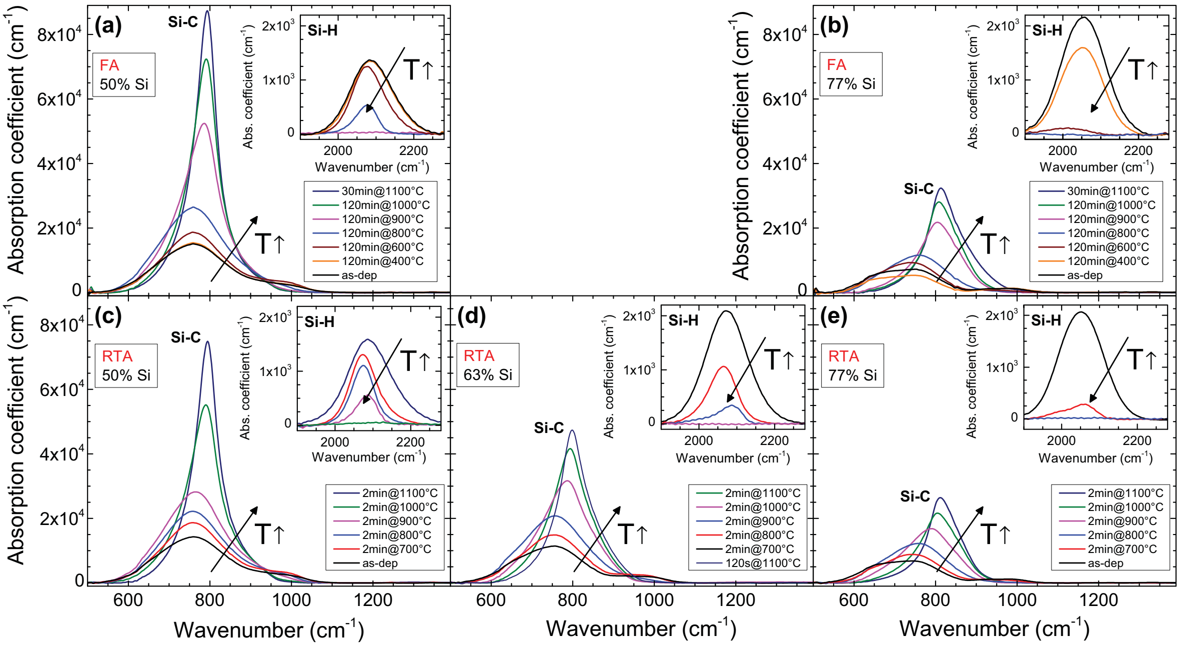

Figure 4.3: FTIR spectra of anneling temperature series conducetd by FA ((a) and (b)) and by RTA ((c),(d) and (e)). The Si content varies from 50% in (a) and (c) over 63% in (d) up to 77% in (b) and (e).

As expected, the Si-C mode grows, narrows and shifts to higher wavenumbers with increasing temperature due to the proceeding crystallization process. On the other hand, the Si-H mode decreases with increasing temperature and vanishes completely at a certain temperature, which depends on both the Si content in the layers and the annealing method. The Si-C mode reaches its maximal height for the highest annealing temperature of 1100°C for all samples, but the absolute height decreases with increasing Si content. This is not surprising as the Si-C bond density is proportional to the area of the Si-C mode. Additionally, with increasing Si content, the Si-C bond density decreases due to the increasing density of Si-Si bonds.

To examine the relationship between the H effusion and the onset of the crystallization process, evaluation of the FTIR spectra in Fig. 4.4 was performed. The position of the Si-C mode is depicted together with the area of the Si-H absorption mode. The latter was calculated by fitting the Si-H mode with two Gaussian peaks as described in section 3.2.3, summing them up and integrating the resulting function. No calculation of the Si-H bond density from the integrated absorption mode according to Eq. 3.12 was conducted due to the wide range of proportionality constants $Q_{\text{Si-H}}$ reported in literature [68]. This results from the fact that all changes in back bonding influence the oscillator strength of a specific bond and therefore the factor Q_ν relating the oscillator strength and the bond density. As a change in back bonding corresponds to a variation of stoichiometry, one expects different $Q_{\text{Si-H}}$ for different Si contents. Results from literature prove the difficulty of choosing the right $Q_{\text{Si-H}}$, as they show that the determination of H concentration from FTIR spectra for a-Si$_{1-x}$C$_x$ deviates strongly from the results from nuclear methods [141]. Therefore, the integrated Si-H$_n$ mode to observe H effusion (squares in Fig. 4.4) is used. The position of the Si-C mode is plotted as triangles in Fig. 4.4.

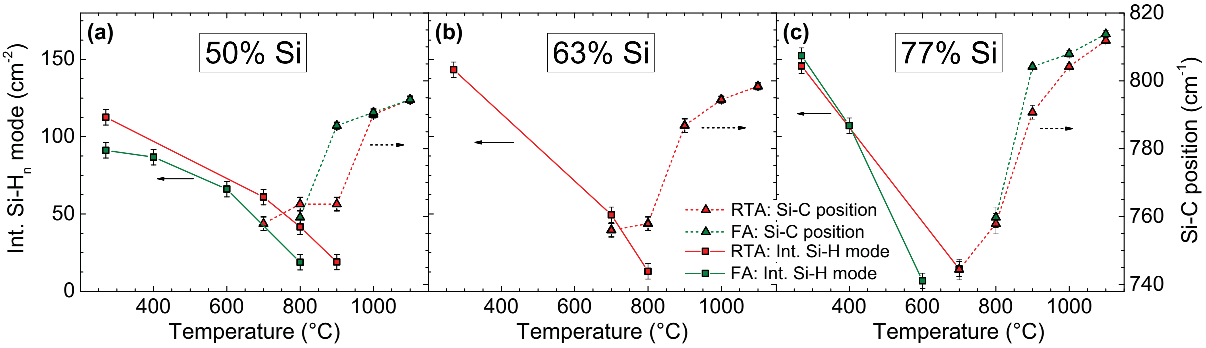

Figure 4.4: Evaluation of the FTIR spectra from Fig. 4.3. On the left-hand ordinate, the integrated Si-H$_n$ absorption mode is shown for Si$_{0.50}$C$_{0.50}$ (a), Si$_{0.63}$C$_{0.37}$ (b) and Si$_{0.77}$C$_{0.23}$ samples (c). Its development reflects the H effusion from the layers. The right-hand ordinate represents the position of the Si-C main vibration for all three Si contents. It represents the crystallization process of the SiC phase in the samples.

First of all, the initial amount of Si-H bonds is significantly lower in a-Si$_{0.50}$C$_{0.50}$:H samples (Fig. 4.4 (a)) than in a-Si$_{0.63}$C$_{0.37}$:H and in a-Si$_{0.77}$C$_{0.23}$:H samples (Fig. 4.4 (a), (b) and (c)), respectively. The nearby explanation is an increasing amount of C-H bonds for increasing C content. Indeed, an increase of the C-H$_n$ mode around 2900 cm^{-1} (not shown here) can be observed for a decreasing Si content.

The second observation concerns the temperature (T_{out}) when the Si-H mode vanishes. At T_{out} complete H effusion is assumed, knowing well that strictly speaking only the detection limit of FTIR measurements is reached and a small amount of H can still be present in the layers. In the case of RTA (red data points), T_{out} decreases from 1000°C for Si$_{0.50}$C$_{0.50}$ via 900°C for Si$_{0.63}$C$_{0.37}$ down to 800°C for Si$_{0.77}$C$_{0.23}$. The use of FA (green data points) reduces T_{out} by about 100°C for every Si content. The dependence of T_{out} from the Si content will be discussed in Sec. 4.5.

The difference of T_{out} for FA and RTA could have two reasons: The trivial one would be that the real temperatures of the samples treated by RTA and FA differ about 100°C. However, this can be excluded because if the final annealing temperature were 1000°C instead of 1100°C for RTA, it could not lead to the formation of Si and SiC NC of the same size as the FA process at 1100°C (cf. Fig. 4.2). The second possibility is the kinetics of H effusion. As FA takes 60x longer than RTA, H has more time for effusion in the case of FA. As the diffusion coefficient depends on the temperature as well, at a certain temperature 2 min RTA is enough time for complete H effusion.

A third observation concerns the correlation between T_{out} and the temperature where the Si-C mode starts shifting to higher wavenumbers (T_{shift}): T_{shift} indicates the onset of SiC crystallization. Before annealing, the wavenumber of the Si-C mode around 760 cm^{-1} does not differ a lot between the different Si contents. After annealing at 1100°C, the difference is quite significant and ranges from 795 cm^{-1} for $\mathrm{Si}_{0.50}\mathrm{C}_{0.50}$ (a) to about 810 cm^{-1} for $\mathrm{Si}_{0.77}\mathrm{C}_{0.23}$ (c). As there is no reason for the Si-C bonds to be stronger if there is more Si in the network, the reason for this peak shift stays unclear. Comparing the H effusion and the SiC crystallization, one can state that for all Si contents T_{out} is lower than T_{shift}. Regarding the RTA results (red data in Fig. 4.4), T_{shift} is estimated to be between 900°C and 1000°C for $\mathrm{Si}_{0.50}\mathrm{C}_{0.50}$, around 900°C for $\mathrm{Si}_{0.63}\mathrm{C}_{0.37}$, and between 800°C and 900°C for $\mathrm{Si}_{0.77}\mathrm{C}_{0.23}$. This could mean that H effusion is a necessary condition for SiC crystallization. It is easy to imagine that the open C and Si bonds after H effusion facilitates the rearrangement of the Si-C bonds from the amorphous to the crystalline state. But it is also possible that there is no connection between the H effusion and the onset of SiC crystallization and that the observed decrease in T_{shift} results from a decease in crystallization temperature with increasing Si content. This question will be discussed in detail at the end of this chapter.

As explained in Sec. 3.2.2, the use of both methods to estimate the SiC crystallinity is necessary to judge if reliable conclusions can be drawn or not. Therefore, the SiC peak position of all samples treated so far are once again depicted in Fig. 4.5 (a) and the results from the Gauss/Lorentz peak fitting of the Si-C vibration mode are plotted in Fig. 4.5 (b).

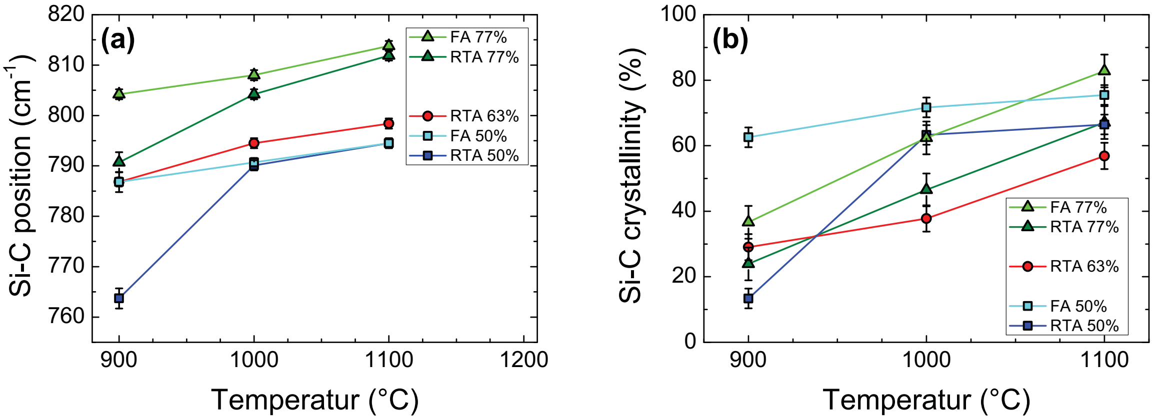

Figure 4.5: Estimation of the SiC crystallinity with the help of the position of the Si-C vibration in (a) and with the results of the fitting of the Si-C vibration mode in (b).

The peak positions in Fig. 4.5 (a) shift to higher wavenumbers with increasing temperature for all samples. The peak position after the 1100°C anneals depends on the Si content but not on the annealing method. For lower temperatures, the peak position and therefore the SiC crystallinity is lower for RTA samples than for FA samples. The peak position does not allow a comparison of the SiC crystallinity of samples with different Si contents. In principle, this is possible with the fitting method depicted in Fig. 4.5 (b). All trends from the peak position method are qualitatively confirmed by the peak fitting method for a fixed Si content. The error bars in Fig. 4.5 (b) refer to the relative error of the fitting. Unfortunately, the absolute error on SiC crystallinity is about 20% due to the strong correlation of the a-Si-C and the Si-N vibration mode. Taking into account this uncertainty, no reliable statement can be made whether the SiC crystallinity is a function of the Si content of the layers or not. However, the dependence of the SiC crystallinity on the Si content - if any - is not very strong because this would be visible in the data.

4.1.3 Si crystallinity

The Si crystallinity is determined with the help of Raman spectra depicted in Fig. 4.6 in order to complete the picture of the crystallization process in Si$_x$C$_{1-x}$ layers.

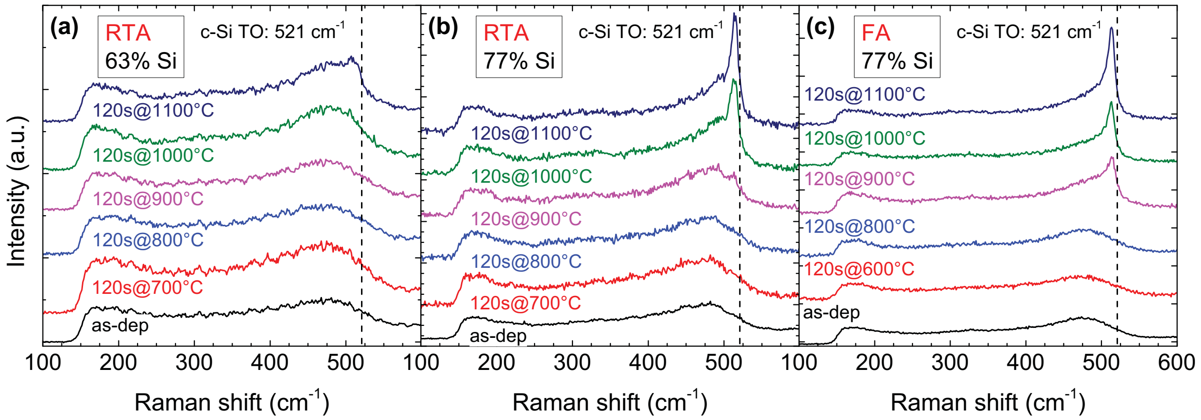

Figure 4.6: Raman spectra of the temperatures series counducted by RTA (a) for Si$_{0.63}$C$_{0.37}$ samples and by RTA (b) and FA (c) for Si$_{0.77}$C$_{0.23}$ samples.

As the formation of the Si phase is expected for Si rich layers, Raman spectra were performed for Si$_{0.63}$C$_{0.37}$ and for Si$_{0.77}$C$_{0.23}$ samples only. For the Si$_{0.77}$C$_{0.23}$ samples treated by FA, (Fig. 4.6 (c)) the c-Si TO mode can clearly be observed after the 900°C annealing step (pink). At the same temperature, the c-Si TO mode is still very weak in case of Si$_{0.77}$C$_{0.23}$ samples treated by RTA (pink spectrum in Fig. 4.6 (b)). In both FA and RTA Si$_{0.77}$C$_{0.23}$ samples, the c-Si TO mode increases and shifts towards 521 cm^{-1} for increasing temperatures. In the case of the Si$_{0.63}$C$_{0.37}$ samples treated by RTA (Fig. 4.6 (a)), the c-Si mode is very weak after a 1000°C anneal (green) and gets clearly observable only after the anneal at 1100°C (dark blue). The Si crystallinity values estimated by the subtraction method are plotted in Fig. 4.7. The Si crystallinity is higher for Si$_{0.77}$C$_{0.23}$ samples than for Si$_{0.63}$C$_{0.37}$ samples for all annealing temperatures. A lower Si content must not a priori lead to a lower Si crystallinity as the Si crystallinity is just a value for the c-Si/a-Si ratio. This means that the $Si_{0.63}C_{0.37}$ samples contain more of the a-Si phase after an anneal at 1100°C than the $Si_{0.77}C_{0.23}$ samples.

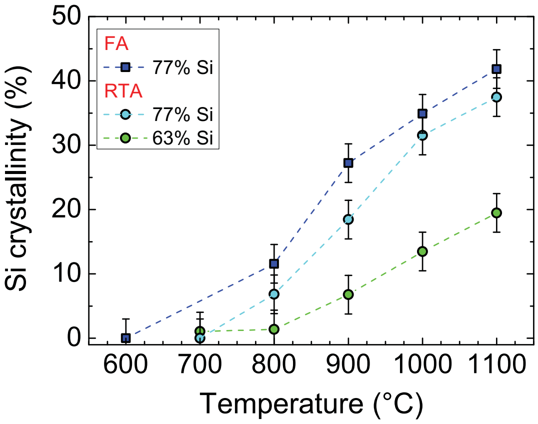

Figure 4.7: Si crystallinity values derived from the Raman spectra in Fig. 4.6 by the subtraction method.

This will be discussed more in Sec. 4.5. Furthermore, Fig. 4.7 shows that in case of $Si_{0.77}C_{0.23}$ samples annealed at 900°C, the Si crystallinity is significantly lower for RTA samples compared to FA samples. This can easily be explained by the difference in Si NC size (cf. Fig. 4.2) at 900°C. For higher temperatures, the difference in Si crystallinity is not significant.

This section about reduction of the thermal budget showed that Si and SiC NC sizes and crystallinity values depend on the annealing method for lower temperatures but become similar at 1100°C. This already strongly indicates that the crystallization process is a thermally activated process. This will be characterized further in the next section.

4.2 Effective activation energy

As already mentioned in Sec. 1.3, for a full characterization of the nucleation process, the mode of nucleation and growth of the material must be known – which is not the case for $Si_xC_{1\text{-}x}$ samples. However, Lui *et al.* [89] proposed a method to estimate the effective activation energy Q for a certain transformed crystalline fraction f and a limited temperature range T ($Q(f)_T$) without referring to a specific kinetic model. Therefore, the time t_f needed at different annealing temperatures to attain a certain fixed value of f is determined. For isothermal annealing, the following relation applies in general:

$$\frac{\mathrm{d}\ln t_{\mathrm{f}}}{\mathrm{d}(1/T)} = \frac{Q(f)_T}{k_{\mathrm{B}}}, \tag{4.1}$$

with the Boltzmann constant k_B [89]. This means that $Q(f)_T$ can be approximated from the linear fit of the plot $\ln t_f$ over $1/T$.

Isothermal annealing of $Si_{0.63}C_{0.37}$ and $Si_{0.77}C_{0.23}$ samples was conducted at 850, 900, 950 and 1000°C between 1 and 3000 min with FA. The SiC and Si NC sizes were determined by GIXRD and depicted for the $Si_{0.63}C_{0.37}$ samples in Fig. 4.8 (a) and (b), respectively. The corresponding SiC and Si NC sizes of $Si_{0.77}C_{0.23}$ samples can be found in App. 7.

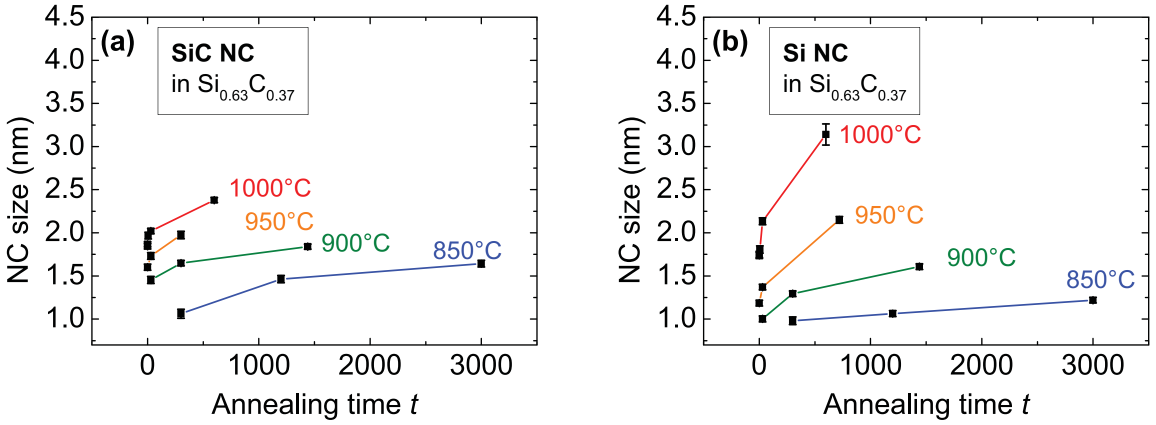

Figure 4.8: SiC (a) and Si (b) NC sizes from $Si_{0.63}C_{0.37}$ samples annealed at different temperatures, derived from GIXRD patterns.

The NC grow fast with short annealing times and the growth slows down for all annealing temperatures with increasing t. As expected, the growth rate increases with increasing annealing temperatures. As the heating ramp is slow, the NC show already a certain size when the final annealing temperature is reached, except for the 850°C samples. It is noteworthy and will be revived in Sec. 4.5 that GIXRD patterns (not shown here), which belong to the same NC size but to different annealing temperatures look very similar.

For the samples annealed for a long time at high temperatures, the Si NC size still increases, but the Si phase starts to decrease (indicated by a decrease of the Si reflex intensity in the GIXRD pattern not shown here). This was also observed for samples in Sec. 4.3.1 and will be discussed in Sec. 4.5.

As most of the crystalline Si and SiC fractions (f_{Si} and f_{SiC}) in this experiment were quite low, it was not possible to obtain reliable values for f_{Si} and f_{SiC} with the help of Raman or FTIR measurements. Therefore, we assume that the crystallized Si and SiC volume ($V_{\mathrm{cryst}}^{\mathrm{Si/SiC}}$) is proportional to the average Si and SiC NC volume ($V_{\mathrm{NC}}^{\mathrm{Si/SiC}}$) and therefore to the Si and SiC NC volume $d_{\mathrm{NC}}^{\mathrm{Si/SiC}}$ cubed:

$$f_{\mathrm{Si/SiC}} = \frac{V_{\mathrm{cryst}}^{\mathrm{Si/SiC}}}{V_{\mathrm{tot}}^{\mathrm{Si/SiC}}} = \frac{V_{\mathrm{NC}}^{\mathrm{Si/SiC}}}{V_{\mathrm{NC\_100}}^{\mathrm{Si/SiC}}} = \frac{\left(d_{\mathrm{NC}}^{\mathrm{Si/SiC}}\right)^3}{\left(d_{\mathrm{NC\_100}}^{\mathrm{Si/SiC}}\right)^3}, \tag{4.2}$$

where $V_{\mathrm{tot}}^{\mathrm{Si/SiC}}$ is the total Si and SiC volume and $V_{\mathrm{NC\_100}}^{\mathrm{Si/SiC}}$ is the Si and SiC NC size, which

corresponds to a Si and SiC crystallinity of 100%. This is assumed to be valid as long as the increase in the crystalline phase (represented by the increase of the GIXRD reflex) is associated with crystal growth (narrowing of the GIXRD reflex). This is the case for all samples used for the determination of $Q(f)_T$.
As Si or SiC crystallinities of 100% were never measured during this thesis, $\left(d_{\mathrm{NC\_100}}^{\mathrm{Si/SiC}}\right)^3$ was determined with the help of the maximum Si and SiC NC volumes $\left(d_{\mathrm{NC\_max}}^{\mathrm{Si/SiC}}\right)^3$ and maximum crystalline fraction $f_{\max}$ ever determined from FA samples, which corresponds to an annealing of 30min@1100°C

$$\left(d_{\mathrm{NC\_100}}^{\mathrm{Si/SiC}}\right)^3 = \frac{\left(d_{\mathrm{NC\_max}}^{\mathrm{Si/SiC}}\right)^3}{f_{\max}}. \tag{4.3}$$

These values are summarized in Tab. 4.1. The fitting errors of the NC sizes are small in this section as all samples are from the same batch, the GIXRD measurements were conducted in a short time window after annealing, and the evaluation was performed in exactly the same way for all GIXRD patterns.

Table 4.1: Values to estimate the overall activation energy for a certain crystalline fraction f ($Q(f)$) for Si and SiC crystallization in $\mathrm{Si_{0.63}C_{0.37}}$ and $\mathrm{Si_{0.77}C_{0.23}}$ samples. In the last column the $Q(0.4)$ value determined from the linear fit of the $\ln t_{0.4}$ over $1/T$ plots are given.

Si content (%)	**Phase**	$f_{\max}$	**NC size** (nm)	$(d_{\mathrm{NC\_max}})^3$ (nm^3)	$(d_{\mathrm{NC\_100}})^3$ (nm^3)	$\boldsymbol{Q(0.4)}$ (eV)
63	Si	0.3 ± 0.1	3.5 ± 0.1	(43 ± 4)	(143 ± 60)	**4.4...5.1**
63	SiC	0.8 ± 0.2	2.6 ± 0.1	(18 ± 2)	(22 ± 8)	**2.1...3.5**
77	Si	0.6 ± 0.1	4.7 ± 0.1	(104 ± 7)	(173 ± 40)	**1.8...4.0**
77	SiC	0.8 ± 0.2	2.6 ± 0.1	(18 ± 2)	(22 ± 8)	**2.6...5.6**

One can now plot $f_{\mathrm{Si/SiC}}(t)$ for 850, 900, 950 and 1000°C. To obtain a t_{f} for a certain f, a reliable intra- and extrapolation of the $V_{\mathrm{NC}}^{\mathrm{Si/SiC}}(f)$ plots are necessary. This was done by using Eq. 1.13 and shifting it on the time axis by t_0

$$f = 1 - \exp(-A(t - t_0)^n). \tag{4.4}$$

With the shift $t - t_0$ it was taken into account that for low heating rates there is always a certain f present in the samples when the annealing temperature is reached after the time t_0. The meaning of the fitting parameter n and A is rather complex and must not be considered in the case of the simple estimation aimed at here. The fitting worked well for Si and SiC NC as depicted for the $\mathrm{Si_{0.63}C_{0.37}}$ samples in Fig. 4.9 (a) and (b), respectively. The corresponding fits for $\mathrm{Si_{0.77}C_{0.23}}$ samples can be found in App. 7. Fig. 4.9 shows that some of the fits contain only three data points. This is obviously not enough to obtain meaningful results concerning the three free parameters in Eq. 4.4. However, this is not the aim of this analysis as the described method to estimate the activation energy contains no fitting at all [89]. It was decided to conduct a data fitting anyway to obtain a better intra- and extrapolation of the data sets.

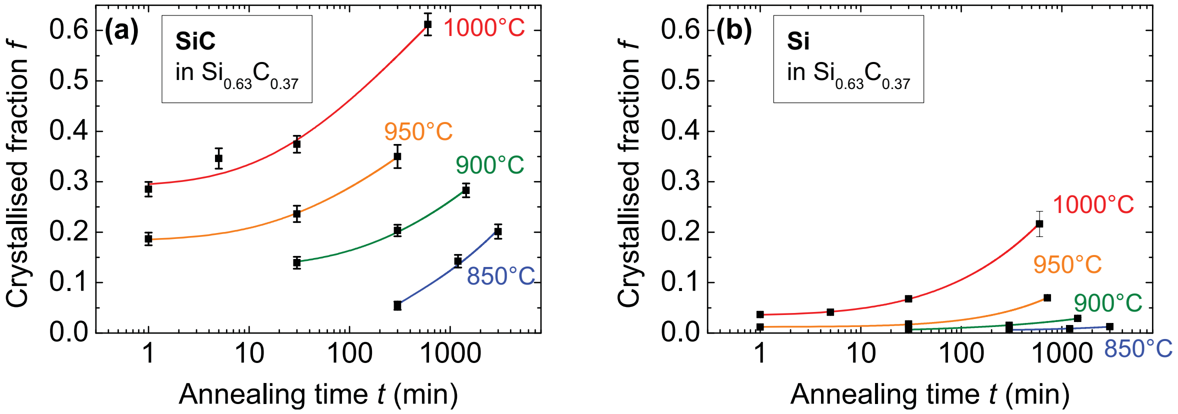

Figure 4.9: Developement of crystallized SiC (a) and Si (b) fractions f in Si$_{0.63}$C$_{0.37}$ samples with annealing time for four different annealing temperatures.

From the fits in Fig. 4.9, the time to reach 40% crystalline fraction $t_{0.4}$ is determined and plotted over $1/T$ (not shown here). The value of 40% crystalline fraction was chosen because all data sets contain either this value or lie below it and can therefore be extrapolated (cf. App. 7 for Si$_{0.77}$C$_{0.23}$ samples). According to Eq. 4.1, linear fits of $t_{0.4}$ versus $1/T$ give an estimation for $Q(0.4)$ in the temperature range between 850 and 1000°C and are summarized in the last column of Tab. 4.1. $Q(0.4)$ ranges from 1.8 to 5.6 eV and thus lies in the expected range of some eV (cf. Sec. 1.3.2), although this method contains simplifying assumptions and large errors. A lower $Q(0.4)^{\mathrm{Si}}$ is observed in Si$_{0.77}$C$_{0.23}$ than in Si$_{0.63}$C$_{0.37}$ samples. A corresponding comparison for $Q(0.4)^{\mathrm{SiC}}$ is not possible as the errors are too large. In the Si$_{0.63}$C$_{0.37}$ samples, $Q(0.4)^{\mathrm{SiC}}$ is significantly smaller than $Q(0.4)^{\mathrm{Si}}$. A corresponding comparison for Si$_{0.77}$C$_{0.23}$ samples is not possible due to the large errors.
A possible explanation for this result could be the following: Theoretical calculations of self-diffusion in 3C-SiC from A. Mattausch [142] show that the activation energy of C self-diffusion is smaller than for Si self-diffusion for both Si and C rich 3C-SiC. Furthermore, for Si rich material, C diffusion occurs via interstitials and vacancies whereas Si diffusion occurs preferentially via interstitials while vacancies contribute only in strongly n-doped Si rich material [142]. Provided that these calculations can be applied for multicrystalline Si$_x$C$_{1\text{-}x}$ layers, they could explain the obtained results as follows: The Si$_x$C$_{1\text{-}x}$ layers are considered to be increasingly n-doped with increasing Si content due to increasing unintentional N incorporation (cf. Sec. 3.2.3). In Si$_{0.63}$C$_{0.37}$ samples, SiC crystallization is favored over Si crystallization as it is determined by C diffusion, which has a lower activation energy than Si diffusion and occurs via both interstitials and vacancies. For

$Si_{0.77}C_{0.23}$ samples, the n-doping could be high enough for Si diffusion to occur not only via interstitials but also via vacancies. Therefore, Si crystallization is facilitated with increasing Si content.
The findings from this section will be discussed again with regard to other crystallization results in Sec. 4.5.

4.3 Two-step anneal

In the last two sections, we have seen that a suppression of SiC crystallization by choosing a certain annealing temperature is not possible. Therefore, a two-step annealing process will be used in order to increase the c-Si to c-SiC ratio. As one can expect a major influence for fast heating ramps and high annealing temperatures, the zone melting crystallisation (ZMR) setup is used, which allows for both. First of all, one has to point out that the ZMR setup is not as clean as the FA or the RTP setup and therefore not suitable for solar cell processes. However, for only structural investigations, the ZMR furnace is a suitable setup to achieve temperatures between 800 and 1350°C.

4.3.1 Maximum conversion rate of Si

Before conducting the two-step anneal in the ZMR setup, it is attempted to determine the optimum temperatures for nucleation and crystal growth.

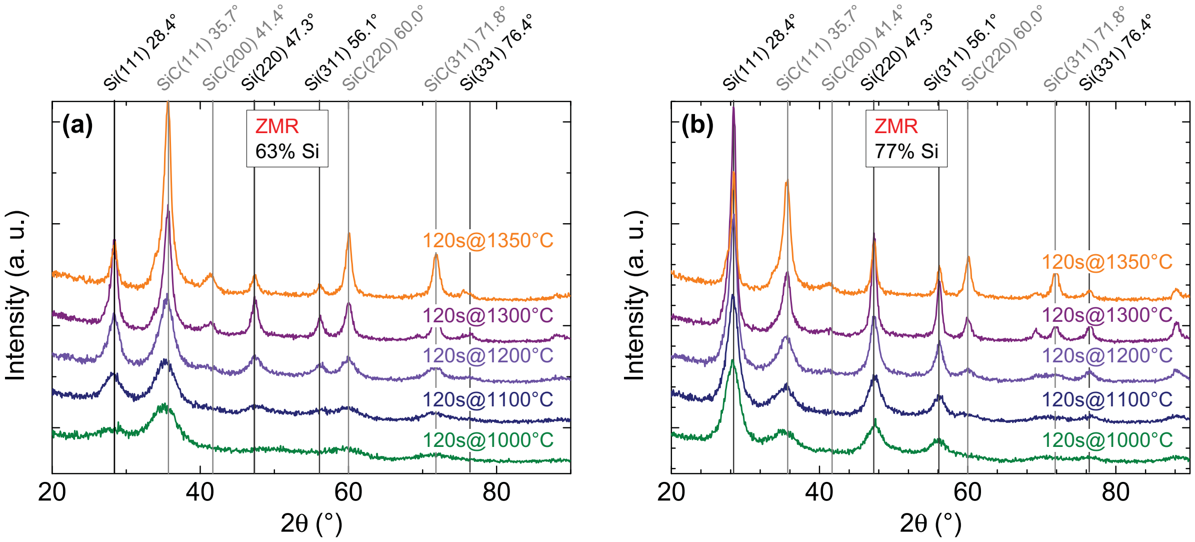

Figure 4.10: GIXRD patterns of $Si_xC_{1\text{-}x}$ samples annealed in the ZMR setup with $x = 0.63$ (a) and $x = 0.77$ (b).

Therefore, the $Si_{0.63}C_{0.37}$ and $Si_{0.77}C_{0.23}$ samples were treated in the ZMR furnace for 600s@800°C for H effusion and performed a subsequent annealing step between 1000 and 1350°C for 120 s. The corresponding GIXRD patterns are depicted in Fig. 4.10 (a) and (b), respectively. For both Si contents, an increase in intensity of Si and SiC reflexes combined with a narrowing of the peaks can be observed between 1000 and 1300°C. However, at 1350°C, the Si reflexes show a clear decrease in intensity while the SiC reflexes keep growing. At the left-hand side of the SiC(111) reflex, a weak shoulder occurs at $2\theta \approx 34°$ which proves the formation of the high temperature polytype 4H-SiC. The Si and SiC NC grain sizes derived from the patterns in Fig. 4.10 are depicted in Fig. 4.11.

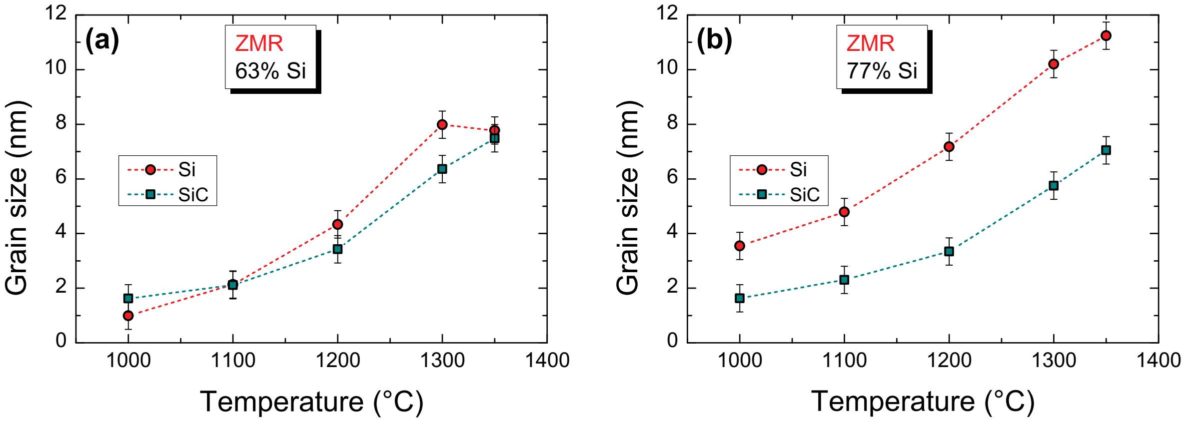

Figure 4.11: The NC grain sizes calculated from GIXRD patterns of Si_xC_{1-x} samples annealed in the ZMR setup with $x = 0.63$ (a) and $x = 0.77$ (b).

In $Si_{0.63}C_{0.37}$ samples (Fig. 4.11 (a)), the Si and SiC NC sizes increase up to a temperature of 1300°C and reach a value of (8.0 ± 0.5) nm and (6.4 ± 0.5) nm for Si and SiC, respectively. With an further increase to 1350°C, the Si NC size stays the same while the SiC NC size keeps growing. In the case of $Si_{0.77}C_{0.23}$ (Fig. 4.11), the difference between Si and SiC NC size is much more pronounced than in $Si_{0.63}C_{0.37}$. Both Si and SiC NC grow continuously up to the final temperature of 1350°C where Si NC reach a value of (11.2 ± 0.5) nm and SiC NC a value of (7.0 ± 0.5) nm. Comparing the NC sizes in $Si_{0.63}C_{0.37}$ and in $Si_{0.77}C_{0.23}$, it turns out that for a given temperature, Si NC are always bigger in $Si_{0.77}C_{0.23}$ samples then in $Si_{0.63}C_{0.37}$ samples while the SiC NC size is the same at a given temperature for $Si_{0.63}C_{0.37}$ and $Si_{0.77}C_{0.23}$. The dependence of the Si NC size on the Si content of the layers and the independence of the SiC NC size on the Si content was also observed for FA and RTA samples (Fig. 4.2). This will be discussed together with these results in Sec. 4.5.

To investigate the Si crystallinity of ZMR samples, $Si_{0.63}C_{0.37}$ and $Si_{0.77}C_{0.23}$ layers deposited on quartz substrate were investigated by Raman spectroscopy. As the adherence of the layers on quartz is lower than on Si substrate, flaking was observed at high temperatures. For $Si_{0.63}C_{0.37}$ it started at 1300°C and for $Si_{0.77}C_{0.23}$ at 1350°C. Therefore, a reliable evaluation of Si crystallinity was only possible up to 1325°C for 77% samples and up to

1200°C for 63% samples. The according Raman spectra and derived Si crystallinities are depicted in Fig. 4.12 (a) and (b).

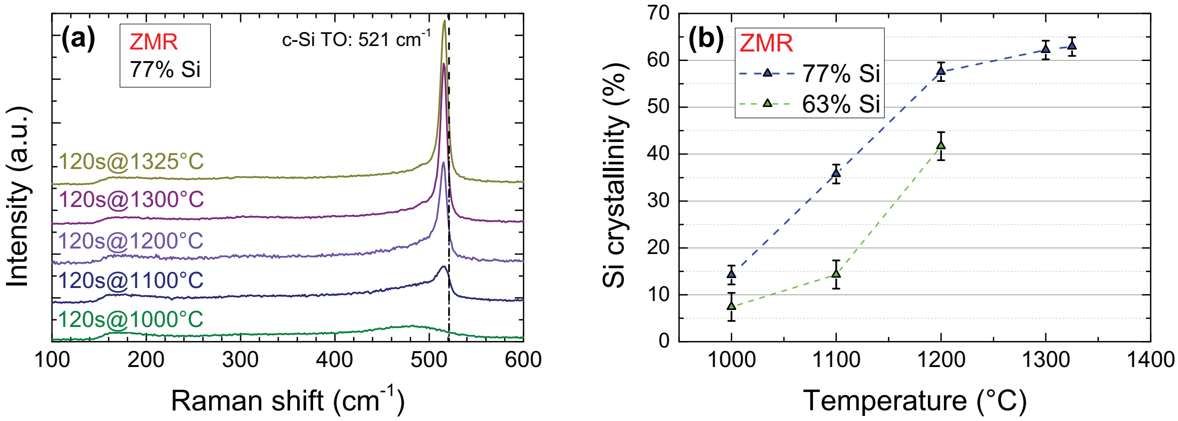

Figure 4.12: Raman spectra of $Si_{0.77}C_{0.23}$ samples annealed in the ZMR setup (a) and Si crystallinities (b) derived from Raman spectra for $Si_{0.77}C_{0.23}$ samples (blue) and $Si_{0.63}C_{0.37}$ samples (green).

Prior to comparing the Si NC size development with the trend of Si crystallinity, one must note that the absolute annealing temperatures of the samples on quartz substrate was about 100°C lower than of samples on Si substrate due to the inaccuracy of the calibration method. This was concluded from the comparison of GIXRD patterns of identical layers deposited on Si and on quartz substrate (not shown here). GIXRD patterns of the samples on quartz substrate corresponds to patterns of samples on Si substrate treated at about 100°C lower annealing temperature. The Raman spectra in Fig. 4.12 (a) show an increase in intensity accompanied with a peak shift towards the c-Si TO mode and a peak narrowing up to 1200°C. This is reflected by the increase of Si crystallinity in this temperature range (Fig. 4.12 (b)). Then the peak narrowing and shifting reduces and a saturation of the Si crystallinity around 63% is observed at temperatures above 1200°C.

Firstly, it should be stated that from classical nucleation theory one would expect a clear decrease of Si crystallinity near the melting point of Si because the undercooling at this temperatures is small, therefore the critical nucleus radius is high, and the nucleation rate is correspondingly low. This suggests that despite the high heating rate, a significant amount of Si nuclei were formed during the ramping up time. This assumption was proven by the following experiment: A $Si_{0.63}C_{0.37}$ and a $Si_{0.77}C_{0.23}$ sample were annealed with the minimum possible ZMR annealing time at 1300°C. The samples were heated up and the ZMR lamps were shut down immediately when 1300°C were reached. These samples were compared to the $Si_{0.63}C_{0.37}$ and $Si_{0.77}C_{0.23}$ samples annealed for 120s@1300°. The Si and SiC NC sizes derived from GIXRD patterns and the intensity ratios of the Si(111) and the SiC(111) XRD reflexes are summarised in Tab. 4.2. The Si and SiC NC sizes are the same within the fitting error for the short and the long annealing process. This strengthens the assumption that Si nucleation mainly takes place during the ramping up time and that very short annealing times are sufficient for crystal growth.

Table 4.2: NC sizes derived from GIXRD patterns (not shown here) to compare samples annealed for 120 s at 1300°C with samples annealed as short as possible at 1300°C in the ZMR setup. Additionally the ratio of XRD intensities Si(111)/SiC(111) is listed for the 1300°C samples and for the two-step process described in the next section.

Si content (%)	**Temperature** (°C)	**Si NC size** (nm)	**SiC NC size** (nm)	**Si(111)/SiC(111)**
77	1300 short	10.2 ± 0.5	5.8 ± 0.5	(4.4 ± 0.3)
77	1300 long	10.9 ± 0.5	5.3 ± 0.5	(3.4 ± 0.2)
63	1300 short	8.0 ± 0.5	6.4 ± 0.5	(1.0 ± 0.1)
63	1300 long	8.0 ± 0.5	5.7 ± 0.5	(0.7 ± 0.1)
77	1200 short	± 0.5	± 0.5	(4.6 ± 0.4)
77	1200 long	± 0.5	± 0.5	(3.9 ± 0.3)
63	1200 short	± 0.5	± 0.5	(1.0 ± 0.1)
63	1200 long	± 0.5	± 0.5	(0.7 ± 0.1)

It is remarkable that the Si(111)/SiC(111) ratio changes in favor of Si(111) for the short annealing time in both $Si_{0.63}C_{0.37}$ and $Si_{0.77}C_{0.23}$ samples. This is probably due to the fact that at 1300°C SiC is still in strong undercooling conditions, meaning that the transformation rate is still high, thus leading to the formation of a higher fraction of the SiC crystalline phase with longer annealing time.

Let us now come back to the initial experiment of increasing annealing temperatures and compare the Si crystallinities (Fig. 4.12 (b)) with the Si NC sizes (Fig. 4.11 (b)). It shows that during saturation of Si crystallinity there is still a significant increase in Si NC size. This effect of Si NC growth without corresponding increase of c-Si phase probably starts even at lower temperatures (about 1100°C) due to the temperature derivation mentioned above. This behaviour was also observed for long annealing times at higher annealing temperatures in Sec. 4.2 and can be attributed to Ostwald ripening. A vanishing of small NC in favor of larger Si NC will lead to the observed increase in Si NC size without a significant increase in the overall Si phase. Ostwald ripening can explain the increasing Si NC size at nearly constant Si crystallinities but not the observed decrease of intensity of the Si reflexes compared to the SiC reflexes at 1350°C (Fig. 4.10), which will be discussed in Sec. 4.5.

Another issue to address is the saturation of the Si crystallinity around 63%. From Sec. 3.3.3 we know that the crystallinity obtained from the subtraction method is not an absolute value. The crystallinity of FZ Si determined with this method is 80%. This shows that the observed maximum crystallinity of 63% still contains a significant part of a-Si phase. One reason for this is the fact that the grain boundaries between NC can be considered as amorphous regions as there is no long-range order of the crystal lattice.

Another reason is the dependence of Si crystallization on the Si concentration, which will be discussed in Sec. 4.5.

One can conclude from the Si NC growth behavior, the saturation of the Si crystallinity at 1200°C, and the higher Si(111)/SiC(111) ratios for shorter annealing times that the maximum conversion rate of the a-Si/c-Si transition lies between 1100°C and 1200°C and a decrease of annealing time is beneficial for the c-Si/c-SiC ratio. This result will be exploited in the next section.

4.3.2 Separation of nucleation and crystal growth

The last section showed that also under ZMR conditions it is difficult to separate the nucleation and the crystal growth process for Si and SiC NC because a significant part of nucleation takes place during the inevitable preanneal step for H effusion and during ramping up time. Even though a complete separation of nucleation and crystal growth is not possible under ZMR conditions, one can sill try to increase the c-Si to c-SiC ratio by a two-step annealing process:

1. A **low temperature step** for Si nucleation: In the ideal case, there would be a temperature at which only Si nucleation takes place. However, the prior experiments showed that the onset of Si and SiC crystallization is at very close temperatures, which are only influenced by the Si content. Therefore, 1000°C for 120 s was taken as preanneal temperature because clear Si XRD reflexes occur for both $Si_{0.63}C_{0.37}$ and $Si_{0.77}C_{0.23}$ samples (Fig. 4.10). This annealing step was successfully used to replace the H effusion step at 800°C without blistering of the samples.

2. A **high temperature step** at the maximum growth rate of Si: Therefore, a temperature of 1200°C was chosen as discussed in the previous section. The short annealing time of 1 s gives further SiC crystallization as little time as possible.

To check if this separation of nucleation and crystal growth works, the following experiment was performed: $Si_{0.63}C_{0.37}$ and $Si_{0.77}C_{0.23}$ samples were annealed for 120s@1000°C and subsequently for 1s@1200°C. Then the order of the annealing was changed and the high temperature process was performed prior to the low temperature process without changing the annealing times at the respective temperatures. The resulting GIXRD patterns are depicted in Fig. 4.13. It is clearly visible that the samples annealed for 120@1000°C and 1s@1200°C (purple) show stronger crystallization than the samples annealed in reversed order (green) for both Si contents. This was proven by the calculation of the Si and SiC NC sizes (bars in Fig. 4.14) and the Si crystallinity (stars in Fig. 4.14). The Si and SiC NC sizes decrease significantly if there is no preanneal step at 1000°C for both Si contents. The same applies for the Si crystallinity. As the overall thermal budget was the same for all samples, the differences in crystallization behavior must be a result from different nucleation and crystal growth. Nucleation takes place during the preanneal step at 1000°C and nuclei can grow fast during the final anneal step at 1200°C. If the sample is heated up directly to 1200°C, non or only a little amount of Si and SiC nuclei can build and correspondingly no significant NC growth occurs at 1200°C. Probably most of the observed NC build during the subsequent annealing step at 1000°C as the green patterns in Fig. 4.13 resemble to the green patterns in Fig. 4.10, which were annealed for 600s@800°C followed by 120s@1000°C.

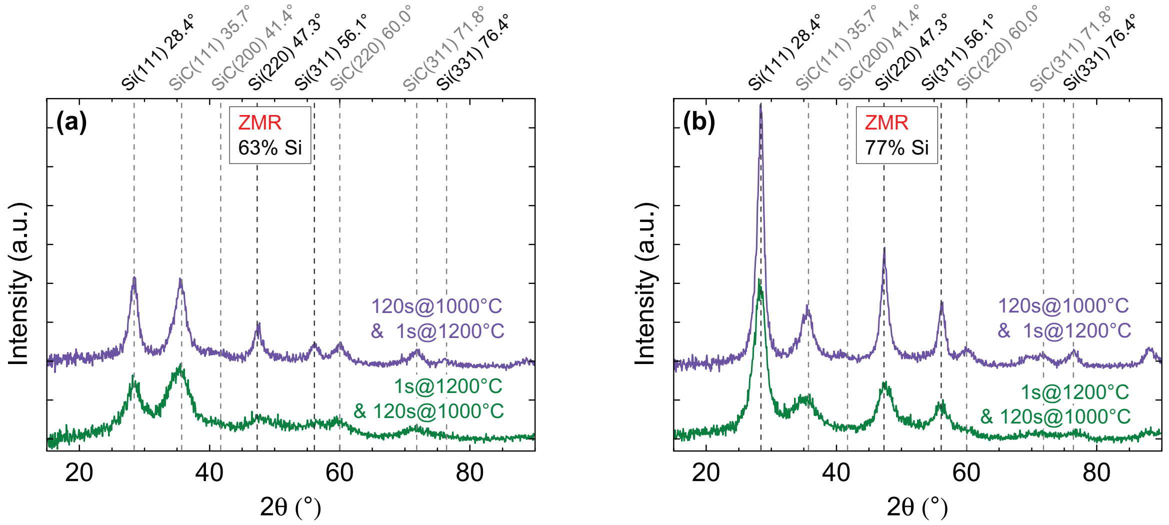

Figure 4.13: GIXRD results of (a) Si$_{0.63}$C$_{0.37}$ and (b) Si$_{0.77}$C$_{0.23}$ samples annealed with a 2 step process for 120@1000°C & 1s@1200°C (purple) and in reversed order (green).

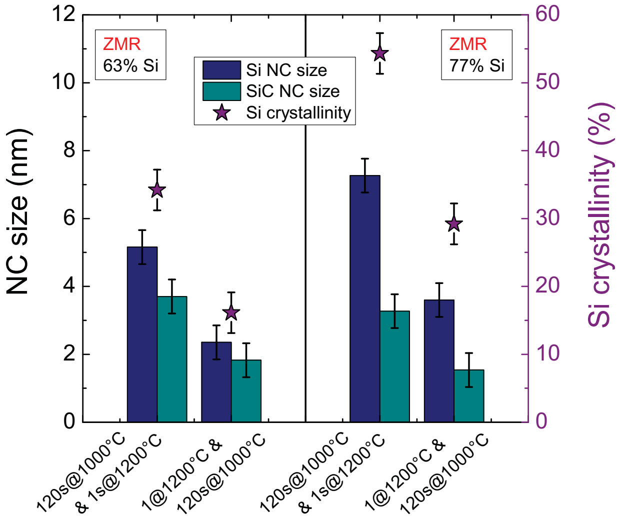

Figure 4.14: Si NC and SiC NC sizes (bars, lef-hand ordinate) from the two-step annealing experiment and Si crystallinity (stars, right-hand ordinate).

The assumption that a short annealing time is beneficial for the c-Si/c-SiC ratio can be verified by a comparison of the Si(111)/SiC(111) intensity ratios of the GIXRD reflexes of the 1s@1200°C process and the 120s@1200°C process from the previous section. The results listed in Tab. 4.2 show a relative reduction in Si phase for the long annealing time and therefore prove this assumption.

Another conclusion can be drawn from the two-step experiment. It proves indirectly that the H effusion step at 800°C used in the experiment in the previous section also acts as preanneal step for nucleation. Otherwise the observed Si and SiC NC sizes and Si crystallinity (see Tab. 4.2) could not be the result of a maximum short annealing step at 1300°C. This assumption is further reinforced by repeating the two-step experiment with a preanneal temperature of 900°C and obtaining very similar results as in the 1000°C preanneal experiment (not shown here).

The results prove that the crystallization process can be influenced by a two-step ZMR annealing process. As the reduction of annealing time from hours in case of FA to seconds in case of RTA and ZMR shows promising results in terms of crystallization control, we will investigate in the next experiment if a further decrease of annealing time to the millisecond range is possible.

4.4 Nonequilibrium crystallization

$Si_{0.50}C_{0.50}$, $Si_{0.63}C_{0.37}$ and $Si_{0.77}C_{0.23}$ samples were treated with flash lamp annealing (FLA). It turned out that both the Si content of the samples and the FLA parameter must be chosen carefully to receive NC formation. This will be discussed in the first part of this section. In the second part, the formation of Si and SiC NC by FLA is investigated in detail. The RTA samples already treated in Sec. 4.1 serve as comparative samples to judge the success of the FLA process.

4.4.1 Flash lamp anneal parameter selection

Successful FLA was only possible for layers with a **Si content** of 77% and 63% but not for 50%. The $Si_{0.50}C_{0.50}$ FLA samples – which had been treated with a preanneal step of 5min@700°C and flashed with energies between 28 and 47 J/cm^2 – all showed a white haze on the surface. SEM images (see Fig. 4.15 (a)) reveal that the origin of the white haze is strong blistering of the layers, which has its reason in the explosive effusion of H during the flash. Obviously, the preanneal step was not hot and/or long enough for complete H effusion. This can be substantiated by an RTA treatment of the $Si_{0.50}C_{0.50}$ samples and evaluation of the corresponding FTIR measurements (Fig. 4.15 (b)). The Si-H vibration mode in the range of 2000...2200 cm^{-1} reveals that after 120s@900°C (blue) there is still a considerable amount of Si-H bonds in the layers. Even after the FLA there are still Si-H bonds visible in the FTIR spectra of Si$_{0.50}$C$_{0.50}$ samples (not shown here). As the hottest and longest preanneal that is possible in the FLA setup is 2min@800°C, it is not possible to drive out all the hydrogen before FLA to avoid blistering of the stoichiometric Si$_{0.50}$C$_{0.50}$ samples. Therefore, no further investigation of Si$_{0.50}$C$_{0.50}$ samples was conducted in this work.

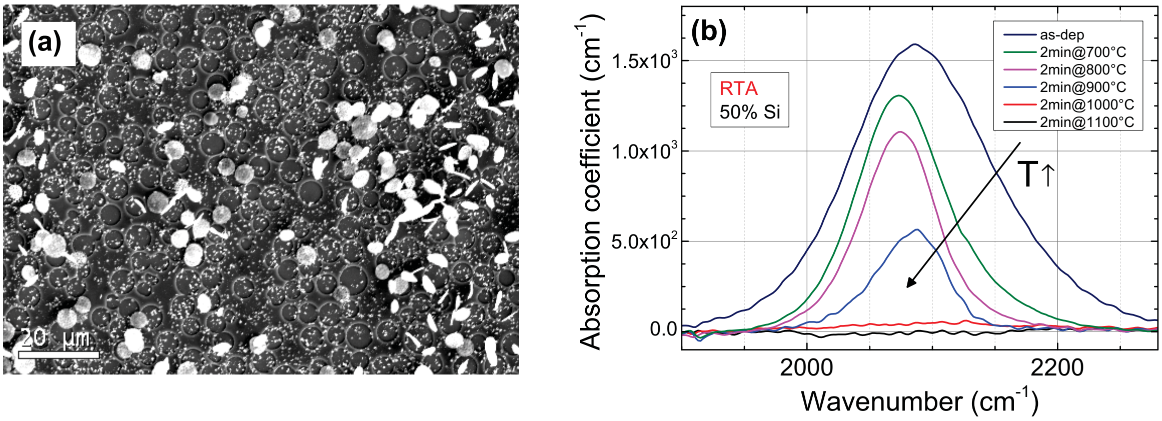

Figure 4.15: In (a) a SEM image of strong blistering of a Si$_{0.50}$C$_{0.50}$ film after FLA is shown. In (b) the development of the FTIR Si-H mode with increasing annealing temperatures is plotted for the of the Si$_{0.50}$C$_{0.50}$ film. It shows that 700°C is not hot enough for complete H effusion: After 2min@700°C there is still a significant Si-H peak (green).

A wide range of **flash energies** were applied to Si$_{0.63}$C$_{0.37}$ and Si$_{0.77}$C$_{0.23}$ films. Since it is not clear which temperatures are achieved at each energy, it is necessary to check whether solid phase crystallization is in fact taking place or whether some flash energies melt or otherwise damage the sample. For flash energies above 40 and 47 J/cm^2 for Si$_{0.63}$C$_{0.37}$ and Si$_{0.77}$C$_{0.23}$, respectively, the GIXRD patterns retain their general shape but the reflection intensities show a dependency on the wafer orientation concerning the ϕ-angle (cf. Sec. 3.1), as shown in Fig. 4.16 for the Si(111)@28.4° reflex.

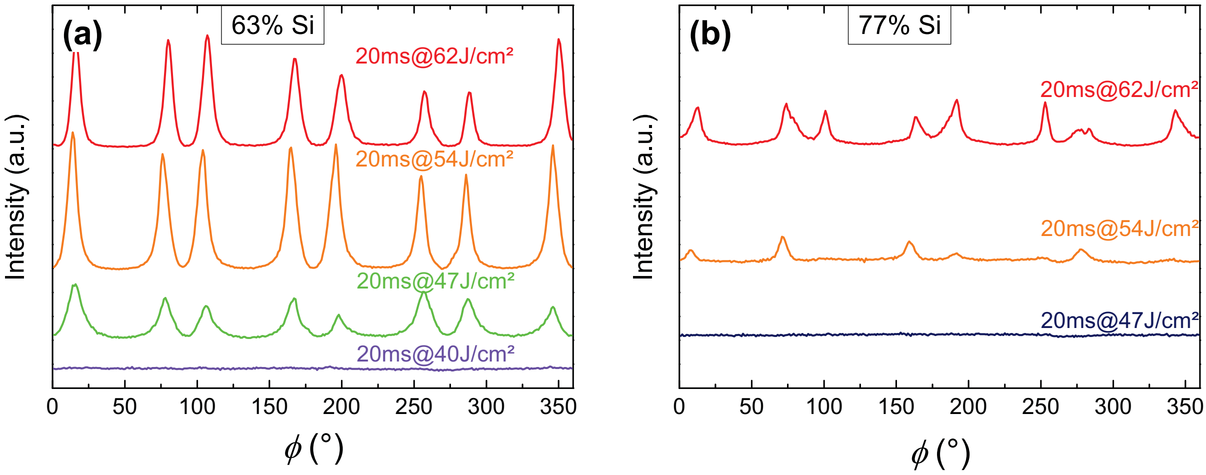

Figure 4.16: The ϕ-orientation dependency of the Si(111) peak at $2\theta = 28.4°$ with increasing FLA energy is shown for Si$_{0.63}$C$_{0.37}$ (a) and Si$_{0.77}$C$_{0.23}$ (b) layers. It is evident that for Si$_{0.63}$C$_{0.37}$ samples, the ϕ-dependency starts at lower flash energies and is stronger than for Si$_{0.77}$C$_{0.23}$ samples.

A 4-fold symmetry, each with two peaks, is present in $Si_{0.63}C_{0.37}$ films (Fig. 4.16 (a)), which increase in intensity for 54 J/cm^2 and decreases slightly in intensity for 62 J/cm^2. In $Si_{0.77}C_{0.23}$ layers (Fig. 4.16 (b)) the ϕ-dependence only starts at 54 J/cm^2 and increases for 62 J/cm^2. In contrast, the intensity of the SiC reflexes show no dependency on sample orientation in either sample. This means that at a certain flash energy, the orientation of the Si NC is no longer randomly distributed while the SiC grain orientation stays random for all energies. The evaluation of Si and SiC grain sizes from GIXRD spectra acquired at different sample orientations shows that an increase in Si(111) peak intensity at a given orientation is correlated with an increase in Si NC diameter in that particular direction. This behavior is not surprising since the GIXRD intensity is in general positively correlated with the size of crystalline clusters. This is shown in Fig. 4.17 (a) for $Si_{0.63}C_{0.37}$ (blue) and $Si_{0.77}C_{0.23}$ (green).

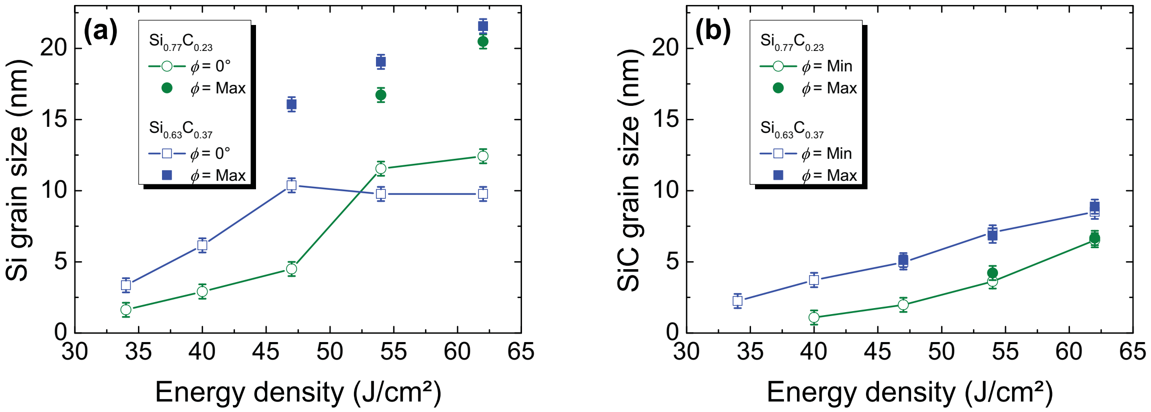

Figure 4.17: Si (a) and SiC (b) grain sizes estimated from the Si(111) and SiC(111) reflex at $2\theta = 28.4°$ and at $2\theta = 31.7°$, respectively. The straight lines connect the data points of measurements done in standard sample orientation referred to $\phi = 0°$. The additional grain sizes at high energies were calculated from diffraction patterns taken at ϕ-angles of maximal intensity for the Si(111) reflex at 28.4°. The Si NC size (a) is a function of both the flash energy and the samples orientation. The SiC NC size (b) stays independent of the sample orientation even for high flash energies but a big difference between the $Si_{0.63}C_{0.37}$ and $Si_{0.77}C_{0.23}$ samples can be observed.

The connected data points represent the GIXRD measurements in standard sample orientation referred to as $\phi = 0°$ while the additional grain sizes (filled symbols) correspond to the spectra taken at the maximal intensity of the Si(111)@28.4° reflex. The largest variation in Si NC size was observed for 63% Si samples flashed for 20 ms at 62 J/cm^2 and ranges from (9.8 ± 0.5) nm to (21.6 ± 0.5) nm. The SiC NC size does not depend on sample orientation and increases continuously with the flash energy for layers with 63% (blue) and 77% (green) Si content, as depicted in Fig. 4.17 (b). The ϕ-dependency of the Si grain size and the very large NC suggest that at high energies, a different crystallization mechanism takes place, perhaps via the Si liquid phase ($T_m(\mathrm{Si}) = 1414°\mathrm{C}$ [65]). To better understand the processes at high temperatures, SEM cross section images of samples were taken with and without ϕ-dependency. Three of them are exemplarily depicted in Fig. 4.18.

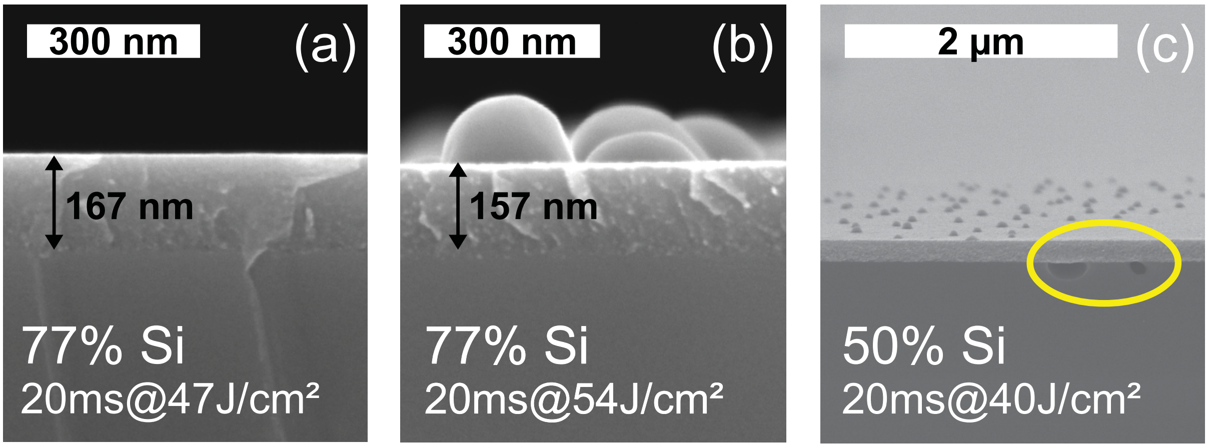

Figure 4.18: SEM images of a $Si_{0.77}C_{0.23}$ FLA sample with ϕ-dependency (a) and a $Si_{0.77}C_{0.23}$ FLA sample without ϕ-dependency (b). The droplets on the surface in (b) indicate the formation of Si liquid phase. In some samples with ϕ-dependency, holes were observed in the substrate under the layer (c).

The cross section in Fig. 4.18 (a) corresponds to the blue curve in Fig. 4.16 (b) and represents a low energy sample without ϕ-dependency while Fig. 4.18 (b) shows a high energy sample from Fig. 4.16 (b) (orange) with obvious ϕ-dependency. Fig. 4.18 (a) shows a smooth $Si_{0.77}C_{0.23}$ layer about 167 nm thick; the $Si_{0.77}C_{0.23}$ layer in Fig. 4.18 (b) is around 10 nm thinner and has lumps on the surface. These were identified as Si lumps with the help of EDX measurements. These Si lumps indicate a high mobility of Si during the FLA process, which suggests the formation of a Si liquid phase. The following considerations show that Si NC may melt during FLA in $Si_{0.77}C_{0.23}$ (this is analogously valid for $Si_{0.63}C_{0.37}$). 47 J/cm^2 corresponds to 1200°C in $Si_{0.77}C_{0.23}$ (this will be shown in the next section). Work by Prucnal *et al.* [143] showed that for SiO_2:Gd layers the temperature to achieve a given nanostructure is 100°C higher in FLA than in RTA. This increases by 100°C per 7 J/cm^2 of flash energy. Assuming these considerations apply also for Si NC, 54 J/cm^2 corresponds to around 1300°C. Taking into account the reduction of the melting temperature with the reduction of crystal size [144, 145], a melting of the Si NC in the layers is likely. The migration of molten Si to the surface could be driven by energy minimization due to reduction of the stress-provoking Si/SiC interfaces and due to volume maximization and surface area minimization of the Si NC. However, the layers cannot be the only origin of the Si lumps on the surface because their total volume estimated from SEM images is around 30% greater than the volume reduction caused by the measured layer shrinkage of 10 nm.

The observation of holes underneath the layers in the substrate (Fig. 4.18 (c), yellow circle) reveals a second possible origin of the liquid Si phase – Si may have diffused through the layer from the substrate. This explanation is supported by the fact that $Si_{0.50}C_{0.50}$ layers without Si excess also exhibit Si droplets on the surface as shown in Fig. 4.18 (c). To explain the uniform distribution of the numerous Si droplets in terms of the few holes, either a high mobility of Si on the surface of the film, or rapid diffusion of molten Si from the substrate in the plane of the film must have occurred. Both mechanisms are plausible, and a more detailed analysis is beyond the scope of this work. Since the presence of lumps and the observation of a preferred crystallization direction is evidence for highly mobile Si and hence the formation of a Si liquid phase, and the aim is the solid phase crystallization of Si NC, further investigation of the high energy FLA samples were waived. In the following, only samples with orientation independent GIXRD spectra were considered and a maximal suitable FLA energy of 47 J/cm^2 for $Si_{0.77}C_{0.23}$ and 40 J/cm^2 for $Si_{0.63}C_{0.37}$ was established.

4.4.2 Formation of nanocrystals by flash lamp anneal

The nanostructure of samples annealed by FLA with settings suitable for solid phase crystallization was studied by **GIXRD**. As mentioned before, the FLA process is characterized by the flash energy and not by the sample temperature. To compare the results from FLA with the RTA processed samples, GIXRD results from FLA were plotted in Fig. 4.19 in line and in the same color as the RTA spectra from Fig. 4.1 (d) and (e) they most resemble.

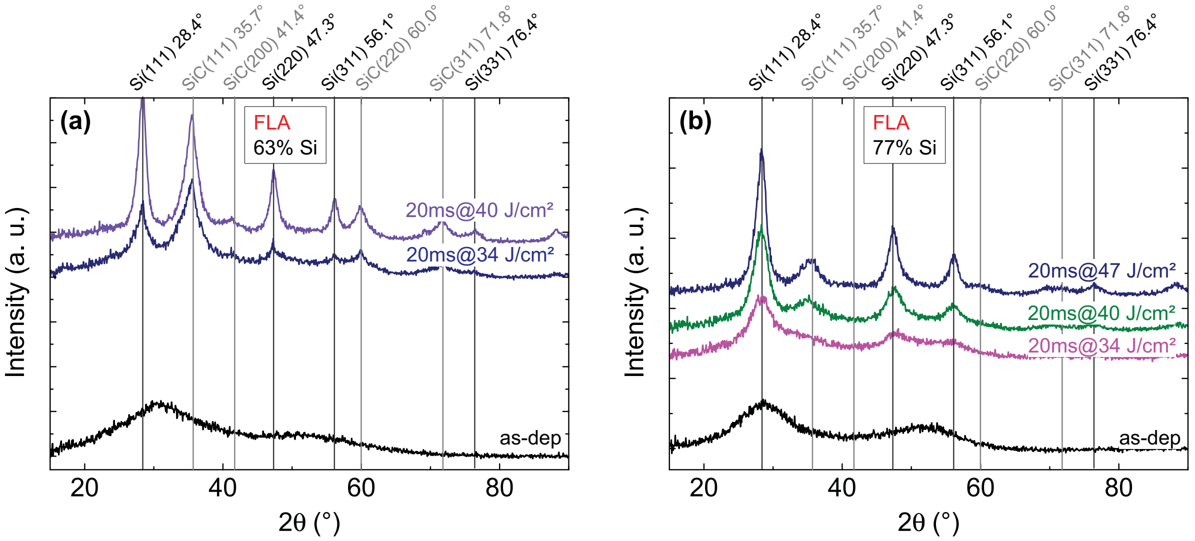

Figure 4.19: GIXRD patterns of FLA samples with a Si content of 63% (a) and 77% (b). To compare flash energies and annealing temperatures, the GIXRD patterns of FLA samples were plotted in line and in the same color with GIXRD patterns of RTA samples with a similar shape in Fig. 4.1.

All FLA samples were subjected to a preanneal step for H effusion of either 2min@800°C (63% Si content, Fig. 4.19 (a)) or 4min@700°C (77% Si content, Fig. 4.19 (b)) before FLA.

The choice of these preanneal temperatures takes into account the dependency of H effusion temperature on the Si content observed in Sec. 4.1.2. In the case of 63% Si content, the highest RTA temperature of 1100°C yields similar data as the lowest FLA energy of 34 J/cm^2. This is different for 77% Si content where a flash energy of 34 J/cm^2 leads to a similar GIXRD pattern as RTA at 900°C. The data from $Si_{0.77}C_{0.23}$ samples exposed to FLA at 40 and 47 J/cm^2 can be compared to that from films that underwent RTA at 1000 and 1100°C, respectively. The average grain sizes of Si and SiC NC are calculated from the GIXRD spectra and plotted as a function of the RTA temperature and the FLA energy in Fig. 4.20.

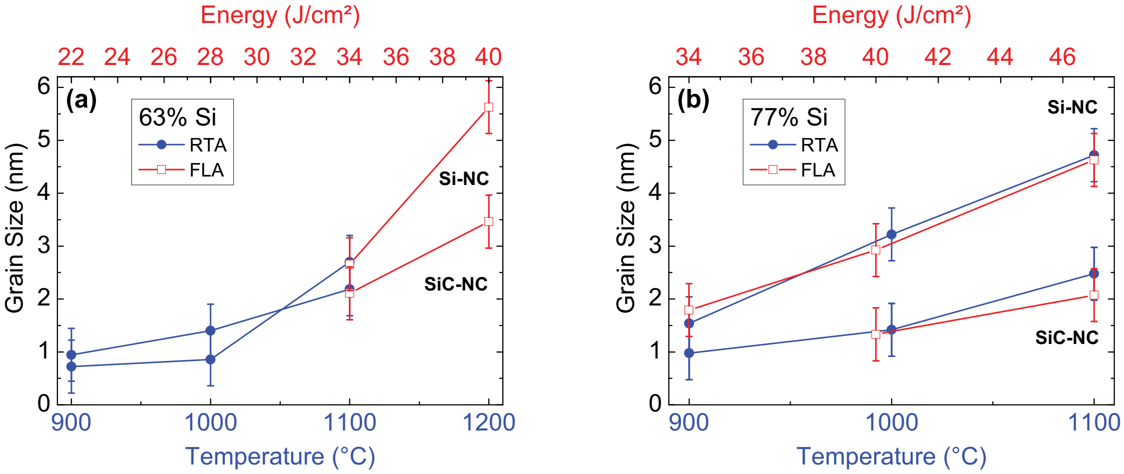

Figure 4.20: Grain sizes calculated from the GIXRD patterns in Fig. 4.19 for $Si_{0.63}C_{0.37}$ (a) and $Si_{0.77}C_{0.23}$ (b). The correspondence between RTA temperatures and FLA energies is the same as between Fig. 4.19 and Fig. 4.1 (d) and (e). Si NC size is seen to be a function of both Si content and annealing temperature while SiC NC size is independent of film composition and only depends on annealing temperature and the corresponding flash energy.

The attribution of the flash energies to a certain RTA temperature corresponds to the attribution of spectra from Fig. 4.19 to Fig. 4.1 (d) and (e). The results confirm what was already assumed from the appearance of the GIXRD spectra: In the $Si_{0.63}C_{0.37}$ samples (Fig. 4.20 (a)) the hottest RTA temperature of 1100°C leads to the same NC sizes (around 2.2 and 2.6 nm for SiC and Si NC respectively) as the FLA with the lowest energy of 34 J/cm^2. For higher flash energies, the grains keep growing up to (3.5 ± 0.5) nm in diameter for SiC NC and (5.6 ± 0.5) nm for Si NC. The grain sizes in the $Si_{0.77}C_{0.23}$ samples (Fig. 4.20 (b)) confirm that the flash with 34 J/cm^2 leads to NC comparable to an RTA at 900°C and the increase to 47 J/cm^2 corresponds to an increase in temperature up to 1100°C. The results also confirm findings from the previous experiments, which showed that the Si NC size is a function of the Si content in the samples. Whereas the SiC NC size only depends on the annealing temperature. The FLA energy, which evokes the same Si NC sizes as RTA at a certain temperature, is greater for higher Si content. For example in Fig. 4.19 and Fig. 4.20, 34 J/cm^2 causes bigger NC in $Si_{0.63}C_{0.37}$ than in

$Si_{0.77}C_{0.23}$, which means that the crystallization process during FLA is favored in films with less Si. This is counterintuitive as Si crystallization would be expected to be easier if more Si is present. The same trend is observed for FLA at higher energies and will be discussed in more detail in Sec. 4.4.3.

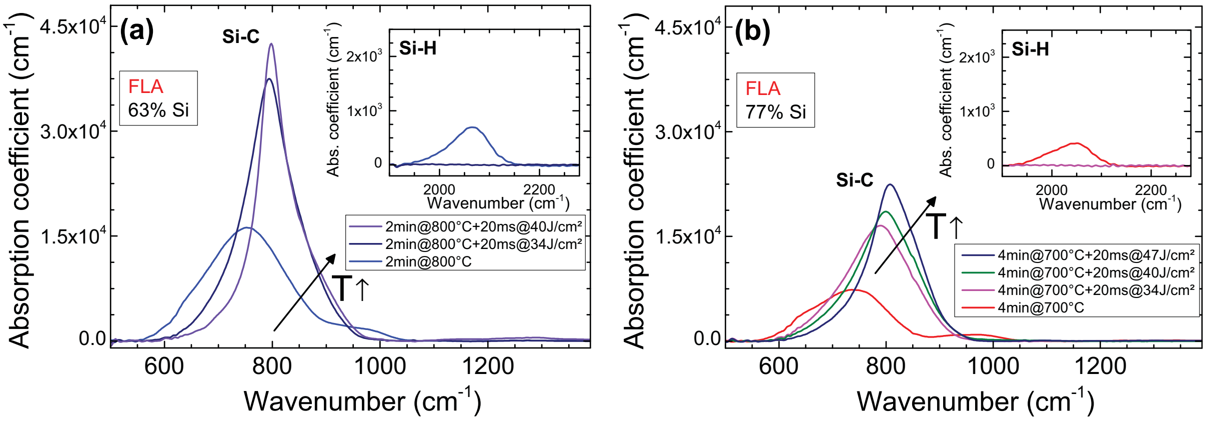

Figure 4.21: FTIR spectra of FLA samples with a Si content of 63% (a) 77% (b). While the Si-C mode increases with temperature und flash energy, the Si-H vibration mode depicted in the insets decreases.

In Fig. 4.21 the **FTIR** spectra of $Si_{0.63}C_{0.37}$ (a) and $Si_{0.77}C_{0.23}$ (b) samples treated by FLA are shown. The spectra are plotted in the same color as the FTIR spectra of RTA samples in Fig. 4.3 they resemble to. The dominant Si-C stretching vibration around 800 cm^{-1} is depicted in the main panels whereas the insets show the Si-H stretching vibration at approximately 2000 cm^{-1}. It is important to note that neither for RTA nor for FLA the formation of Si-O bonds can be observed as no peak around 1000 cm^{-1} appears at higher temperatures. The area of the Si-C mode increases and the peaks shift to higher wavenumbers as the flash energies increase. The latter indicates the SiC crystallization process, whereas the former corresponds to a growing Si-C bond density in the samples. The insets of Fig. 4.21 (a) and (b) show that the area of the Si-H mode is larger for $Si_{0.63}C_{0.37}$ preannealed at 800°C than for $Si_{0.77}C_{0.23}$ preannealed at 700°C. This indicates a dependency of T_{out} on the Si content as already observed for RTA and FA samples in Sec. 4.1.2 and will be explained in Sec. 4.5.

Whereas the overall trends in FTIR spectra of FLA and RTA samples are similar, a careful analysis (described in section 3.2.2) of the SiC crystallization in $Si_{0.77}C_{0.23}$ samples reveals a slight difference. In Fig. 4.22, results from the peak position method are plotted. These trends were confirmed by the results of the fitting method (not shown here). For Si grain sizes larger than 2 nm (as determined by GIXRD), one can observe a significantly lower SiC crystallinity in FLA samples compared to RTA samples for a given Si grain size. The difference in SiC crystallinity increases with increasing Si NC size. This trend will be discussed in the next section.

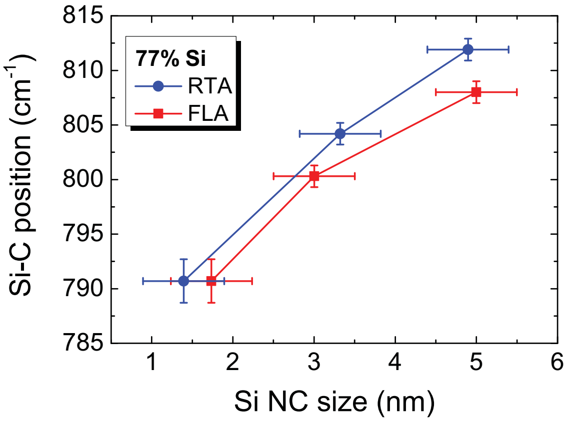

Figure 4.22: The Si-C peak position determined from FTIR spectra as a function of the Si NC size derived from GIXRD patterns show that FLA leads to less SiC crystallinity than RTA for a given Si NC size.

4.4.3 Discussion of flash lamp anneal

Reduced SiC crystallinity in FLA samples: Fig. 4.22 shows a decreasing SiC crystallinity in FLA samples compared to RTA samples for the same Si NC size. This is a remarkable result since the reduction of SiC crystallinity promises defect reduction in the samples [50]. As Fig. 4.20 (b) shows that the SiC NC sizes are the same within the experimental error for a given Si NC size, irrespective of whether FLA or RTA was used, the reduced SiC crystallinity for FLA must result from a lower number of SiC NC in FLA compared to RTA. This can be explained with the help of classical crystallization theory in terms of nucleation and crystal growth. Theory states that the temperature at which maximal nucleation takes place is lower than the temperature of maximum crystal growth (see Fig. 1.3). Near the phase transition temperature, which is the melting point for Si ($T_{\mathrm{S}}^{\mathrm{Si}} = 1414°\mathrm{C}$ [65]) and the decomposition point for SiC ($T_{\mathrm{S}}^{\mathrm{SiC}} > 2500°$), there is rapid crystal growth but a marginal nucleation rate. The RTA samples in Fig. 4.22 were annealed between 900°C and 1100°C and the FLA samples were exposed to comparable annealing conditions as the consistency of the structural measurements in Fig. 4.19/Fig. 4.1 and Fig. 4.21/Fig. 4.3 demonstrate. This means that in RTA and FLA the annealing temperatures were far below the decomposition point of SiC ($T \ll T_{\mathrm{S}}^{\mathrm{SiC}}$). So both nucleation and growth of SiC NC occur throughout the RTA and FLA processes. The larger number of SiC NC in RTA samples may therefore be due to a longer plateau time or a longer heating ramp. The plateau time is 20 ms for FLA and 120 s for RTA. The ramp-up time is 22 s for RTA at 1100°C. In the case of FLA, the heating-up of the samples is only limited by the thermal properties of the layer. The thermal diffusion length L_{D} is the penetration depth of heat into a material with thermal diffusivity ζ and pulse duration t:

$$L_\mathrm{D} = \sqrt{\zeta t}. \tag{4.5}$$

The thermal diffusivity is given by

$$\zeta = \frac{k}{\delta \cdot c_\mathrm{p}}, \tag{4.6}$$

where the other parameters are the thermal conductivity k, the density of the material δ and the specific heat capacity c_p. For the $\mathrm{Si}_x\mathrm{C}_{1\text{-}x}$ layers, these values are not known. However, one can estimate ζ with the help of values for a-Si and SiC from literature summarized in Tab. 2 in App. 8. For a-SiC:H there is no complete dataset available but a lower boundary on its thermal diffusivity $\zeta_\mathrm{SiC}^\mathrm{min}$, can be estimated with the values in Tab. 2 marked with a *, which are $k^* = 0.18\,\mathrm{W/cm{\cdot}K}$ [75], $c_\mathrm{p}^* = 1.2\,\mathrm{J/g{\cdot}K}$ [75], and $\delta^* = 3.217\,\mathrm{g/cm^3}$ [146]. The resulting $\zeta_\mathrm{SiC}^\mathrm{min}$ of $0.0047\,\mathrm{cm^2/s}$ is higher than $\zeta_\text{a-Si}^{1000^\circ\mathrm{C}} = 0.0045\,\mathrm{cm^2/s}$. Therefore, one can use $\zeta_\text{a-Si}^{1000^\circ\mathrm{C}}$ for a lower limit of the thermal diffusivity in the $\mathrm{Si}_x\mathrm{C}_{1\text{-}x}$ layers. This means the heating-up time in FLA is less than 0.1 ms and therefore five orders of magnitude shorter than in the case of RTA. Consequently, the FLA process leads to the formation of less SiC grains during ramping-up and during the temperature plateau compared to RTA.

Influence of Si-content on crystallization behavior: As shown in Fig. 4.17 and Fig. 4.20, a certain FLA energy leads to the formation of bigger Si and SiC NC in $\mathrm{Si}_{0.63}\mathrm{C}_{0.37}$ than in $\mathrm{Si}_{0.77}\mathrm{C}_{0.23}$ layers. Possible explanations are (i) better optical absorption in the $\mathrm{Si}_{0.63}\mathrm{C}_{0.37}$ than in the $\mathrm{Si}_{0.77}\mathrm{C}_{0.23}$ layers (although this would be counterintuitive), (ii) a strong influence of the preanneal step, which was 2min@800°C for $\mathrm{Si}_{0.63}\mathrm{C}_{0.37}$ and 4min@700°C $\mathrm{Si}_{0.77}\mathrm{C}_{0.23}$ samples, and (iii) the influence of the amount of H remaining after the preanneal step, which depends on the Si content. Each possibility will now be examined in turn:

(i) This was checked by modelling the absorptance of the layers $A_{\mathrm{L}\text{-}i}(\lambda) = 1 - R_i(\lambda) - T_i(\lambda)$ $(i = 63, 77)$ from the reflectance $R_i(\lambda)$ and the transmittance $T_i(\lambda)$ for a-$\mathrm{Si}_{0.63}\mathrm{C}_{0.37}$:H and a-$\mathrm{Si}_{0.77}\mathrm{C}_{0.23}$:H layers. The dielectric function $\epsilon_i(\lambda)$ was obtained by fitting ellipsometry data from an a-$\mathrm{Si}_{0.63}\mathrm{C}_{0.37}$:H and an a-$\mathrm{Si}_{0.77}\mathrm{C}_{0.23}$:H film on Si substrate by a Gauss oscillator model using the WVASE® software. These dielectric functions and samples thicknesses from SEM cross sections were then used to simulate $R_i(\lambda)$, $T_i(\lambda)$ and $A_{\mathrm{L}\text{-}i}(\lambda)$ with the help of the software CODE. This ellipsometry model will be presented in detail in the upcoming master thesis of J. Hofmann, supervised in the framework of this Ph.D. thesis, which was still ongoing work at the time when this Ph.D. thesis was submitted.

In Fig. 4.23 (a), the calculated $A_{\mathrm{L}\text{-}i}(\lambda)$ for a-$\mathrm{Si}_{0.63}\mathrm{C}_{0.37}$:H (blue) and a-$\mathrm{Si}_{0.77}\mathrm{C}_{0.23}$:H (green) (left-hand ordinate) are depicted with the normalized intensity of the FLA Xe lamps $I(\lambda)$ [103] (right-hand ordinate). In Fig. 4.23 (b), the calculated $T_i(\lambda)$ for a-$\mathrm{Si}_{0.63}\mathrm{C}_{0.37}$:H (blue) and a-$Si_{0.77}C_{0.23}$:H (green) (left-hand ordinate) are depicted, which correspond to the absorptance in the Si substrate $A_{\text{S-}i}(\lambda)$ under the a-$Si_{0.63}C_{0.37}$:H and the a-$Si_{0.77}C_{0.23}$:H layer ($T_i(\lambda) = A_{\text{S-}i}(\lambda)$).

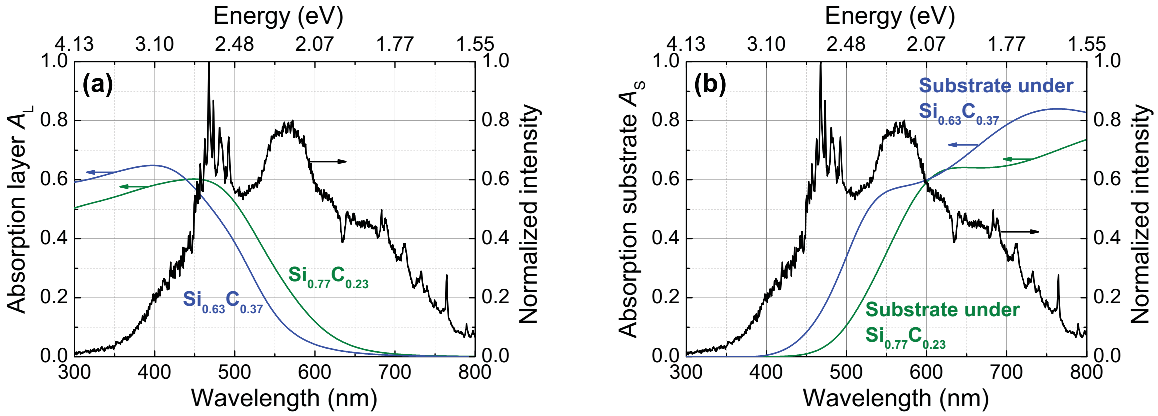

Figure 4.23: The normalized emission spectrum of the Xe lamps (black) used for FLA is plotted with the absorption of the layers $Si_{0.77}C_{0.23}$ ($A_{\text{L-77}}$, green) and $Si_{0.63}C_{0.37}$ ($A_{\text{L-63}}$, blue) in (a) and the absorption of the substrate under the $Si_{0.77}C_{0.23}$ ($A_{\text{S-77}}$, green) and $Si_{0.63}C_{0.37}$ ($A_{\text{S-63}}$, blue) layer in (b).

Fig. 4.23 (a) shows that $A_{\text{L-77}}(\lambda) > A_{\text{L-63}}(\lambda)$ in the spectral range of high intensity of the Xe lamps. Correspondingly, more light is transmitted and therefore absorbed in the Si substrate in the case of the a-$Si_{0.63}C_{0.37}$:H sample ($A_{\text{S-63}}(\lambda) > A_{\text{S-77}}(\lambda)$). To quantify this observation, the fraction of $I(\lambda)$ absorbed in the layer was calculated by:

$$\Gamma_{\text{L-}i} = \frac{\int A_{\text{L-}i}(\lambda) I(\lambda) d\lambda}{\int I(\lambda) d\lambda} \tag{4.7}$$

and in the substrate by:

$$\Gamma_{\text{S-}i} = \frac{\int A_{\text{S-}i}(\lambda) I(\lambda) d\lambda}{\int I(\lambda) d\lambda} \tag{4.8}$$

to be $\Gamma_{\text{L-63}} = 21\%$ and $\Gamma_{\text{L-63}} = 27\%$ in the layers and $\Gamma_{\text{S-63}} = 49\%$ and $\Gamma_{S-77} = 39\%$ in the substrate. It follows that the absorption behavior of the layers alone cannot be the reason for the stronger crystallization in $Si_{0.63}C_{0.37}$:H compared to a-$Si_{0.77}C_{0.23}$:H. However, the overall absorption $\Gamma_i = \Gamma_{\text{L-}i} + \Gamma_{\text{S-}i}$ is higher in the $Si_{0.63}C_{0.37}$:H sample ($\Gamma_{63} = 70\%$) than in the a-$Si_{0.77}C_{0.23}$:H sample ($\Gamma_{77} = 66\%$). Therefore, it is possible that the absorption in the substrate can act as a significant heat source for the layer on top. To verify this, a further experiment was performed with the same a-$Si_{0.63}C_{0.37}$:H and a-$Si_{0.77}C_{0.23}$:H layers deposited on quartz instead of Si substrate because quartz has negligible absorption in the optical wavelength range. After a preanneal of 2min@800°C for $Si_{0.63}C_{0.37}$:H and 4min@700°C for a-$Si_{0.77}C_{0.23}$:H, a FLA of 20ms@47 J/cm^2 was performed for both samples. The Si NC size derived from GIXRD measurements was (14.6 ± 0.5) nm for $Si_{0.63}C_{0.37}$, and (18.6 ± 0.5) nm and thus significantly higher for $Si_{0.77}C_{0.23}$. This result corresponds

to the expectation of higher Si NC size with higher Si content and suggests that strong absorption in the Si substrate promotes film crystallization.
(ii) As $Si_{0.63}C_{0.37}$ was preannealed at higher temperatures than $Si_{0.77}C_{0.23}$, the formation of more crystallization seeds during preannealing in $Si_{0.63}C_{0.37}$ samples compared to $Si_{0.77}C_{0.23}$ could be the result. However, even if this was the case, it would only lead to an increased number of Si and SiC crystallites in $Si_{0.63}C_{0.37}$ samples compared to $Si_{0.77}C_{0.23}$ samples, as discussed in the previous section. But this could not explain the observed difference in NC sizes. Thus, the preanneal temperature is not the reason for the crystallization behavior.
(iii) As shown in the insets of Fig. 4.21, the Si-H vibrational mode of $Si_{0.63}C_{0.37}$ (blue) after preannealing is stronger than in $Si_{0.77}C_{0.23}$ (red), indicating more remaining hydrogen in $Si_{0.63}C_{0.37}$ samples after preannealing than in $Si_{0.77}C_{0.23}$. This higher amount of hydrogen could result in enhanced Si diffusion in $Si_{0.63}C_{0.37}$ compared to $Si_{0.77}C_{0.23}$, leading to the formation of bigger clusters at the same flash energy and therefore to bigger Si NC in $Si_{0.63}C_{0.37}$ samples. Lanckmans *et al.* [147] observed a similar influence of H on the mobility of Cu^+ in PECVD deposited a-SiC:H layers. Both increased hydrogen content after preannealing and substrate absorption of FLA light are probable explanations for the unexpected improvement in Si crystallization with decreased Si content.

4.5 Discussion of the crystallization process

In this section, the most important results of the crystallization process of a-$Si_xC_{1\text{-}x}$:H samples will be recapitulated and discussed.

4.5.1 Role of hydrogen

At low annealing temperatures (400°C...1000°C), H effusion takes place in the samples. H effusion is investigated with the help of the Si-H peak in FTIR spectra. The temperature at which no Si-H peak is observable any more was defined as the temperature of complete H effusion T_{out}. It turned out that T_{out} is a function of the Si content in the layers. This can be explained by the differences in back bonding. With increasing Si content, the C atoms in the vicinity of the Si-H_n bonds are exchanged by Si atoms. Since Si atoms show a lower electronegativity than C atoms, the H atoms are less strongly bonded with increasing Si content and can effuse at lower temperatures [144, 145]. This explanation is supported by the fact that the Si-H_n mode in as-dep samples shifts to lower wavenumbers with increasing Si content. As discussed in section 3.2.1, a shift to lower wavenumbers corresponds to a weakening of the corresponding bond. T_{out} decreases from 1000°C for

$Si_{0.50}C_{0.50}$ over 900°C for $Si_{0.63}C_{0.37}$ down to 800°C for $Si_{0.77}C_{0.23}$. Furthermore, the Si-H peak position shifts to lower wavenumbers with increasing Si content. One can explain these results with a weakening of the Si-H bond with increasing Si content in the layers. For FA, RTA and ZMR annealing, the heating-up time is long enough to allow a smooth H effusion without an extra preanneal step. However, for FLA, a preanneal step for H effusion is inevitable because the heating-up process lasts less than a ms. Otherwise the H effuses explosively at high temperatures and leads to blistering of the $Si_xC_{1\text{-}x}$ layers.

For all samples, the onset of crystallization takes place at temperatures higher than T_{out}. Obviously the breaking of Si-H and C-H bonds favors the formation of Si-Si and Si-C bonds. However, one cannot conclude from this result that H effusion is a indispensable condition for $Si_xC_{1\text{-}x}$ crystallization. Some FLA results even suggest that the presence of a small amount of hydrogen enhances the mobility of Si and C atoms and therefore favors crystallization. It was not possible within the framework of this work to clarify completely the role of H for the crystallization process. However, it was shown how H effusion can be investigated and how the H effusion must be taken into account for a successful sample preparation to avoid layer blistering or cracking.

4.5.2 Crystallization temperature

As mentioned in the Sec. 1.3.2, the onset of Si and SiC crystallization is a very important issue for experimental investigation because from theory one can find arguments for both a Si crystallization temperature ($T_{\mathrm{cry}}^{\mathrm{Si}}$), which is lower than the SiC crystallization temperature ($T_{\mathrm{cry}}^{\mathrm{SiC}}$) or the other way round. One has to point out that the determination of T_{cry} is not straightforward. It was determined that the most precise analysis for $T_{\mathrm{cry}}^{\mathrm{SiC}}$ is the evaluation of the peak shift of the Si-C vibration mode in FTIR spectra. For RTA, $T_{\mathrm{cry}}^{\mathrm{SiC}}$ was estimated to be between 900°C and 1000°C for $Si_{0.50}C_{0.50}$, around 900°C for $Si_{0.63}C_{0.37}$ and between 800°C and 900°C for $Si_{0.77}C_{0.23}$. $T_{\mathrm{cry}}^{\mathrm{Si}}$ cannot be determined as precisely as $T_{\mathrm{cry}}^{\mathrm{SiC}}$ because it can be defined as the temperature where either the Si(111) peak in GIXRD patterns start to grow or the c-Si TO mode in Raman spectra appears. Both events are not only connected to the onset of Si crystallization but also to the amount of c-Si phase in the samples. From GIXRD, $T_{\mathrm{cry}}^{\mathrm{Si}}$ was estimated to be 900°C for both $Si_{0.63}C_{0.37}$ and $Si_{0.77}C_{0.23}$ samples. The analyzis of the corresponding Raman spectra suggest a $T_{\mathrm{cry}}^{\mathrm{Si}}$ of 800°C for $Si_{0.77}C_{0.23}$ and 900°C for $Si_{0.63}C_{0.37}$ samples, although the spectra show no obvious c-Si peak at this temperatures. Despite the small amount of data for $T_{\mathrm{cry}}^{\mathrm{Si}}$, a decrease of $T_{\mathrm{cry}}^{\mathrm{Si}}$ and $T_{\mathrm{cry}}^{\mathrm{SiC}}$ with increasing Si content in the samples is suggested. In the case of Si crystallization, this is supported by the estimation of the effective activation energy Q^{Si} (Sec. 4.2), which is lower in $Si_{0.77}C_{0.23}$ than in $Si_{0.63}C_{0.37}$ samples. For Q^{SiC}, no clear conclusion can be drawn from the data. Is is described in the theory chapter that the nucleation rate is a function of the undercooling ΔT. It's maximum shifts towards the melting point when the diffusion in the melt decreases. This is the reason for the observed dependency of $T_{\text{cry}}^{\text{Si}}$ and probably also of $T_{\text{cry}}^{\text{SiC}}$ on the Si content. With increasing Si content in the layers, the diffusion velocity increases and therefore Q decreases, so does $T_{\text{cry}}^{\text{Si}}$ and $T_{\text{cry}}^{\text{SiC}}$.

Note that for all samples, $T_{\text{cry}}^{\text{Si}}$ and $T_{\text{cry}}^{\text{SiC}}$ lie very close together. As do the estimated $Q^{\text{Si/SiC}}$. This confirms the results observed by all groups working with $\text{Si}_x\text{C}_{1\text{-}x}$ samples, reporting co-crystallization of Si and SiC NC for a wide parameter range. It leads us to the assumption that the crystallization process is barely influenced from the properties of the Si and SiC single systems, but from the overall properties of the $\text{Si}_x\text{C}_{1\text{-}x}$ samples, which depend primarily on x. Another effect, which could assist the Si/SiC co-crystallization is the following: The homogeneous crystallization of one phase could give rise to heterogeneous nucleation of the other phase. As heterogeneous nucleation reduces the activation energy of nucleation, this process could support the Si/SiC co-crystallization even if $T_{\text{cry}}^{\text{Si}}$ and $T_{\text{cry}}^{\text{SiC}}$ for homogeneous nucleation were different. If this process takes place in the sub-nanometer range, it cannot be investigated if the Si or the SiC phase crystallizes first.

4.5.3 Nanocrystal growth

The estimation of the Si and SiC NC mean size was derived from GIXRD patterns. Comparing Si and SiC NC sizes in $\text{Si}_{0.77}\text{C}_{0.23}$ samples treated by FA, RTA and ZMR at 900, 1000 and 1100°C, one can see that at 900 and 1000°C, RTA and ZMR treated samples contain smaller Si and SiC NC than FA samples. At 1100°C, the Si and SiC NC reach the same NC sizes for all three annealing methods. This is an effect of the characteristic of the crystal growth rate described in Sec. 1.3 and verified experimentally in Sec. 4.2. The growth rate increases with decreasing ΔT, which means increasing T. Below 1100°C, the growth rate is low and therefore, smaller NC sizes were reached during the short RTA and ZMR annealing times (2 min). However, at 1100°C the growth rate is high and therefore nearly the same NC size is reached by all annealing methods.

Even though it is not possible to determine the NC size distribution from GIXRD patterns, one can assume that two identical patterns result from two identical size distributions. With that, it was possible to reach a very similar NC size distributions by long-term low temperature and short-term high temperature anneals. From crystallization theory, we would expect smaller NC in the former and larger NC in the latter case (cf. Sec. 1.3.2). This shows that nucleation probably takes place at low temperatures during heating-up. Once the nuclei are formed, NC growth is energetically favored to further nucleation.

In fact, Spinella *et al.* reported increasing growth rates for increasing Si NC sizes [88]. This justifies the assumption of deriving an effective activation energy Q from isothermal annealing curves, taking the Si NC size as a quantity for the crystallized volume. Thereby it was found that $Q_{77}^{\mathrm{Si}} < Q_{63}^{\mathrm{Si}}$, meaning that Si diffusion is higher in $\mathrm{Si_{0.77}C_{0.23}}$ samples compared to $\mathrm{Si_{0.63}C_{0.37}}$ samples. This was explained with the increasing n-doped character of the samples with increasing Si content, leading – according to literature [142] – to an increasing influence of Si diffusion via vacancies. Another explanation for $Q_{77}^{\mathrm{Si}} < Q_{63}^{\mathrm{Si}}$ could be the simple consideration that the distance, which a Si atom must cover to reach the next Si atom decreases with increasing Si content. This could result in a decreasing effective activation energy with increasing Si content. Both explanations can explain the strong dependence between the Si NC size and the Si content in the layers, observed in most of the discussed experiments. Due to $Q_{77}^{\mathrm{Si}} < Q_{63}^{\mathrm{Si}}$, Si NC reach a larger size for the same thermal budget in $\mathrm{Si_{0.77}C_{0.23}}$ samples compared to $\mathrm{Si_{0.63}C_{0.37}}$ samples. It remains unclear why the effect of activation energy is not the same for the SiC NC size, which seems to be largely unaffected from x. Probably Q^{SiC} is determined primarily by the C diffusion coefficient, which is less influenced by the overall Si content because C diffusion occurs always via vacancies and interstitials [142].

The nucleation at low temperatures during ramping-up is the reason why the control of SiC or Si nucleation is so difficult in our samples. Only for high annealing temperatures ($\geq$ 1200°C) and high heating rates (ZMR), a decrease in Si and SiC NC size and crystallinity occurred if no preannel step was conducted. The latter result confirms the expectation from crystallization theory: Significant crystal growth can only occur after a preceding nucleation step.

When all a-Si and a-SiC is transformed into c-Si and c-SiC, the NC continue changing their size due to Ostwald ripening. With the help of SiC and Si crystallinity, the onset of Ostwald ripening can be estimated as discussed in the Si crystallinity paragraph. From 1300°C on, not only 3C-SiC but also 4H-SiC can be detected by GIXRD measurements. For temperatures above 1300°C or high energy flashes, the SiC NC size continues growing. The c-Si phase in the samples either reduces or starts melting above 1300°C. In the former case, reduction of Si NC growth can be observed. Whereas in the latter case, orientation of Si NC and further growth takes place.

4.5.4 SiC crystallinity

Best performance of Si NC devices are expected for samples with low SiC crystallinity. The evaluation of SiC crystallinity was done qualitatively by investigating the position of the Si-C vibration mode and quantitatively by a peak fitting of this mode with one

Lorentzian and two Gaussian peaks. It turned out that the fitting error gives rise to an uncertainty of about 20% on absolute SiC crystallinity values from samples with different Si content. Therefore, one cannot rule out a certain dependence of the SiC crystallinity on the Si content. However, one can state that it must be less than 20%, and therefore less significant than the dependence of Si crystallinity on the Si content (see next paragraph). The SiC crystallinity increases with increasing annealing temperature for $Si_{0.50}C_{0.50}$, $Si_{0.63}C_{0.37}$ and $Si_{0.77}C_{0.23}$ samples. No FTIR data exist for high temperatures $\geq 1200°C$. However, the GIXRD results, which show further SiC NC growth accompanied by an increasing amount of c-SiC phase, allow the conclusion of further increase of SiC crystallinity above 1200°C. It can also be concluded from the results that even at high temperatures there is a regime of SiC nucleation. This is not surprising as all the annealing temperatures used in this work are far below the decomposition temperature of SiC and therefore nucleation is expected from crystallization theory. Hence, the suppression of SiC nucleation and crystal growth by choosing a certain annealing temperature is not possible. The only possibility to reduce the SiC crystallinity is a reduction in annealing time. This was observed in the form of a clear dependence of SiC crystallinity on the annealing method. FLA samples with Si NC of a certain size show less crystalline SiC matrix than RTA samples with Si NC of the same size. Probably the SiC matrix is even more crystalline in case of FA samples with the same Si NC size. However, it was not possible to verify this assumption unambiguously.

4.5.5 Si crystallinity

A high Si crystallinity is expected to be energetically advantageous for the samples because c-Si is more stable than a-Si, and because c-Si has a distinct bandgap and no pronounced tail states as a-Si. The determination of Si crystallinity was done qualitatively by GIXRD spectra and quantitatively by Raman spectra. The main source of uncertainty for this evaluation is the fact that Raman measurements are only possible for layers on quartz substrate. Only for FA is it possible to ensure exactly the same annealing process for samples on quartz and for samples on Si substrate.

First of all, all Si crystallinities determined from our samples are far below 100%. This behavior shows that the Si NC are probably covered by an a-Si shell. For all Si rich samples, treated by FA, RTA and ZMR, the Si crystallinity increases with increasing annealing temperatures up to 1200°C. For higher temperatures, only data from ZMR annealed $Si_{0.77}C_{0.23}$ samples exist. They show a saturation of Si crystallinity and simultaneously a further Si NC growth, which was explained by Ostwald ripening and instability of small NC at high temperatures. At 1350°C, a loss of c-Si phase for $Si_{0.63}C_{0.37}$ and $Si_{0.77}C_{0.23}$

samples is observed in GIXRD patterns. This loss at temperatures near the melting point is attributed to an expected aspect of crystallization theory. Near the melting point, ΔT is very low for Si and therefore r^*_{Si} is high. This leads to the dissolving of Si NC with $d_{Si} \leq r^*$, which one would expect to lead to a decrease in Si crystallinity. However, because a simultaneous increase in SiC phase is observed, the formation of further SiC from the new a-Si phase is assumed. The C atoms required for this process could either still be present in the samples or diffuse into the samples from the surface where one always expect a small amount of adsorbed C from the environment.

There are two more aspects from crystallization theory, which were verified experimentally. For Si crystallization near the melting point, no Si nucleation and reduction of Si NC growth rate was expected. However, for the Si$_x$C$_{1\text{-}x}$ samples, Si NC were also observed for temperatures near the melting point, which means that a certain nucleation must have taken place. As there was always either a heating ramp (FA, RTA, ZMR) or a preanneal step for H effusion (FLA), the Si nucleation most likely took place during this period. Therefore the observed c-Si phase after high temperature annealing does not contradict nucleation theory. This was verified by significantly reducing the preanneal time, generating less Si phase, and smaller Si NC. The smaller number of Si NC verifies their preferred formation during preanneal. Their smaller size verifies the reduced Si growth rate near the melting point.

Furthermore, ZMR and RTA data show that the Si crystallinity is a function of the Si content. Namely, Si$_{0.63}$C$_{0.37}$ shows significantly lower Si crystallinity than Si$_{0.77}$C$_{0.23}$ at a certain temperature. This means Si$_{0.63}$C$_{0.37}$ contains a higher percentage of a-Si phase after annealing at 1100°C than Si$_{0.77}$C$_{0.23}$ samples. Analogous to the smaller Si NC size in Si$_{0.63}$C$_{0.37}$ compared to Si$_{0.77}$C$_{0.23}$ samples, this was attributed to be a consequence of $Q^{\mathrm{Si}}_{77} < Q^{\mathrm{Si}}_{63}$. This means that more energy is needed to reach the same degree of Si crystallinity in Si$_{0.63}$C$_{0.37}$ compared to Si$_{0.77}$C$_{0.23}$ samples. Vice versa, the Si crystallinity in Si$_{0.63}$C$_{0.37}$ samples is smaller than in Si$_{0.77}$C$_{0.23}$ samples when the same amount of energy was supplied. This is supported by a publication from Yoshii *et al.* [148], which also suggests an increasing Si diffusion, accompanied with a facilitated Si crystallization for increasing Si content in Si$_x$C$_{1\text{-}x}$ layers.

Chapter 5

Si nanocrystals in multilayers

Si nanocrystal (NC) size control is crucial for successful quantum confinement. Therefore, Si NC size control was tried to achieve by depositing multilayer (ML) with varying sublayer thicknesses and it was found out that strong sublayer intermixing occurs during annealing. Nevertheless, Si NC size control can be achieved by varying the Si content under these conditions. These results were published in the Journal of Applied Surface Science [45]. In the second experiment, it is shown that the incorporation of oxygen into the ML hinders sublayer intermixing and therefore promises a new route for Si NC size control.

5.1 Size control by Si content

The deposited ML consist of 20 bilayers of alternating a-$Si_{0.50}C_{0.50}$:H barrier (SiC) and a-$Si_{0.77}C_{0.23}$:H well (SRC) layers. The thickness of these sublayers was varied between 3 and 9 nm, resulting in total as-dep layer thicknesses of 187...334 nm. Three different types of singlelayers (SL) of approximately 200 nm thickness were deposited: SL with the barrier and the well sublayer composition ($Si_{0.50}C_{0.50}$ and $Si_{0.77}C_{0.23}$), and SL with a composition of $Si_{0.63}C_{0.37}$, which corresponds to the overall Si content of a ML with SRC/SiC sublayer thicknesses of 9/6 nm. It is important to note that during this work, it was not possible to verify the overall Si content in the ML experimentally. Because the ML deposition by PECVD consists of 40 individual layers, it is most likely that the frequent change of gas flow and the deposition conditions at interfaces influence the incorporated amount of Si.

5.1.1 Grazing incidence X-ray diffraction results

The GIXRD patterns of the ML stacks with a thickness variation of SRC and SiC sublayers and an annealing of 1000°C for 60 min were measured and the results of the NC size analysis are presented in Fig. 5.1 (a) and (b). In Fig. 5.1 (a), the thickness of the SiC sublayers is 6 nm for all samples and in Fig. 5.1 (b), the thickness of the SRC sublayers is 6 nm for all samples.

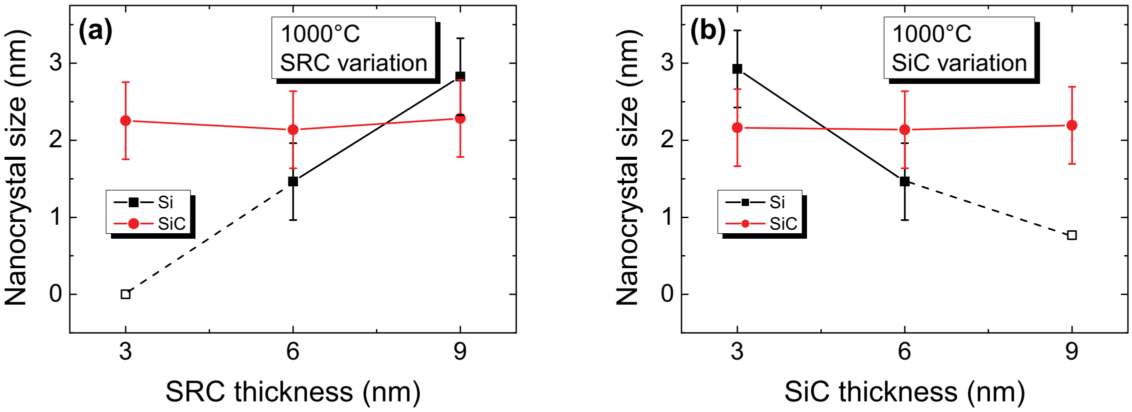

Figure 5.1: The GIXRD patterns of ML stacks with varying SRC sublayer thickness and varying SiC sublayer thickness were used to calculate the mean NC size of Si and SiC NC. The relation between the sublayer thickness and the NC sizes is shown in (a) for SRC thickness variation and constant SiC thickness of 6 nm and in (b) for SiC thickness variation and constant SRC thickness of 6 nm. The open squares indicate samples for which no definite determination of the Si NC size was possible, and the lines are a guide for the eye.

While the SiC NC size is (2.2 ± 0.5) nm for all sublayer thicknesses, the Si NC size ranges between (1.5 ± 0.5) nm and (3.5 ± 0.5) nm. This is the targeted range for Si NC in SiC as Löper *et al.* [27] calculated that Si NC in SiC with a diameter of around 2.5 nm show a band gap of 1.7 eV, corresponding to the ideal band gap of the top cell in an all-Si tandem solar cell [19]. Closer inspection reveals that the Si-NC size increases with increasing SRC sublayer thickness, and decreases with increasing SiC barrier layer thickness.

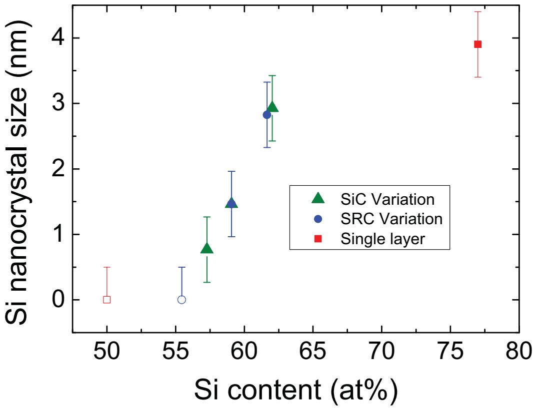

Figure 5.2: The Si NC size as a function of overall Si content in the ML with SRC sublayer thickness variation (blue), SiC barrier thickness variation (green) and two SL (red). In the samples with 50% and 56% Si content, no crystalline Si was detected by GIXRD.

The increase in Si NC size with SRC sublayer thickness (Fig. 5.1 (a)) is expected from the ML approach. However, for a constant SRC layer thickness of 6 nm at varying SiC barrier layer thicknesses, the ML approach predicts a constant Si NC size, which is inconsistent with the trend in Fig. 5.1 (b). A possible explanation for this behavior is a strong intermixing of the SiC and SRC sublayers, leading to a homogenous distribution of the excess Si throughout the sample. In principle, intermixing seems possible because the estimation of a lower limit for the diffusion coefficient of Si in SiC (D_{Si}) during the growth of SiC by carbonization of Si from Cimalla *et al.* [149] leads to values of $1{\cdot}10^{-16}\,\mathrm{cm}^2/\mathrm{s}$ and $2{\cdot}10^{-15}\,\mathrm{cm}^2/\mathrm{s}$ at 1000°C and 1100°C, respectively. These values correspond to a diffusion length of 6 nm after 60 min at 1000°C and 60 nm after 30 min at 1100°C, which would be sufficient for complete intermixing even for a ML with 9 nm barriers. Furthermore, intermixing of SiC/SRC ML was observed by many groups using TEM investigations [33, 42, 43]. The assumption of intermixing was checked experimentally by plotting the Si NC size as a function of the overall Si content in Fig. 5.2. In addition to the ML already investigated in Fig. 5.1, two SL with a composition of $\mathrm{Si}_{0.50}\mathrm{C}_{0.50}$ and $\mathrm{Si}_{0.77}\mathrm{C}_{0.23}$ were also taken into account.

The Si content was calculated by the following routine. First, the non-normalized mass fractions of Si and SiC (M_{Si}, M_{SiC}) in the $\mathrm{Si}_x\mathrm{C}_{1\text{-}x}$ well layers was calculated with the help of the molar masses m_{Si} and m_{SiC}:

$$M_{\mathrm{Si}} = m_{\mathrm{Si}} \cdot (2x-1); \qquad M_{\mathrm{SiC}} = m_{\mathrm{SiC}} \cdot (1-x). \tag{5.1}$$

Then the normalized volume fraction of Si in the $\mathrm{Si}_x\mathrm{C}_{1\text{-}x}$ well layer was calculated with the help of the mass densities of Si and SiC (ρ_{Si}, ρ_{SiC}):

$$V_{\mathrm{Si}} = \frac{M_{\mathrm{Si}}/\rho_{\mathrm{Si}}}{M_{\mathrm{Si}}/\rho_{\mathrm{Si}} + M_{\mathrm{SiC}}/\rho_{\mathrm{SiC}}}. \tag{5.2}$$

With this value, the overall Si and SiC volume fraction in a ML stack ($V_{\mathrm{Si}}(\mathrm{ML})$, $V_{\mathrm{SiC}}(\mathrm{ML})$) with a total well thickness s_{w} and a total barrier thickness s_{b} was calculated:

$$V_{\mathrm{Si}}(\mathrm{ML}) = V_{\mathrm{Si}} \frac{s_{\mathrm{w}}}{s_{\mathrm{w}} + s_{\mathrm{b}}}; \qquad V_{\mathrm{SiC}}(\mathrm{ML}) = 1 - V_{\mathrm{Si}}(\mathrm{ML}). \tag{5.3}$$

To transform the Si volume fraction $V_{\mathrm{Si}}(\mathrm{ML})$ in at%, the number of atoms in a cubic centimetre of Si and SiC (n_{Si}, n_{SiC}) is needed:

$$n_{\mathrm{Si}} = N_{\mathrm{A}} \cdot \frac{\rho_{\mathrm{Si}}}{m_{\mathrm{Si}}} = 4.99 \cdot 10^{22} \frac{\mathrm{at}}{\mathrm{cm}^3} \quad \& \quad n_{\mathrm{SiC}} = 2N_{\mathrm{A}} \cdot \frac{\rho_{\mathrm{SiC}}}{m_{\mathrm{SiC}}} = 9.53 \cdot 10^{22} \frac{\mathrm{at}}{\mathrm{cm}^3}, \tag{5.4}$$

where N_{A} is the Avogadro constant. Weighted with the volume fractions, the numbers of atoms of Si and SiC in the ML ($n_{\mathrm{Si}}(\mathrm{ML})$, $n_{\mathrm{SiC}}(\mathrm{ML})$) were determined as follows:

$$n_{\mathrm{Si}}(\mathrm{ML}) = V_{\mathrm{Si}}(\mathrm{ML}) \cdot n_{\mathrm{Si}}; \qquad n_{\mathrm{SiC}}(\mathrm{ML}) = V_{\mathrm{SiC}}(\mathrm{ML}) \cdot n_{\mathrm{SiC}}. \tag{5.5}$$

This led finally to the overall Si content in the ML (Si(at%)):

$$\mathrm{Si}(at\%) = \frac{n_{\mathrm{Si}}(\mathrm{ML}) + n_{\mathrm{SiC}}(\mathrm{ML})/2}{n_{\mathrm{Si}}(\mathrm{ML}) + n_{\mathrm{SiC}}(\mathrm{ML})}. \tag{5.6}$$

The continuous increase in Si NC size with overall Si content in Fig. 5.2, regardless of the precursor layer structure, supports the assumption of strong sublayer intermixing. Also do SEM cross sections as they show a layered structure for as-dep ML, and a loss of these structure after annealing (cf. Fig. 5.6 in the next paragraph).

5.1.2 Spectrophotometry results

Two bulk SL with the compositions of the sublayers in the ML ($\mathrm{Si}_{0.77}\mathrm{C}_{0.23}$ and $\mathrm{Si}_{0.50}\mathrm{C}_{0.50}$) as upper and lower bound and four ML stacks with varying sublayer thicknesses were used for spectrophotometry measurements. In Fig. 5.3 (a), the absorption coefficient α for these samples is depicted as a function of photon energy E.

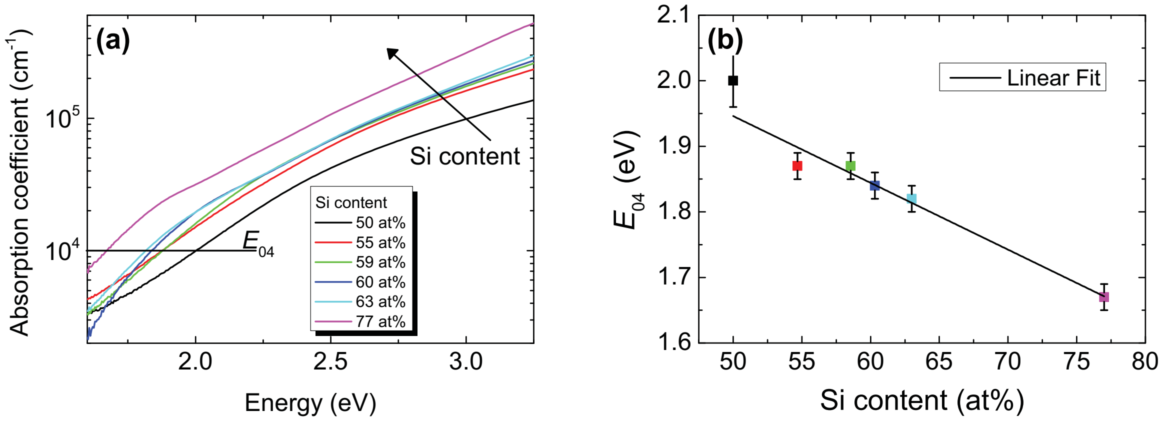

Figure 5.3: In (a), the absorption coefficient α derived from R&T measurements for ML with a different overall Si content is shown. The 50% and the 77% samples are SL. The bandgap estimation E_{04} at $\alpha = 10^4\,\mathrm{cm}^{-1}$ as a function of the Si content is plotted in (b).

Effectively, $\alpha(E)$ of all ML lies between the border cases of bulk SiC and SRC. A reliable determination of the bandgap by evaluating the Tauc plots derived from Fig. 5.3 (a) is not possible as the Tauc plots show no linear region required for determining the bandgap. This result is not surprising given that this evaluation method is valid only for amorphous semiconductors [41, 150]. Thus, the bandgap E_{04} was estimated by taking the energy at $\alpha = 10^4\,\mathrm{cm}^{-1}$. Fig. 5.3 (b) shows that E_{04} decreases continuously with the Si content. This could in principle be attributed to a decreasing bandgap with increasing Si NC size as we know from Fig. 5.2 that the Si content correlates with the Si NC size. However, the decrease in E_{04} can more likely be explained by the intermixing of the ML that leads to a typical absorption behavior of an $\mathrm{Si}_x\mathrm{C}_{1\text{-}x}$ layer with increasing x.

5.1.3 Conclusions Si content

ML stacks consisting of SRC/SiC sublayers were studied with a view to achieving Si NC size control and strong sublayer intermixing was observed even for the thickest barrier layer of 9 nm (as-dep). The Si NC size is a function of the overall Si content in the ML and not only of the SRC well thickness. Also the optical properties can be ascribed to sublayer intermixing as the decreasing trend of E_{04} with increasing Si-content is the typical behavior of a Si_xC_{1-x} layer with increasing x.
Based on these results, the use of SL with varying Si content is proposed to control the Si NC size instead of using ML with varying SRC thicknesses. The examined mean Si NC sizes between 1 nm and 4 nm lie in the targeted range for Si NC in SiC as a top cell absorber in an all-Si tandem solar cell [19]. It is true that in SL, the control of crystal size, size distribution, and interdot distance is limited. However, the formation of large NC ($>$ 10 nm) can be excluded for all samples by means of GIXRD measurements. Furthermore, both the interdot distance and the NC size distribution are less crucial for Si NC in SiC than for Si NC in SiO_2 [23, 27]. Consequently, precise control of Si NC size and separation is not required. Additionally, as this study and other works [29, 33, 42] show that control over both is extremely difficult to obtain with the ML approach in the Si NC/SiC system, it follows that SRC SL might be more effective for optimising the optoelectronic properties of SiC with embedded Si NC for Si NC-based devices. Another approach would be maintaining the ML structure by changing the properties of the as-dep samples as explained in the next section.

5.2 CO_2 in multilayers

In this section, the intentional incorporation of oxygen (O) into the $Si_{0.50}C_{0.50}/Si_{0.77}C_{0.23}$ ML is described. The incorporation of O was realised by adding CO_2 to the precursor gases SiH_4, CH_4 and H_2. To check if the use of CO_2 as precursor gas leads to the desired O incorporation into the samples, $Si_{0.50}C_{0.50}$ and $Si_{0.77}C_{0.23}$ SL were deposited under CO_2 fluxes varying between 0.0 and 10.0 sccm. To compensate a possible increase in C content in the samples due to the CO_2 flux, the CH_4 flux was reduced by the same amount as the CO_2 flux was increased. The FTIR spectra in Fig. 5.4 show that the increase in CO_2 flux from 0.0 to 10.0 sccm leads to an increased vibration mode between 1000 and 1200 cm^{-1}. This result confirms the successful incorporation of O by CO_2 precursor gas as either Si-O or C-O vibrations are expected in this wavelength range [151]. The increase of the vibration for a certain CO_2 flux is stronger in the case of $Si_{0.77}C_{0.23}$ (Fig. 5.4 (b)) than in $Si_{0.50}C_{0.50}$ samples (Fig. 5.4 (a)). Therefore, it is assigned to Si-O vibrations as an increasing Si-O bond density with increasing Si content seems more obvious than an increasing C-O content with increasing Si content.

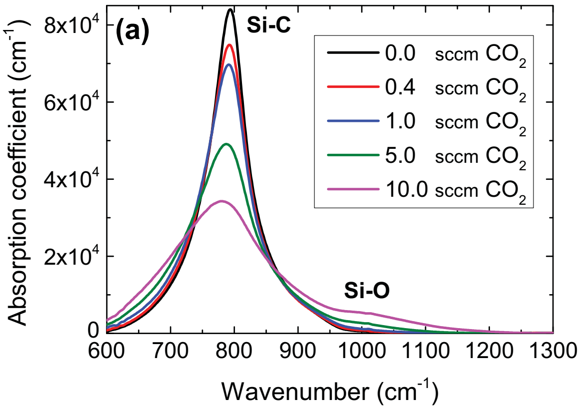

Figure 5.4: FTIR spectra of (a) $Si_{0.50}C_{0.50}$ and (b) $Si_{0.77}C_{0.23}$ samples deposited with increasing amounts of CO_2 among the precursor gases and annealed for 30min@1100°C by FA. The increasing Si-O mode indicates the successful oxygen incorporation.

It is an interesting question if the O in the samples influences the SiC crystallinity. Therefore, it was tried to determine the SiC crystallinity by the two available methods. The fitting of the Si-C vibration described in Sec. 3.2.2 and the shift of the peak position of the SiC vibration mode. Both methods are more difficult to apply for samples with O content compared to samples without O content. The fitting of the Si-C mode is complicated by the overlapping of the Si-O peak. The peak shift of the Si-C mode is more difficult to interpret with varying O content because both a change in sample composition and SiC crystallization are expected to lead to a peak shift. In Fig. 5.5 (a), the evaluation of the $Si_{0.50}C_{0.50}$ FTIR spectra are presented. The results of the fitting method are depicted in red (left-hand ordinate) and the Si-C peak position is depicted in blue (right-hand ordinate).

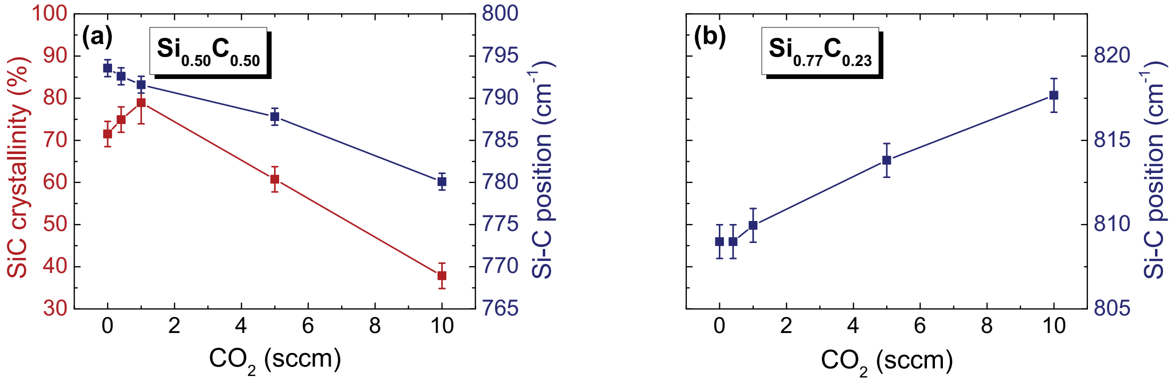

Figure 5.5: SiC crystallinities derived from the FTIR spectra in Fig. 5.4 for $Si_{0.50}C_{0.50}$ samples (a) and $Si_{0.77}C_{0.23}$ samples (b) with increasing oxygen content annealed for 30min@1100°C by FA.

For high CO_2 fluxes, a decrease of SiC crystallinity is observed and confirmed by the shift of the Si-C peak position to lower wavenumbers. For low CO_2 fluxes up to 1 sccm a slight increase of SiC crystallinity was observed but will not be discussed further as the observed change lies within the fitting error. Probably the Si-O clusters in the Si-C network complicate the SiC crystallization in the $Si_{0.50}C_{0.50}$ samples.

In the case of $Si_{0.77}C_{0.23}$ samples (Fig. 5.5 (b)), no reliable fitting of the Si-C mode is possible because the amorphous Si-C mode, the Si-N mode, and the Si-O mode overlap strongly and show strong interdependence. As an influence on the amplitude and the position of the Si-N peak by O incorporation cannot be excluded, no further assumptions can reduce the degrees of freedom of the peak fitting. Therefore, only the SiC peak position is shown in Fig. 5.5 (b). The SiC peak position shifts to higher wavenumbers with higher O content, indicating a strengthening of the Si-C bonds. The strengthening could be explained analogously to the strength of the Si-H bond with increasing Si content in Sec. 4.5. In the vicinity of a Si atom, which is initially bonded to four C atoms when no O is in the network, some of the C atoms will be replaced with O atoms due to the increasing O content. As O has a larger electronegativity than C, the Si atom will be polarized more positively when bonded to an O atom, resulting in a strengthening of the Si-C bond. This effect is probably stronger in $Si_{0.77}C_{0.23}$ layers than in $Si_{0.50}C_{0.50}$ because more O is incorporated in $Si_{0.77}C_{0.23}$ samples. If O influences the SiC crystallinity of $Si_{0.77}C_{0.23}$ samples cannot be determined with the help of the FTIR data. However, one can at least assume that the influence of O incorporation on the SiC crystallinity in $Si_{0.77}C_{0.23}$ samples is not strong as the shape of the FTIR spectra differ only slightly from each other with increasing O content (Fig. 5.4 (b)).

It can be concluded from the SL experiments that O incorporation into the samples by adding CO_2 to the precursor gases was successful. Furthermore, the stoichiometric samples show a decrease of SiC crystallinity with increasing O content. The influence of O on the SiC crystallinity in $Si_{0.77}C_{0.23}$ samples is weak and could not be quantified reliably.

As a second step, the O-containing SL were combined to a $Si_{0.50}C_{0.50}/Si_{0.77}C_{0.23}$ (6 nm/9 nm) ML stack with 20 bilayers. The choice of the sublayer thickness leads to an overall Si content of 63% and allows a direct comparison between ML and $Si_{0.63}C_{0.37}$ SL. Three different types of ML and two different SL for comparison were prepared:

- ML without CO_2 (**ML0**)
- ML with 6.8 sccm CO_2 flux during $Si_{0.77}C_{0.23}$ sublayer deposition (**ML77**)
- ML with 10.0 sccm CO_2 flux during $Si_{0.50}C_{0.50}$ sublayer deposition (**ML50**)
- SL $Si_{0.63}C_{0.37}$ with 4.4 sccm CO_2 (**SL63**)
- SL $Si_{0.77}C_{0.23}$ with 6.8 sccm CO_2 (**SL77**)

As the FTIR spectra show that an increasing amount of O is incorporated into samples with increasing Si content, it was tried to account for this by adapting the CO_2 flux to the

Si content in a way that ML77, ML50 and SL63 have the same overall O content. FTIR spectra (not shown here) indicate that this is only roughly the case. ML50 shows the highest Si-O content, whereas ML77 and SL63 show about 15% and 35% less Si-O bonds, respectively.

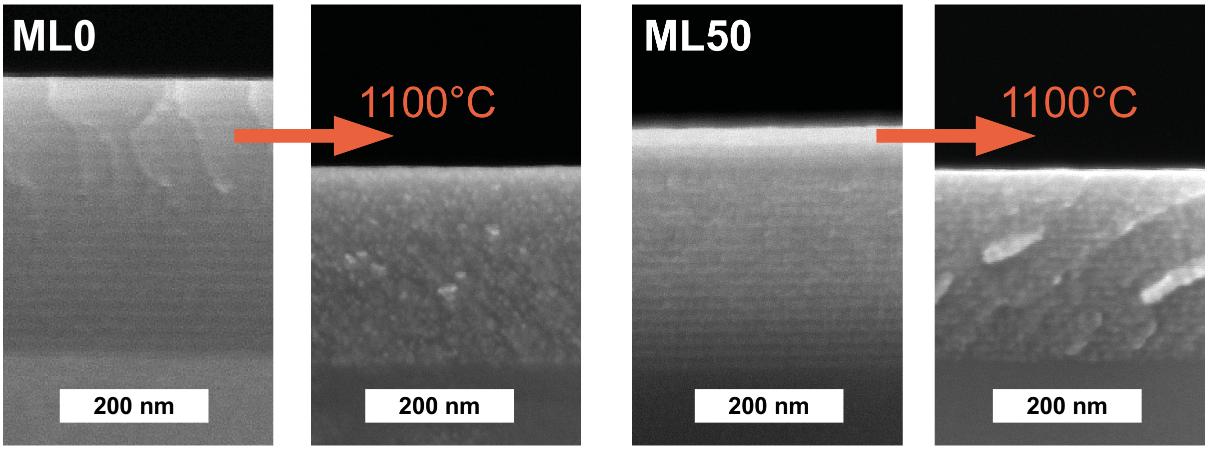

Figure 5.6: SEM cross section images of ML deposited with and without CO_2 as precursor gas before and after annealing for 30min@1100°C by FA.

In Fig. 5.6, SEM cross sections of the ML before and after annealing at 1100°C are shown. The ML with and without CO_2 show a layered structure in the SEM cross section before annealing. After annealing, the ML structure is lost in the ML0 samples as discussed in Sec. 5.1. However, in the case of ML with O, the ML structure is preserved during the annealing process as shown by the example of ML50 in Fig. 5.6. For the first time, a ML structure with a Si content of only 77% in the Si-rich layers survived an annealing step of 30min@1100°C. It is concluded from this result that O in the samples hinders Si or C diffusion and therefore intermixing of the sublayers. FTIR spectra of as-dep $Si_{0.50}C_{0.50}$ and $Si_{0.77}C_{0.23}$ samples show that approximately 60% of the Si-O bonds are already present after deposition. This is only a rough estimation as the Si-O vibration in the as-dep samples overlap strongly with the Si-H vibration. However, the large amount of Si-O bonds present prior to annealing are probably responsible for the reduced Si and C mobility during the annealing step. This interpretation is supported by the Raman and GIXRD results presented in Fig. 5.7 (a) and (b), respectively.

To draw conclusions about the Si crystallinity from the Raman spectra, the fitting method described in Sec. 3.3.3 was not applied because the interesting samples are too similar to obtain reliable values for the Si crystallinity. Only a qualitative comparison between the different Raman spectra is possible. Therefore, all normalized Raman spectra are plotted in Fig. 5.7 (a). The black and the green spectra show SL63 and SL77, respectively. The brown spectrum represents ML0, and the orange and red spectra represent the samples ML77 and ML50. Both ML have an overall Si content of 63%. As reported before (Sec. 4.1.3), the sample with the highest Si content (77%) clearly shows the most pronounced Raman c-Si peak (green spectra) and a c-Si peak position at higher wavenumbers than the other spectra.

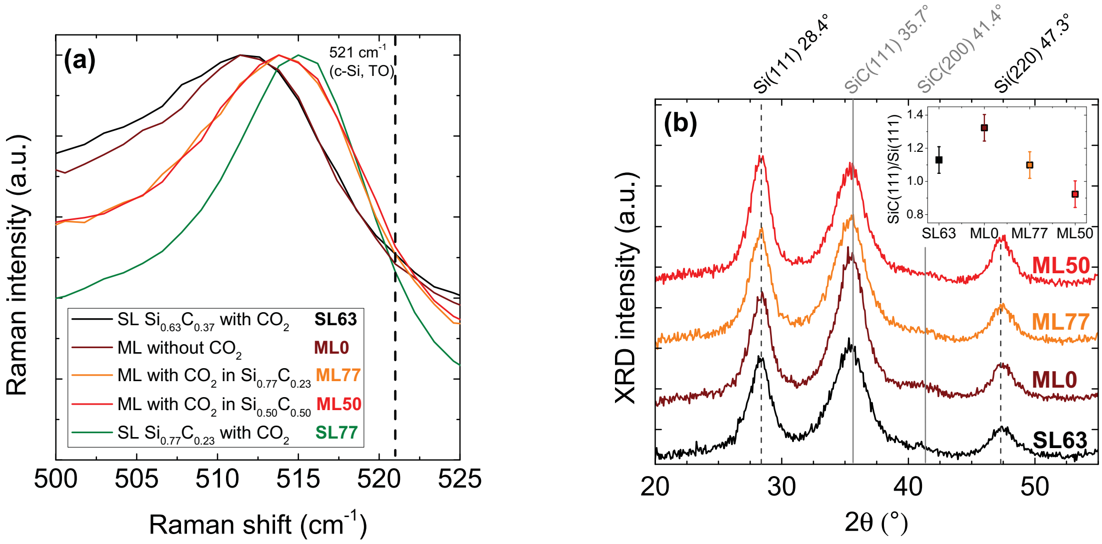

Figure 5.7: Raman spectra (a) and GIXRD patterns (b) of ML with CO_2 (red) and without CO_2 (black) annealed for 30min@1100°C by FA.

This can be explained by a larger fraction of crystalline Si present in the SL77 than in the other samples. Raman results (not shown here) also prove that the Si crystallinity in $Si_{0.77}C_{0.23}$ SL samples is not influenced by the O content in the layers. This is also true for the $Si_{0.63}C_{0.37}$ SL sample with and without CO_2. In Fig. 5.7 (a) the SL63 sample clearly shows a smaller c-Si fraction than the SL77 sample. These results are not surprising so far. However, looking at the ML0 and at ML50/ML77 the issue gets more interesting. The ML0 shows a very similar c-Si peak at exactly the same peak position as the c-Si peak of SL63. This supports the assumption from Fig. 5.6 suggesting strong sublayers intermixing in the ML and therefore a behavior of ML0 after annealing which is quite similar to the properties of SL63 after annealing. Let us finally review the Raman spectra of ML50 (red) and ML77 (orange). The shape of the c-Si Raman modes and the peak positions lie between that of the ML0 and the SL77. This is an indication for a larger c-Si fraction in ML with CO_2 compared to ML without CO_2. A higher c-Si fraction requires a local Si concentration in the samples, which is higher than 63%. This strengthens the initial assumption that the O incorporation into the ML hinders sublayer intermixing.

In Fig. 5.7 (b) the GIXRD pattern for all samples from Fig. 5.7 (a) are depicted, except for SL77. At first sight, all GIXRD pattern look quite similar. The differences of Si and SiC NC size evaluated from the patterns lie within the experimental error. However, the SiC(111)/Si(111) peak intensity ratios show significant differences as depicted in the inset of Fig. 5.7 (b). The increase of SiC(111)/Si(111) for ML0 compared with SL63 could result from a slight difference in overall Si content in these two layers and will not be discussed further. Here the difference of the three ML will be examined. SiC(111)/Si(111) shows its highest value for ML0, decreases for ML77, and decreases further for ML50. This shows that O incorporation improved the c-Si to c-SiC ratio, either by the reduction of SiC crystallinity or by the increase of c-Si phase. It can be concluded that the Si-C bond density decreases starting with ML0 over ML77 down to the lowest value for ML50 from FTIR measurements (not shown here). As mentioned before, no clear statement about the SiC crystallinity is possible.

It seems to play a subordinated role if CO_2 is added to the $Si_{0.77}C_{0.23}$ or to the $Si_{0.50}C_{0.50}$ sublayers in the ML stack. It was just argued that the majority of the Si-O bonds are formed prior to annealing. Perhaps diffusion of the unbound O from the $Si_{0.50}C_{0.50}$ to the $Si_{0.77}C_{0.23}$ layers occurs during annealing. Di Ventra *et al.* [152] calculated that the activation energy for diffusion of a single O atom in 3C-SiC is only 1.7 eV, compared to 2.5 eV in bulk Si. However, it is doubtful if these values apply for $Si_{0.50}C_{0.50}$ compared to $Si_{0.77}C_{0.23}$ layers. The second possible reason is the deposition process itself. The regulation of the CO_2 flux at the PECVD tool is much slower than the regulation of the other precursor gases. As the deposition of a single sublayer takes less than 50 s, it is assumed that there is a certain amount of CO_2 molecules in the plasma during the whole process, leading to an incorporation of O in the whole ML samples.

Combining FTIR, GIXRD and Raman results, it can be concluded that from ML0 to ML77 the c-Si phase increases, whereas the c-SiC phase decreases due to the O incorporation. For ML50, the c-SiC phase decreases further whereas the c-Si phase stays unchanged. The decrease in c-SiC phase is probably due to the competition between Si-O and Si-C bonds as observed in $Si_{0.50}C_{0.50}$ SL. This is why the c-SiC phase decreases more strongly in ML50 than in ML77 layers: The O is incorporated directly into the $Si_{0.50}C_{0.50}$ sublayers. The increase of c-Si phase due to O incorporation is probably due to an already mentioned hindering effect of O on Si diffusion. Therefore, the local Si density in the ML stays higher during annealing than without O and more c-Si phase forms – probably in the form of larger Si NC. However, this difference in Si NC size stays an assumption because it is too small to be proven experimentally. The second possible explanation for an increased c-Si phase could be a higher number of Si NC in ML with O, perhaps because the incorporated O acts as a nucleation seed.

Chapter 6

Passivation of Si nanocrystals

The efforts made to improve $Si_xC_{1\text{-}x}$ *quality by defect passivation are described in this chapter. After deducing some principle informations about band structure and defect distribution from spectrophotometry (R&T) measurements, two types of H passivations on all kind of samples presented so far in this work were applied. Forming gas anneal was done by H. Steidl and remote plasma H passivation by F. Feldmann. The very few cases of successful H passivation are discussed based on photoluminescence (PL) spectroscopy. Finally, oxygen incorporation in ML is presented to show a promising increase in PL intensity.*

6.1 Defects in $Si_xC_{1\text{-}x}$

The absolute luminescence quantum yield of $Si_xC_{1\text{-}x}$ samples was estimated by Schnabel *et al.* [108] to be very low ($< 10^{-6}$), indicating a high density of nonradative recombination-active defects. Kořínek *et al.* [153] verified this high defect density in Si-NC/SiC ML by determining carrier dynamics in the picosecond range with the help of ultrafast transient transmission measurements. This is the reason for the very weak PL signal from $Si_xC_{1\text{-}x}$ samples, which do not allow a conclusive investigation of the band structure. Some information about the band structure can be given by R&T measurements in the UV-Vis wavelength range (cf. Sec. 2.4.2). Examples of the derived absorptions coefficients (α) from R&T measurements for increasing annealing temperatures are depicted in Fig. 6.1. These absorption spectra allow some general statements about the optical properties and the band structure of our samples.

First of all, the additional Si in the $Si_{0.77}C_{0.23}$ samples (Fig. 6.1 (b)) leads to a higher absorption compared to the $Si_{0.50}C_{0.50}$ samples (Fig. 6.1 (a)) in the whole optical wavelength range. The apparent saturation of α above 3.0 eV in the $Si_{0.77}C_{0.23}$ samples is a consequence of the sensitivity limit of the measurement setup. Above 3.0 eV, the transmitted light is too weak to be detected. Therefore, no further changes in α can be resolved.

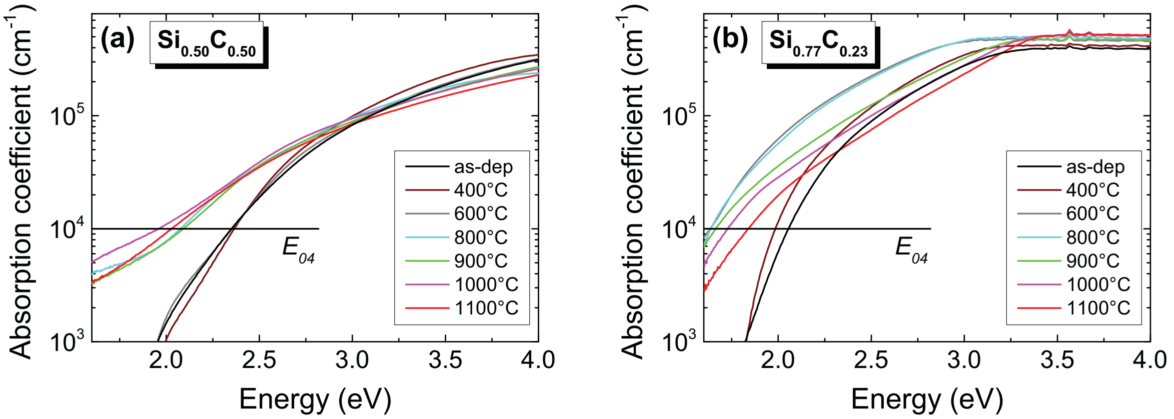

Figure 6.1: Absoption coefficients derived from R&T measurements for $Si_{0.50}C_{0.50}$ samples and for $Si_{0.77}C_{0.23}$ samples on quartz substrates annealed at increasing temperatures.

Second, there is a remarkable change in α for $Si_{0.50}C_{0.50}$ samples after annealing between 600°C and 800°C and no further change for further increase in annealing temperature. Hence, H effusion changes the optical properties of $Si_{0.50}C_{0.50}$, but not the crystallization from a-SiC to 3C-SiC. In the case of $Si_{0.77}C_{0.23}$, there is a significant change in α for every annealing temperature except between 600°C and 800°C. In this case, not only the H effusion but also the Si crystallization leads to a change of the optical properties. This is in accordance with the optical properties of SiC and Si from the literature as briefly introduced in Sec. 1.2.

Third, all α curves flatten in a similar way upon annealing, leading to additional absorption around E_{04}. Therefore, one can draw the following conclusions in terms of optical bandgap and band structure: Due to the quite steep increase of absorption in the amorphous samples at E_{04}, this energy can be assumed as optical band gap energy. The flatter absorption curves for annealed samples show no steep increase of absorption, which means that the assignment of a certain optical bandgap is not possible for annealed samples. In terms of band structure, one has to distinguish between $Si_{0.50}C_{0.50}$ (Fig. 6.1 (a)) and $Si_{0.77}C_{0.23}$ (Fig. 6.1 (b)). In the case of $Si_{0.50}C_{0.50}$, we attribute the flattening of α to an enhanced defect density and therefore an enhanced density of states in the bandgap, which leads to additional defect absorption, manifested by additional absorption around E_{04}. In the case of $Si_{0.77}C_{0.23}$, flattening of α is equally attributed to an enhanced defect density. However, the additional absorption around E_{04} is likely a combination of defect absorption and absorption from the formation of the Si phase due to progressing phase separation with increasing annealing temperature. It seems that during H effusion, mainly phase separation occurs (only slight flattening but strong shift of α) whereas the subsequent crystallization mainly leads to defect formation (strong flattening of α).

These assumptions are supported by the shape of the Tauc plots for the samples in Fig. 6.1 (not shown here). They are straight lines in case of amorphous samples and therefore allow a derivation of an optical bandgap as listed in Tab. 6.1 together with literatures values.

Table 6.1: Comparision between literature values and the values obtained in this work for E_G(a-$Si_xC_{1\text{-}x}$:H).

x	E_G(a-$Si_xC_{1\text{-}x}$:H) (eV)	Reference
0.46	2.65 ± 0.02	[64]
0.50	2.2 ± 0.1	this work
0.50	≈ 2.3	[154]
0.62	2.49 ± 0.05	[64]
0.72	2.26 ± 0.05	[64]
0.77	1.9 ± 0.1	this work
0.77	≈ 1.9	[154]

The values coincide well with the values reported by Baker *et al.* [154], but are lower than the values reported by Mui *et al.* [64]. It is supposed that the differences in optical bandgap values result from the degree of chemical order in the a-$Si_xC_{1\text{-}x}$ samples. The chemical order of $Si_{0.50}C_{0.50}$ samples is maximal if only Si-C bonds exist. With decreasing order, Si-Si and C-C bonds occur. In general, a higher chemical order leads to higher bandgaps [76]. Mui *et al.* [64] claim complete chemical ordering in their a-$Si_xC_{1\text{-}x}$ samples. Probably the degree of chemical ordering and therefore the bandgap in the $Si_xC_{1\text{-}x}$ samples investigated in this thesis is lower.

For annealed samples, the Tauc plots show strong curvatures, which makes a determination of a bandgap impossible. The reason for this is not only that Tauc plots are not the right method to determine a bandgap for semi-crystalline samples, but that there *is* no distinct bandgap in the annealed samples because they absorb over the whole optical wavelength range by means of numerous defect states, different phases (a-Si/a-SiC/c-Si/c-SiC), and NC of different sizes.

One cannot say for certain which kind of defects prevail in our samples. As it is known from literature that both C and Si dangling bonds are present in a-$Si_xC_{1\text{-}x}$ and that Si dangling bonds dominate for Si-rich material [76, 155–157], it can be assumed that they also play an important role in our samples. This assumption is supported by the above described increase of defects due to H effusion in $Si_{0.50}C_{0.50}$ samples. Because a further increase of defects through crystallization in $Si_{0.77}C_{0.23}$ was observed and furthermore taking into account the different lattice constants of c-Si and 3C-SiC (see Tab. 1.1), a significant enhancement of the defect density due to lattice mismatch and strain at grain boundaries is supposed. Therefore, defect passivation is attempted by two different methods. One method is treating the samples with H for dangling bond passivation. The other method is the introduction of O into the layers to decrease the lattice mismatch at grain boundaries either by preventing SiC crystallization or by forming an amorphous SiO_2 shell around Si NC.

6.2 Hydrogen passivation

The hydrogen passivation was carried out with molecular H_2 by forming gas anneal (FGA) and with atomic H by remote plasma H passivation (RPHP) as described in Sec. 2.3 for all annealed samples described in this work so far. PL measurements were conducted for all these samples before passivation, after FGA and after RPHP. After about 200 carefully performed PL measurements on all kinds of samples with and without passivation, it is stated clearly that no significant change or enhancement of PL signal was observed from the samples after FGA or RPHP. There are two exceptions to this observation: The first one concerns the oxygen incorporated ML, which will be treated separately in the next section. The second exception concerns Si_xC_{1-x} SL samples treated by RTA at low annealing temperatures. These samples show a certain change and enhancement of PL signal after RPHP as depicted in Fig. 6.2 for $Si_{0.63}C_{0.37}$ samples.

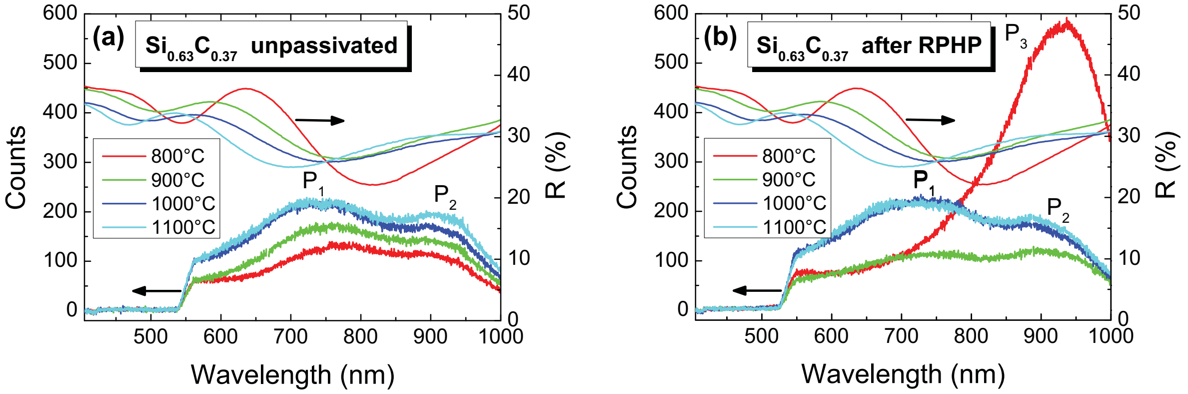

Figure 6.2: Left-hand ordinate: PL spectra of $Si_{0.63}C_{0.37}$ samples annealed at different temperatures before (a) and after (b) RPHP. Right-hand ordinate: reflectance curves of $Si_{0.63}C_{0.37}$ samples annealed at different temperatures.

Typical PL spectra of $Si_{0.63}C_{0.37}$ samples are depicted in Fig. 6.2 (a), (left-hand ordinate). As described in Sec. 2.4, it is useful to plot the reflection spectra of the samples together with the PL spectra (right-hand ordinate) to estimate the influence of thin film interference on the PL spectra. The start of the abscissa at 405 nm corresponds to the laser wavelength. One can derive the reflection value of the laser light directly from the intercept of the reflection curves with the ordinate.

Fig. 6.2 (a) shows that the overall PL intensity increases slightly with increasing annealing temperature. This effect can be attributed to the reflection of the laser light at the sample. The reflection value at 405 nm decreases in the same way as the PL intensity increases. That means simply that more PL light is generated if more laser light penetrates the samples.

All PL spectra show two broad peaks, one between 700 and 800 nm (P_1), and one around 900 nm (P_2). As the most pronounced minima in reflectance (red and cyan curve) do not coincide with P_1 or P_2, the influence of thin film interference can be neglected for these samples. The possible assignment of P_1 and P_2 will be discussed later. After FGA (spectra not shown here), neither the intensity nor the shape of the PL spectra change. However, after RPHP (Fig. 6.2 (b)), the sample annealed at 800°C (red) shows an intense peak around 940 nm (1.3 eV, P_3) whereas the samples annealed at higher temperatures show no significant change in PL spectra. As discussed in Sec. 2.4.1, the PL intensity is systematically underestimated for $\lambda > 950$ nm. This underestimation increases for increasing wavenumbers. Therefore, it cannot be excluded that the real position of P_3 is at slightly higher wavenumbers. However, this uncertainty does not influence the validity of the following considerations.

P_3 can be attributed clearly to the bandgap in amorphous material as it is observed also in PL spectra of a-$Si_{0.77}C_{0.23}$:H and a-$Si_{0.63}C_{0.37}$:H samples (cf. App. 9) but with much higher intensities. Analogously to a-Si:H [18], we assume that P_3 occurs from radiative band tail to band tail transitions and that the peak energy is therefore lower than E_G determined by the Tauc method in the previous section. This shows that for $Si_{0.63}C_{0.37}$ samples annealed by RTA up to 800°C, H passivation by RPHP is possible, but not for higher annealing temperatures. The reason for this will be explained in the end of this section. A similar behaviour is observed in Fig. 6.3 for $Si_{0.77}C_{0.23}$ samples.

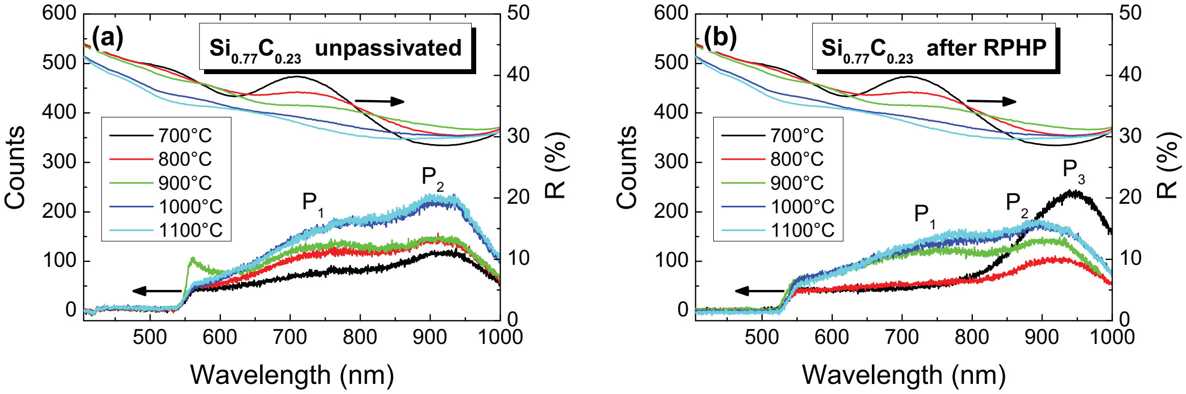

Figure 6.3: Left hand ordinate: PL spectra of $Si_{0.77}C_{0.23}$ samples annealed at different temperatures before (a) and after (b) RPHP for H passivation. Right-hand ordinate: reflectance curves of $Si_{0.77}C_{0.23}$ samples annealed at different temperatures.

All unpassivated PL spectra (Fig. 6.3 (a)) also show P_1 and P_2 with the only difference that the intensity of P_1 is slightly lower and the intensity of P_2 is slightly higher than for unpassivated $Si_{0.63}C_{0.37}$ samples. The increase of PL intensity at 550 nm of the 900°C sample (green) is probably due to an irregularity of the sample surface. The temperature series of the PL spectra starts with samples annealed at 700°C (black) for $Si_{0.77}C_{0.23}$ samples (Fig. 6.3), but at 800°C for $Si_{0.63}C_{0.37}$ samples (Fig. 6.2). This is due to the fact that $Si_{0.63}C_{0.37}$ samples still show a remarkable H content after annealing at 700°C and therefore, H passivation is not useful. This confirms the findings from Sec. 4.1 of a connection between the Si content and the temperature of complete H effusion.

FGA shows no effect on the spectra whereas RPHP leads to the P_3 peak for the sample annealed at 700°C (black). A remarkable effect here is the significant decrease of P_1 with increasing P_3 for the samples annealed at 700°C (black) and at 800°C (red). Consequently, P_1 is attributed to a transition from Si dangling bonds in SiC [76] to the SiC valence band, which are passivated in case of successful H in-diffusion.

The logical assignment of P_2 (1.38 eV) would be a-Si or Si NC in the samples. However, this assumption is untenable because this peak is also observed in $Si_{0.50}C_{0.50}$ samples where no Si phase is present. Therefore, P_2 is attributed also to SiC defect states, which cannot be further characterized.

Summarising the H passivation results, FGA does not show any influence on the PL spectra. RPHP does not show an influence on samples treated by FA, by FLA and by RTA above 800°C. However, for RTA, $Si_{0.63}C_{0.37}$ and $Si_{0.77}C_{0.23}$ samples annealed under 800°C, RPHP passivation was successful. A possible explanation for the difference of FGA and RPHH is the following: During RPHP, the H_2 molecules are dissociated into H radicals in the plasma and then they reach the surface. Whereas during FGA, H_2 molecules must adsorb at the surface and dissociate into H radicals to passivate dangling bonds [53]. This dissociation mechanism is reported to be mediated by surface damage and by vacancies [158]. Probably the dissociation is not effective in the investigated $Si_xC_{1\text{-}x}$ samples as the surface is very smooth and no surface damage is introduced by polishing or similar treatments. There is no information about the vacancy density in the samples, but the inefficiency of FGA can be taken as indication for a low vacancy density.

The finding that RPHP is possible only < 800°C can be explained by the diffusion of H radicals in the $Si_xC_{1\text{-}x}$ samples. H diffusion is reported to take place via interstitials and vacancies [158] in c-Si and via bond states in a-Si [159]. One can assume that the increasing crystallization, which occurs for increasing annealing temperatures, leads to a decrease in vacancies and interstitial sites for H diffusion. Therefore, no passivation occur > 800°C. In other words, the samples densify upon annealing. This assumption is supported by the thickness measurement from SEM cross sections: Both $Si_{0.77}C_{0.23}$ and $Si_{0.63}C_{0.37}$ as-dep samples are ≈ 205 nm thick, shrink to an intermediate thickness of ≈ 180 nm after annealing at 800°C, and further to ≈ 170 nm after 900°C. For higher

annealing temperatures, the samples thicknesses stay constant. This means that at 800°C, the H effusion leaves behind a vacancy rich material which allows H in-diffusion but densifies upon annealing. However, it remains unclear why H does not diffuse via dangling bond states in the samples annealed at high temperatures.
Other groups observed the same difficulties in obtaining an effective H passivation of $Si_xC_{1\text{-}x}$ layers. Yamada *et al.* [54] reported a successful in-diffusion of H via hydrogen plasma treatment into $Si_{0.56}C_{0.32}O_{0.12}/Si_{0.40}C_{0.35}O_{0.25}$ ML after an annealing step of 30min@900°C under forming gas. However, they still detect a small amount of H after annealing and before passivation in their layers. This supports our result that effective H in-diffusion only takes place if the samples were treated before with the maximal thermal budget required for H effusion. Furthermore, Yamada *et al.* [54] show that the diffusion coefficient for H in $Si_{0.56}C_{0.32}O_{0.12}/Si_{0.40}C_{0.35}O_{0.25}$ ML lies between the higher one in SiO_2 and the very low one in a-SiC. As their samples contain much more O than those investigated in this thesis, one can conclude that their H diffusion coefficient is lower than the one obtained for their samples. Ding *et al.* [53] investigated FGA and RPHP passivation in SiC SL, $SiO_{1.2}$ SL and SiC/$SiO_{1.2}$ ML after annealing them for 1h@1050°C. With the help of electron spin resonance (ESR) measurements, they show that FGA successfully passivated the $SiO_{1.2}$ SL, had no influence on the SiC SL at all, and only a small passivation effect on the SiC/$SiO_{1.2}$ ML. RPHP leads to less effective passivation in the case of $SiO_{1.2}$ SL and SiC/$SiO_{1.2}$ ML, but shows some effect on SiC samples. However, the spin density is still approximately $1\cdot10^{19}\,\mathrm{cm}^{-3}$. A PL signal was only detected for $SiO_{1.2}$ SL, but not for SiC/$SiO_{1.2}$ ML and SiC SL, neither before nor after passivation. This work also confirms the results from this thesis and shows that our PL setup is very sensitive as we observe at least a small amount of PL signal for all $Si_xC_{1\text{-}x}$ samples.

6.3 Passivation by CO_2

As reported in Sec. 5.2, oxygen (O) was successfully incorporated during growth into the $Si_xC_{1\text{-}x}$ samples by a CO_2 precursor gas. Therefore, a passivation effect either on Si dangling bonds or by reducing the SiC crystallinity is expected. However, no clear evidence for enhanced PL signal in $Si_xC_{1\text{-}x}$ SL samples with increased O content was observed. This means that either no defect passivation occurred or that defect passivation of radiative and non-radiative defects somehow compensated for each other. It is also possible that an increasing O content leads to defect passivation on the one hand and to creation of new defects on the other. In the case of $Si_{0.77}C_{0.23}/\ Si_{0.50}C_{0.50}$ ML, the O incorporation seems to change the PL signal significantly. These PL spectra (left-hand ordinate) are depicted together with the reflectance of the samples (right-hand ordinate) in Fig. 6.4 (a). The same ML samples as described in Sec. 5.2 were measured: One without O (ML0, brown), one with O in the $Si_{0.77}C_{0.23}$ sublayers (ML77, orange), and one with O in the $Si_{0.50}C_{0.50}$ sublayers (ML50, red).

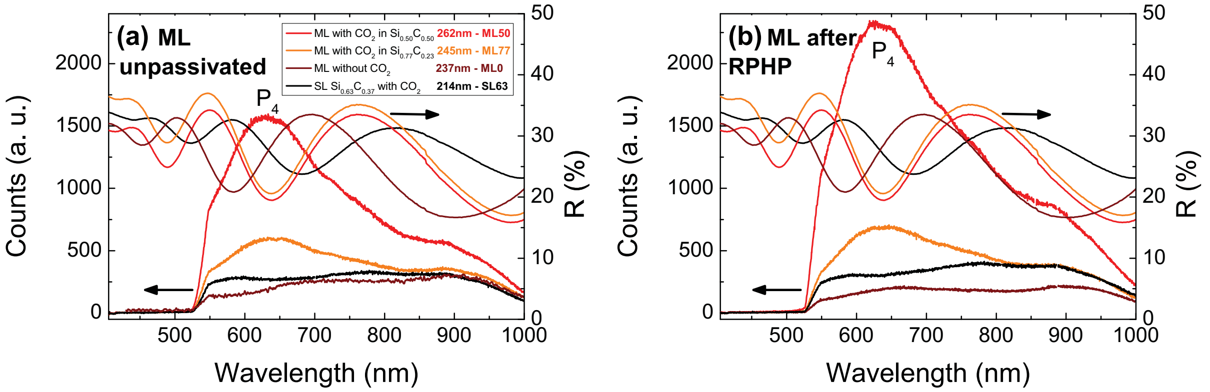

Figure 6.4: Left-hand ordinate: PL spectra of ML and SL samples with and without O before (a) and after (b) RPHP for H passivation. Right-hand ordinate: reflectance curves of ML and SL samples with and without O.

For comparison, a SL with the same overall composition as the ML is also plotted (SL63, black). The thin-film interference maxima and minima in the reflection curves are much more pronounced than in the samples that were discussed in the last section (Fig. 6.2 and 6.3). This results from the fact that the layers in this batch are about 100 nm thicker than the ones discussed before. The respective average layer thicknesses from SEM cross sections are specified in Fig. 6.4 (a). The error in layer thickness is ±5 nm.

For both ML samples with incorporated O, one can observe a broad, intense PL peak around 630 nm (P_4, ≈ 2 eV). This peak was never observed in any other $Si_xC_{1\text{-}x}$ sample in this work. We will discuss now if P_4 can be attributed to the positive influence of O incorporation or if it results from measurement conditions or other sample parameters like sample thickness, thin-film interferences, and laser incoupling.

P_4 is exactly at the same position as a pronounced minimum in reflection, meaning that its position and intensity is probably strongly influenced by thin-film interferences. Nevertheless, it seems unlikely that the whole intensity of P_4 is a result of interference effects because the minimum in reflectance for SL63 is nearly as pronounced as the minima of ML50 and ML77 and is only ≈ 40 nm blue-shifted. But the PL intensity of SL63 is about 2x lower than the PL intensity of ML77 and about 6x lower than the PL intensity of ML50. The higher thicknesses (1.1x for ML77 and 1.2x for ML50) compared to SL63 also can not explain the increase in PL intensity. Finally, one must look at the incoupling of the laser light, represented by the reflectance at 405 nm in Fig. 6.4. It is stronger for ML77 than for ML50. This could be the reason for the difference in the PL intensity of these two samples. However, the reflectance at 405 nm for ML0 and SL63 lies between the reflectance of ML77 and ML50 and therefore cannot explain why the PL spectra of sample ML0 and SL63 are less intense than the PL spectrum of sample ML77 and ML50. One can conclude that the P_4 PL peak intensity is enhanced by the effect of thin-film interference, laser incoupling, and film thickness. However, there must still be "real" PL signal around 630 nm in ML samples with O. It will now be discussed where this signal could come from.

Either P_4 results from Si NC or from the SiC bandgap. PL from O-terminated Si NC is usually reported in the wavelength range from very close to the bulk Si bandgap (1.1 eV) to 1.6 eV [160]. O-related states in the bandgap of the Si NC are assumed to hinder further bandgap opening [161]. If the Si NC are H-terminated, bandgaps up to approximately 2.4 eV are reported [162]. In our case, the Si NC are either O or C terminated. Theoretical calculations of the confinement energy of Si NC in SiC show that it is expected to be smaller than for Si NC in SiO_2 [27]. Therefore, it is quite unlikely but still cannot be excluded that the P_4 PL peak results from Si NC. It seems more plausible that P_4 results from a radiative transition in SiC. As it is known from a-Si:H that the transitions between band tails are strongly radiative whereas the transitions from the band edges to defect states are mainly non-radiative [18], it is proposed that P_4 corresponds to a transition between SiC band tails. This would mean that the O in the ML leads to a strong passivation of nonradiative defect states in SiC. As mentioned before, this could be due to passivation of c-Si/c-SiC interfaces by inducing an Si-O layer or by the reduction of SiC crystallinity. Both the formation of Si-O bonds and the reduction of c-SiC phase have been verified to occur in the ML in Sec. 5.2. However, it remains unclear why this passivation due to O incorporation should occur in ML but not in SL.

All samples from Fig. 6.4 (a) were subjected to FGA and RPHP. No significant difference of the PL signal was observed for FGA samples. But after RPHP passivation (Fig.6.4 (b)), the ML77 sample shows a slight increase and the ML50 samples a significant increase of the PL signal whereas the other PL spectra stay unchanged. The reason could be that the additional O in the layers increases the H diffusion coefficient and therefore the efficiency of the H passivation as expected from literature [54]. Once again this leads to the question why this process should take place in ML and not in SL. One possible reason is the fact that the SL63 sample unintentionally contains less O than ML50 and ML77 sample (cf. Sec. 5.2).

In summary, it is stated that we observed some promising results concerning the beneficial effect of O in $Si_{0.77}C_{0.23}/Si_{0.50}C_{0.50}$ ML, no matter if the O is incorporated in the $Si_{0.77}C_{0.23}$ or in the $Si_{0.50}C_{0.50}$ sublayers. The additional PL peak at 630 nm (≈ 2 eV), which increases through RPHP passivation, hints at defect passivation and facilitated H diffusion through O incorporation.

Summary and outlook

This Ph.D. thesis addresses the deposition, characterization and improvement of Si nanocrystal layers embedded in a SiC matrix (Si NC/SiC) as future absorber material for top cells of an all-Si tandem solar cell. The required enlargement of the Si NC bandgap to ideally 1.7 eV is aimed to achieve with the help of quantum confinement (QC). No unambiguous evidence of QC in Si NC/SiC samples were presented in the literature up to now. Even though this also was not possible during this Ph.D. thesis, some necessary preconditions for QC were successfully complied, which are (i) a better understanding and control of the crystallization mechanism, and (ii) size control of the Si NC and defect passivation.

The deposition of amorphous $Si_xC_{1\text{-}x}$:H layers was conducted by plasma-enhanced chemical vapor deposition (PECVD) from the precursor gases SiH_4, CH_4 and H_2. The ratio of gas fluxes allows a variation of Si content in the samples. During the annealing step subsequent to layer deposition, H effusion, formation of Si NC, and crystallization of the SiC matrix occurs. As this crystallization represents the key process for the final properties of the samples, it was investigated in detail. Therefore, a variety of annealing techniques were established and applied. Conventional furnace annealing (FA) with slow heating ramps and annealing times between 1 min and several days. Rapid thermal annealing (RTA) and a zone melting recrystallization (ZMR) furnace with annealing times of several minutes and heating rates of about 10°C/s. And flash lamp annealing (FLA) for faster heating ramps and annealing times in the ms range.

All Si NC/SiC samples were subjected to a comprehensive structural characterization, completed with optical measurements. The layer thickness was investigated by scanning electron microscopy (SEM) cross sections. The development of crystalline Si (c-Si) and crystalline SiC (c-SiC) phase was investigated by grazing incidence X-ray diffraction (GIXRD). The evaluation of GIXRD patterns allows furthermore an estimation of the SiC and Si NC size. This was complemented by information from Fourier transform infrared (FTIR) spectroscopy, which gives insight into the SiC crystallinity and from Raman spectroscopy, yielding information about the Si crystallinity. Photoluminescence (PL) and spectrophotometry (R&T) measurements were also conducted to investigate the absorption and emission properties of amorphous and crystalline samples. The application of GIXRD, FTIR and Raman measurements to Si NC/SiC thin films were significantly improved during this work in terms of signal to noise ratio and concerning a reliable and reproducible data treatment as well as a correct interpretation of the results.

The formation of Si NC in the targeted size range of some nm is possible with all applied annealing techniques after adapting the annealing parameter, including annealing times of several hours down to the ms range. Unfortunately, the Si crystallization is always accompanied by the undesired SiC crystallization, which is probably mainly responsible for the high defect density in the Si NC/SiC material. A rough estimation of the activation energy for Si and SiC crystallization with the method proposed by Liu *et al.* [89] shows that they are both in the same range between 2 and 6 eV. This explains why a separation of Si and SiC crystallization is not possible via the annealing temperature. However, crystallization theory predicts that the maximum growth rate of Si and SiC does probably not take place at the same temperature. Estimating the maximum growth temperature of Si turned out to be the key to reach a reduction of SiC crystallinity. Therefore, a two-step anneal was applied. A preanneal step at low temperatures for H effusion and nucleation and an annealing step at the maximum growth rate temperature as short as possible. As this temperature is near the melting point of Si, and fast heating ramps are required, the two-step anneal could only be realised with the ZMR and the FLA setup. With both setups, the SiC crystallinity was successfully reduced for a certain Si NC size by the two-step anneal.

The estimation of the activation energy for Si crystallization shows furthermore that it decreases for samples with increasing Si content, signifying a higher Si diffusion for increasing Si content. This was explained in Sec. 4.2 either with the help of theoretical calculations from Mattausch [142], or with the shorter distances between Si atoms for higher Si content. The larger diffusion coefficient for higher Si contents explains the findings of larger Si NC and higher Si crystallinity for samples treated with the same annealing process but different Si contents.

As expected, the crystallization turned out to be a thermally activated process. This means that it proceeds faster with increasing annealing temperature. Consequently, a certain Si NC size can be reached either with a long anneal at low temperatures, or a short anneal at high temperatures. Both kind of heating ramps lead to surprisingly similar structural properties of the samples. It shows that nucleation occurs mainly during the ramping up time and that crystal growth is favored over nucleation as soon as a number of nuclei are present.

The Si NC size control is an indispensable precondition for successful quantum confinement.

For this purpose, two routes were proposed in this work. The Si NC size is shown to increase with increasing Si content of the $Si_xC_{1\text{-}x}$ layers. Thus, the Si NC size can be adjusted by adjusting the Si content. The advantage of this method is the fact that singlelayers can be deposited instead of multilayers (ML). The disadvantage is the uncontrollability of the Si NC spacing and the wide size distribution. Furthermore, the correlation between Si content and Si NC size makes it difficult to distinguish between a quantum confinement effect and the absorption characteristic of a $Si_xC_{1\text{-}x}$ layer with varying Si content. The second route, which promises Si NC size control, is with the help of a ML structure. Usually, Si NC/SiC ML structures show strong intermixing during the annealing step and are therefore not suitable for Si NC size control. In this work it is shown that the ML structure can be hindered from intermixing by oxygen (O) incorporation during deposition. Although there is not enough data so far to prove that the maintenance of the ML with the help of O is accompanied by Si NC size control, by Si NC surface passivation, and by quantum confinement, this approach promises to fulfill those demands and will therefore be pursued further.

Oxygen incorporation into ML furthermore causes an increase in PL intensity, which is attributed to the passivation of nonradiative defects in the samples. A further increase in PL signal after remote plasma H passivation (RPHP) suggests a facilitated H diffusion and further defect passivation due to O incorporation. For layers without additional O, H passivation is only successful for short annealing processes prior to H passivation at annealing temperatures $< 900°C$ where the samples are hardly crystallized. As crystallization is accompanied by densification of the $Si_xC_{1\text{-}x}$ layers, these results reveal that the propagation of H in the samples probably takes place via vacancies. Crystallization and densification of the samples lead to a decrease in vacancy density and therefore hinders H in-diffusion.

Although steps towards the control of Si NC formation and defect reduction in Si NC/SiC layers have been made during this thesis, further work is necessary to achieve a good absorber material for solar cell applications. Electron spin resonance measurements should be conducted to gain insight into the kind of defects predominant in the samples and to verify defect reduction due to O incorporation and H passivation. To raise the chance to detect QC, the PL analysis should be improved by simulating the modulation function of the PL signal. The promising results of ML surviving the annealing step due to O incorporation should be investigated further by a sublayer thickness variation to examine if size control can be achieved by this method. These ML should be treated with a two-step anneal for reduced SiC crystallinity. Additionally, transmission electron microscopy measurements should be conducted to verify the maintenance of the ML and show the Si NC size distribution.

Appendix

1 List of abbreviations

Acronym	Meaning
3C-SiC/β-SiC	Cubic SiC
a-	Amorphous
a-Si$_x$C$_{1\text{-}x}$:H	Hydrogenated amorphous SiC
as-dep	As-deposited
Ar	Argon
BGC	Back ground correction
c-	Crystalline
C	Carbon
CZ Si	Czochralski Si
FA	Furnace Annealing
FGA	Forming gas anneal
FLA	Flash lamp annealing
FTIR	Fourier transform infrared spectroscopy
FWHM	Full width at half maximum
FZ Si	Float zone Si
GIXRD	Grazing incidence X-ray diffraction
H	Hydrogen
IF	Interferogramm
ML	Multilayer
N	Nitrogen
NC	Nanocrystal(s)
O	Oxygen
OES	Optical emission spectroscopy
PECVD	Plasma enhanced chemical vapour deposition
PL	Photoluminescence
QD	Quantum dot(s)
%R	Reflectance
RPHP	Remote plasma hydrogen passivation
R&T	Reflectance and Transmittance

Acronym	Meaning
RTA	Rapid thermal annealing
SC	Solar cell
Si	Silicion
SiC	Silicon carbide
SIMS	Secondary ion mass spectroscopy
SL	Singlelayer
SRC	Si rich carbide
%T	Transmittance
TA/LA	Transversal/longitudinal acoustic
TO/LO	Transversal/longitudinal optic

2 List of symbols

Symbol	Dimension	Meaning
α	$\mathrm{cm^{-1}}$	Absorption coefficient
β	°	Angle between the Si(100) and the Si(311) planes in Si substrate
Γ	%	Absorbed fraction
δ	$\mathrm{g\,cm^{-3}}$	Density
$\Delta\epsilon_{\mathrm{F}}$	eV	Quasi-Fermi level splitting
ΔG	eV	Gibbs energy (Free enthalpy)
ΔG^{*}	eV	Critical free activation energy of nucleus formation
ΔG_{D}	eV	Diffusion barrier
ΔG_{G}	eV	Free activation energy for crystal growth
$\Delta G^{*}_{\mathrm{H}}$	eV	Critical free activation energy of hetero. nucleus formation
$\Delta G_{\mathrm{I}}/\sigma$	$\mathrm{eV}/\ \mathrm{eV\,m^{-2}}$	Free interface enthalpy
ΔG_{M}	eV	Free Misfit enthalpy
$\Delta G_{\mathrm{V}}/\Delta g_{\mathrm{V}}$	$\mathrm{eV}/\ \mathrm{eV\,m^{-3}}$	Free volume enthalpy
Δn	$\mathrm{m^{-3}}$	Excess carrier density
$\Delta_{\mathrm{S}}H$	eV	Melting enthalpy
ΔT	°C	Undercooling
$\epsilon(\lambda)$	$\mathrm{F\,m^{-1}}$	Dielectric function
$\epsilon_{\mathrm{e/h}}$	eV	Eigenvalues energy electron/holes
ζ	$\mathrm{cm^{2}\,s^{-1}}$	Thermal diffusivity
η	%	Solar cell efficiency
θ	°	Diffraction angle
κ	$\mathrm{kg\ s^{-2}}$	Spring constant
λ	nm	Wavelength
ν	$\mathrm{cm^{-1}}$	Frequency of IR vibration
$\sigma_{\mathrm{G/L}}$	$\mathrm{cm^{-1}}$	Gaussian/Lorentzian FTIR peak FWHM
ϕ	°	Orientation of GIXRD sample
$\phi(\vec{x})_{\mathrm{e/h}}$	-	Wavefunction electron/hole
χ_{Si}	%	Si crystallinity
a	Å	Lattice constant
A/n	$\mathrm{t^{-1}}$/-	Parameter for crystalline fraction
$A_{\mathrm{G/L}}$	$\mathrm{cm^{-2}}$	Gaussian/Lorentzian FTIR peak area
A_{L}	%	Absorptance layer
A_{S}	%	Absorptance substrate

Symbol	Dimension	Meaning
b	Å	Distance of the lattice planes
$B(\nu)$	%	Absorbance spectrum
c_{p}	$\mathrm{J\,g^{-1}K^{-1}}$	Specific heat capacity
d	nm	Quantum dot/Nanocrystal size
$D(\epsilon)$	$\mathrm{m^{-Dim}eV^{-1}}$	Density of states
D_{Si}	$\mathrm{m^2\,s^{-1}}$	Diffusion coefficient of Si
$d^{\mathrm{Si/SiC}}_{\mathrm{NC\_100}}$	$\mathrm{m^3}$	Si and SiC NC size corresponding to Si and SiC crystallinity of 100%
$d^{\mathrm{Si/SiC}}_{\mathrm{NC\_max}}$	$\mathrm{m^3}$	Si and SiC NC size at maximum crystalline fraction f_{max}
E_{04}	eV	E_{04} bandgap
E_{C}	eV	Conduction band energy
E_{G}	eV	Bandgap energy
E_{Tauc}	eV	Tauc bandgap
E_{V}	eV	Valence band energy
f	%	Transformed crystalline fraction
F_{hkl}	Number	Structure factor for the lattice plane (hkl)
f_{max}	%	Maximum transformed crystalline fraction
$G(\nu)$	$\mathrm{cm^{-1}}$	Gaussian FTIR mode
$\hbar$	eV s	Reduced Planck constant ($6.58212 \cdot 10^{-16}$ eV s)
hkl	Numbers	Miller indices
I_0	$\mathrm{W\ m^2}$	Incident intensity
I_{amo}	a.u.	Amorphous Raman spectrum
I_{cry}	a.u.	Crystalline Raman spectrum
I_{semi}	a.u.	Semicrystalline Raman spectrum
I_{t}	$\mathrm{W\ m^2}$	Transmitted intensity
k	$\mathrm{W\,cm^{-1}K^{-1}}$	Thermal conductivity
k_{B}	$\mathrm{eV\,K^{-1}}$	Boltzmann constant ($8.61733 \cdot 10^{-5}\ \mathrm{eV\,K^{-1}}$)
$L(\nu)$	$\mathrm{cm^{-1}}$	Lorentzian FTIR mode
L_{D}	μm	Thermal diffusion length
m^*	g	Effective mass
m^*_C	g	Effective mass holes in valence band
$m_{\mathrm{Si/SiC}}$	$\mathrm{g\,mol^{-1}}$	Molar masses Si/SiC
$M_{\mathrm{Si/SiC}}$	%	Non-normalized mass fraction Si/SiC
m^*_V	g	Effective mass electrons in conduction band

Symbol	Dimension	Meaning
n, m, l	-	Quantum numbers
N_{A}	mol^{-1}	Avogadro constant ($6.02214 \cdot 10^{23}\,\mathrm{mol}^{-1}$)
$n_{\mathrm{Si/SiC}}$	$\mathrm{at\,cm}^{-3}$	Number of atoms in a cubic cm Si/SiC
$N(\mathrm{X}-\mathrm{Y})$	cm^{-3}	X-Y bond density
p	Number	Data points Raman
P	Number	Number of data points Raman
Q	eV	Effective activation energy
$Q(f)_T$	eV	Effective activation energy for a certain f in a limited T range
$Q_{\text{Si-C}}/K_{\text{Si-C}}$	$\mathrm{cm}^{-1}/\mathrm{cm}^{-2}$	Proportionality constants FTIR
r	nm	Radius of particle
R	%	Reflectance
r^*	nm	Critical nucleus radius
s	nm	Sample thickness
S	Number	Scaling factor Raman
s_{b}	nm	Total barrier thickness
s_{w}	nm	Total well thickness
T	%	Transmittance
t_0	min	Crystallization time during ramping-up during FA
T_{cry}	%	Crystallization temperature
T_{S}	°C	Melting point
$T_{\mathrm{T}}^{\mathrm{Si}}$	°C	Melting point Si
$T_{\mathrm{T}}^{\mathrm{SiC}}$	°C	Decomposition point SiC
v	$\mathrm{m}^{-3}\,\mathrm{s}^{-1}$	Transformation rate per unit volume
v_0	$\mathrm{m}^{-3}\,\mathrm{s}^{-1}$	Time-independent transformation rate per unit volume
V_{conf}	eV	Confinement potential
V_{cryst}	m^3	Crystalline volume
v_{G}	$\mathrm{m}^{-3}\,\mathrm{s}^{-1}$	Crystal growth rate per unit volume
v_{G0}	$\mathrm{m}^{-3}\,\mathrm{s}^{-1}$	Time-independent crystal growth rate per unit volume
v_{N}	$\mathrm{m}^{-3}\,\mathrm{s}^{-1}$	Nucleation rate per unit volume
v_{N0}	$\mathrm{m}^{-3}\,\mathrm{s}^{-1}$	Time-independent nucleation rate per unit volume
V_{NC}	m^3	Si NC volume
$V_{\mathrm{Si/SiC}}$	m^3	Si/SiC volume fraction
V_{tot}	m^3	Total volume
$V_{\mathrm{tot}}^{\mathrm{Si/SiC}}$	m^3	Total Si/SiC volume
$\vec{x}$	m	Position electron
y	Number	Weighting factor Raman cross sections

3 Photoluminescence setup

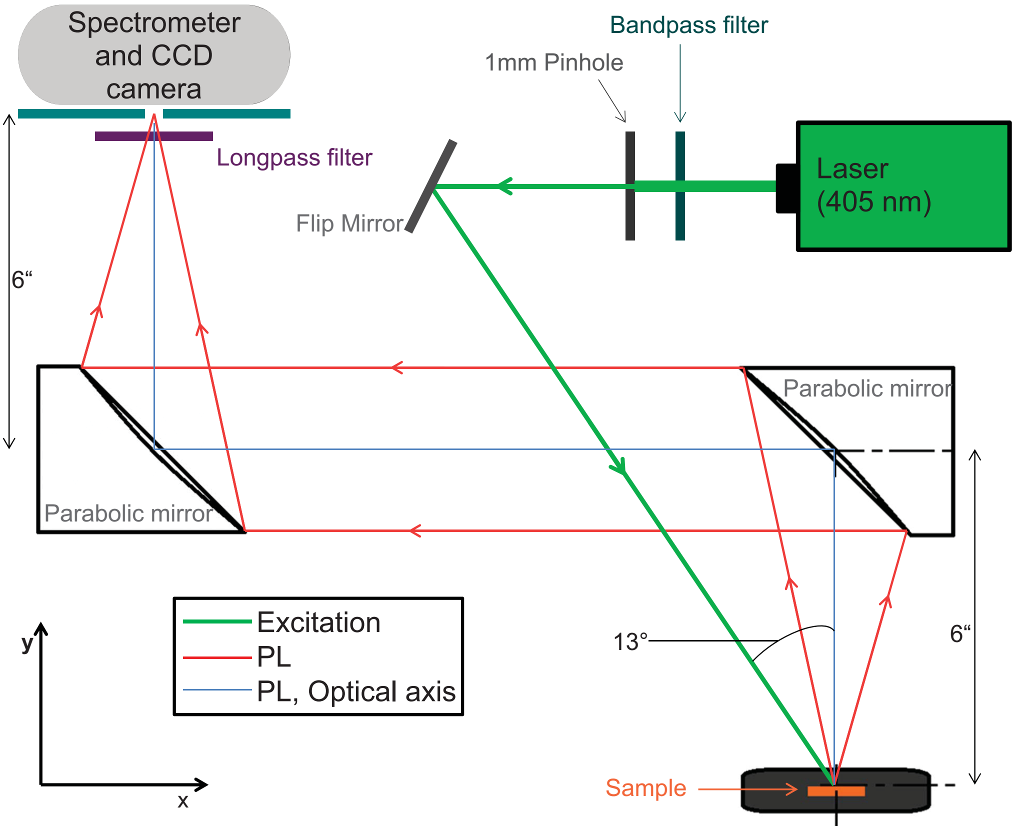

Figure 5: Sketch of the PL setup [58].

4 Structure factor F_{hkl} for Si and SiC

$$F_{hkl} = \sum_n f_n \exp[2\pi i(hx_n + ky_n + lz_n)] \tag{1}$$

where f_n are the atomic form factors of all atoms in one unit cell, whereas the exponential term takes into account the positions of these atoms within the unit cell (x_n, y_n, z_n) regarding the basis vectors $(\vec{a}, \vec{b}, \vec{c})$. We can calculate F_{hkl} for 3C-SiC (zinc blende structure) with the atomic form factors f_{Si} and f_{C}. Regarding the basis, the Si atoms are located at the positions (0,0,0), $(0,\frac{1}{2},\frac{1}{2})$, $(\frac{1}{2},0,\frac{1}{2})$ and $(\frac{1}{2},\frac{1}{2},0)$, while the C atoms are located at the positions $(\frac{1}{4},\frac{1}{4},\frac{1}{4})$, $(\frac{1}{4},\frac{3}{4},\frac{3}{4})$, $(\frac{3}{4},\frac{1}{4},\frac{3}{4})$ and $(\frac{3}{4},\frac{3}{4},\frac{1}{4})$.

$$\begin{aligned}
F_{hkl} &= f_{\text{Si}}(1 + e^{i\pi(k+l)} + e^{i\pi(h+l)} + e^{i\pi(h+k)}) \\
&\quad + f_{\text{C}}(e^{i\frac{\pi}{2}(h+k+l)} + e^{i\frac{\pi}{2}(h+3k+3l)} + e^{i\frac{\pi}{2}(3h+k+3l)} + e^{i\frac{\pi}{2}(3h+3k+l)}) \\
&= (f_{\text{Si}} + f_{\text{C}}e^{i\frac{\pi}{2}(h+k+l)})(1 + e^{i\pi(k+l)} + e^{i\pi(h+l)} + e^{i\pi(h+k)}) \\
&= \begin{cases} 4(f_{\text{Si}} \pm f_{\text{C}}e^{i\frac{\pi}{2}(h+k+l)}) & \text{h,k,l all even or all odd} \\ 0 & \text{otherwise} \end{cases}
\end{aligned} \tag{2}$$

In crystalline Si, there is only one sort of atoms and therefore only one atomic form factor f_{Si}, while the positions of the atoms in the unit cell are the same as in SiC (Si crystallizes in the diamond structure). This leads to the additional condition for a not vanishing F_{hkl} in the case of even (hkl): $h + k + l = 4n$ with n being a positive integer.

5 X-rays spectrum

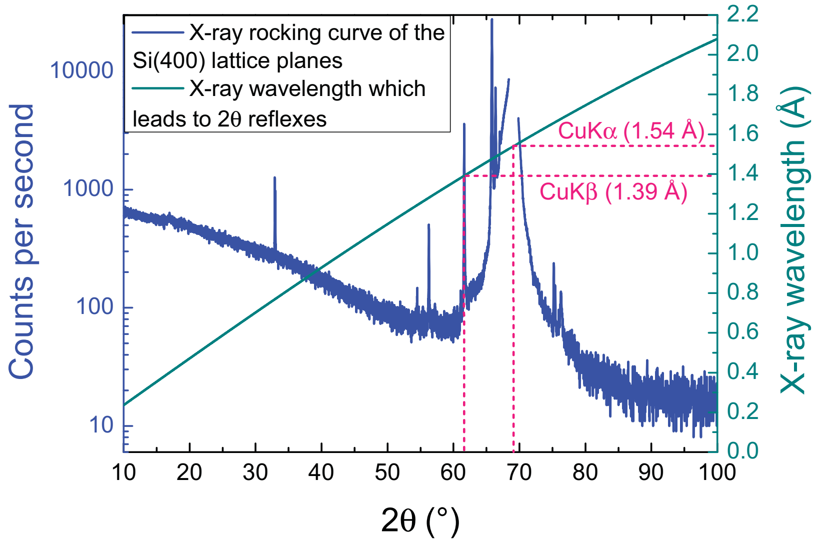

Figure 6: The X-ray spectrum hitting the samples in GIXRD configuration was determined indirectly by conducting an X-ray rocking curve measurement of the Si substrate. Therefore, the Si(400) lattice planes were chosen. Every reflex which occurs in the pattern (left-hand ordinate) can be "translated" to an X-ray wavelength (right-hand ordinate) via the Bragg equation (Eq. 3.3). The pattern shows residues of the bremsstrahlung at lower angles, a broad main reflex at 69.1°, resulting from the CuK$_\alpha$ line ($\lambda_{\mathrm{CuK}_\beta} = 1.54\,\mathrm{Å}$), a reflex at 61.6°, resulting from the CuK$_\beta$ line ($\lambda_{\mathrm{CuK}_\beta} = 1.39\,\mathrm{Å}$), and various foreign lines. The high intensity part of the 69.1° reflex was skipped during the measurement to avoid the use of an attenuator.

6 Further characterization methods

The following characterization methods were applied in this work without focusing on their further improvement:

- **Secondary ion mass spectroscopy** (SIMS)
  SIMS measurements were conduced by *RTG Mikroanalyse GmbH Berlin* in order to determine the N_2 contamination of the $Si_xC_{1\text{-}x}$ samples.

- **Spectral ellipsometry** (SE)
  The as-deposited layer thickness of the $Si_xC_{1\text{-}x}$ samples were determines by SE with a *Woollam M-2000* instrument. The data were fitted by a Cody-Lorentz oscillator model [163]. In the upcoming master thesis of J. Hofmann, a extended model will be presented to evaluate SE measurements for both, as-deposited and annealed $Si_xC_{1\text{-}x}$ samples.

- **Scanning electron microscopy** (SEM)
  SEM measurements of cross sections of annealed $Si_xC_{1\text{-}x}$ samples were conducted by J. Zielonka in order to determine the layer thickness. SEM images were acquired using a *Hitachi SU70* or a *Zeiss AURIGA 60 FIB-SEM* tool, both equipped with a Schottky emitter, operated at 5 kV accelerating voltage and a working distance of approximately 5 mm

- **Energy dispersive X-ray spectroscopy** (EDX)
  With EDX measurements, also conducted by J. Zielonka, the presence of large Si precipitations was proven in some $Si_xC_{1\text{-}x}$ samples. For EDX measurements, the *Zeiss FIB-SEM* is equipped with a *Bruker QUANTA 400* operated at an acceleration voltage of 5 kV.

- **Optical emission spectroscopy** (OES)
  OES allows the investigation of the ions present in the plasma during PECVD deposition.

7 Activation energy $Si_{0.77}C_{0.23}$

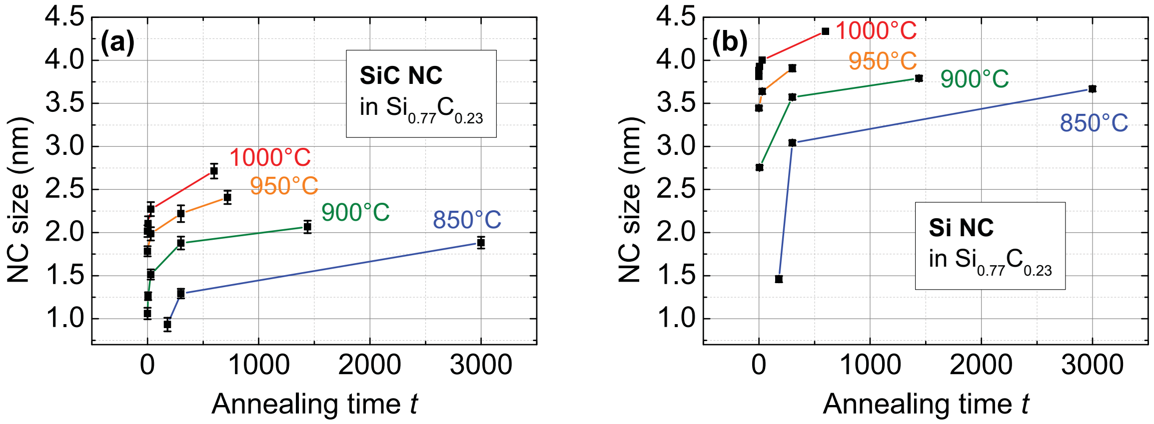

Figure 7: SiC (a) and Si (b) NC sizes from $Si_{0.77}C_{0.23}$ samples annealed at different temperatures, derived from GIXRD patterns.

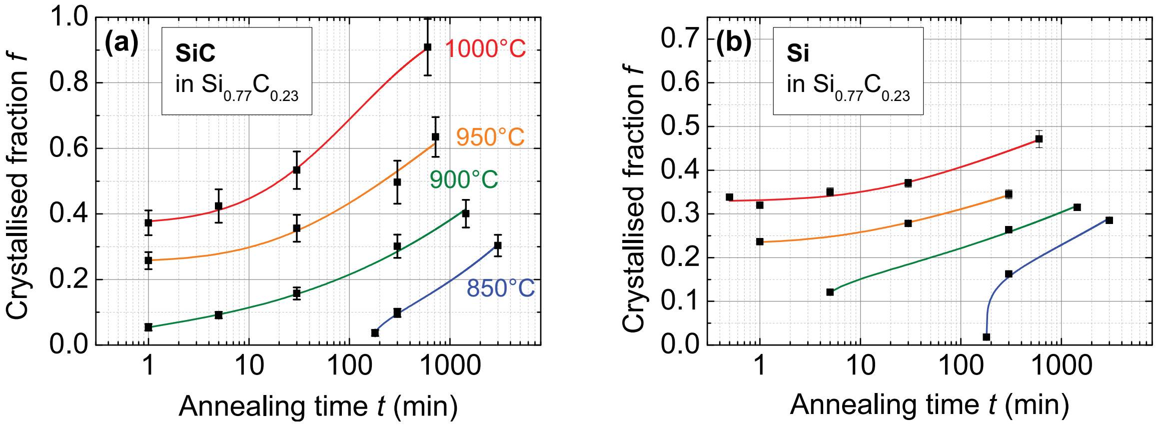

Figure 8: Developement of crystallised SiC (a) and Si (b) fractions f in $Si_{0.77}C_{0.23}$ samples with annealing time for four different annealing temperatures.

8 Table of thermal properties

Table 2: Literature values for the determination of the thermal diffusivity ζ and the thermal diffusion length L_D in Si and SiC.

Material	T	k (W/cm·K)	c_p (J/g·K)	δ g/cm^3	Ref.	$\zeta = k/\delta \cdot c_p$ (cm^2/s)	$L_D = \sqrt{\zeta t}$ (μm) for $t = 20$ ms	$t = L_D^2/\zeta$ (ms) for $L_D = 200$ nm
a-Si	27°C	0.007	0.77	2.30	[72]	0.0040	89	0.1012
	1000°C	0.011	1.07	2.30	[72]	0.0045	95	0.0895
	1145°C	0.013	1.12	2.30	[72]	0.0050	100	0.0793
c-Si	27°C	1.56	0.71	2.33	[72]	0.9430	1373	0.0004
	1000°C	0.25	0.96	2.30	[72]	0.1132	476	0.0035
	1414°C	0.22	1.03	2.29	[139]	0.0933	432	0.0043
a-SiC:H	27°C			1.51 - 2.15	[164]			
a-SiC	27°C	1.3 - 1.6			[73]			
poly-SiC (with additives)	27°C	0.48	0.7		[75]			
	1000°C	0.27	1.2*		[75]			
	1500°C	0.18*			[75]			
c-SiC	27°C	5.0	0.67	3.217*	[61, 74, 146]			
	730°C		1.18		[146]			
	1230°C		1.23		[146]			

9 Photoluminescence spectrum of a-Si$_{0.63}$C$_{0.37}$:H

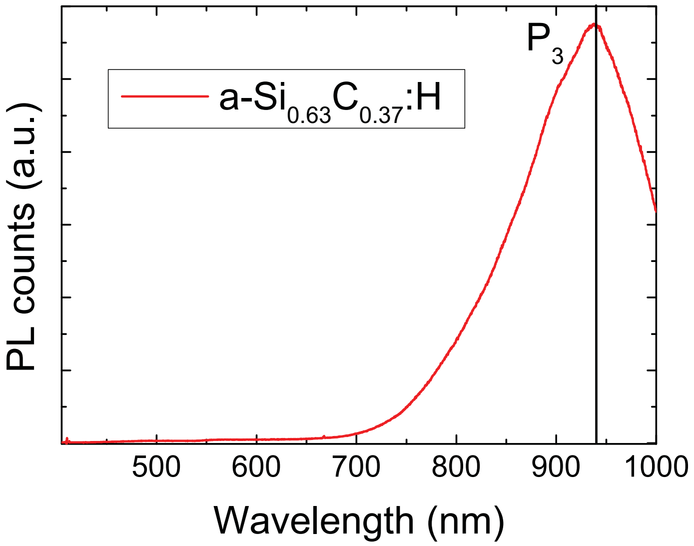

Figure 9: The PL spectrum of an a-Si$_{0.63}$C$_{0.37}$:H sample shows a peak around 940 nm (P$_3$).

Bibliography

[1] *Adoption of the Paris agreement, Article 2.1 (a).* UNFCCC, Paris (2015).

[2] C.-F. Schleussner, J. Rogelj, M. Schaeffer, T. Lissner, R. Licker, E. M. Fischer, R. Knutti, A. Levermann, K. Frieler, and W. Hare. Science and policy characteristics of the Paris Agreement temperature goal. In: *Nature Clim. Change* **6** (9), pp. 827 (2016).

[3] C.-F. Schleussner, J. F. Donges, R. V. Donner, and H. J. Schellnhuber. Armed-conflict risks enhanced by climate-related disasters in ethnically fractionalized countries. In: *Proceedings of the National Academy of Sciences* **113** (33), pp. 9216 (2016).

[4] C. P. Kelley, S. Mohtadi, M. A. Cane, R. Seager, and Y. Kushnir. Climate change in the Fertile Crescent and implications of the recent Syrian drought. In: *Proceedings of the National Academy of Sciences* **112** (11), pp. 3241 (2015).

[5] C. Werrell, F. Femia, and T. Sternberg. Did We See It Coming?: State Fragility, Climate Vulnerability, and the Uprisings in Syria and Egypt. In: *SAIS Review of International Affairs* **35** (1), pp. 29 (2015).

[6] J.-F. Maystadt and O. Ecker. Extreme Weather and Civil War: Does Drought Fuel Conflict in Somalia through Livestock Price Shocks? In: *American Journal of Agricultural Economics* **96** (4), pp. 1157 (2014).

[7] O. Edenhofer. King Coal and the queen of subsidies. In: *Science* **349** (6254), pp. 1286 (2015).

[8] P. van Breevoort, K. Blok, M. Hagemann, H. Fekete, N. Höhne, B. Hare, M. Schaeffer, M. Rocha, and L. Jeffery. The Coal Gap: Planned coal-fired power plants inconsistent with 2°C and threaten achievement of INDCs. In: *Climate Action Tracker* (2015).

[9] A. Richter, M. Hermle, and S. W. Glunz. Reassessment of the Limiting Efficiency for Crystalline Silicon Solar Cells. In: *Photovoltaics, IEEE Journal of Photovoltaics* **3** (4), pp. 1184 (2013).

[10] M. A. Green. *Third generation photovoltaics: Advanced solar energy conversion*, volume 12 of *Springer Series in Photonics*. Springer, Berlin, Heidelberg, New York (2003).

[11] P. Würfel. Neue Solarzellenkonzepte. In: *ForschungsVerbund Sonnenenergie* pp. 102–6 (2003).

[12] S. W. Glunz, R. Preu, and D. Biro. *Crystalline silicon solar cells: State-of-the-art and future developments*, volume 1, pp. 353–87. Elsevier, Oxford (2012).

[13] P. Würfel. *Physics of solar cells: From principles to new concepts.* Wiley-VCH Verlag GmbH and Co KgaA, Weinheim, Germany (2005).

[14] M. A. Green, K. Emery, Y. Hishikawa, W. Warta, and E. D. Dunlop. Solar cell efficiency tables (version 47). In: *Progress in Photovoltaics: Research and Applications* **24** (1), pp. 3 (2016).

[15] A. W. Bett, F. Dimroth, W. Guter, R. Hoheisel, E. Oliva, S. P. Philipps, J. Schöne, G. Siefer, M. Steiner, A. Wekkeli, E. Welser, M. Meusel, W. Köstler, and G. Strobl. Highest efficiency multi-junction solar cell for terrestrial and space applications. In: *Proceedings of the 24th European Photovoltaic Solar Energy Conference*, pp. 1–6 (2009).

[16] N. Wyrsch, A. Billet, G. Bugnon, M. Despeisse, A. Feltrin, F. Meillaud, G. Parascandolo, and C. Ballif. Development of micromorph cells in large-area industrial reactor. In: *Proceedings of the 24th European Photovoltaic Solar Energy Conference*, pp. 2808–11 (2009).

[17] K. Yamamoto, A. Nakajima, M. Yoshimi, T. Sawada, S. Fukuda, T. Suezaki, M. Ichikawa, Y. Kol, M. Goto, T. Meguro, T. Matsuda, T. Sasaki, and Y. Tawada. High efficiency thin film silicon hybrid cell and module with newly developed innovative interlayer. In: *Proceedings of the 4th World Conference on Photovoltaic Energy Conversion*, pp. 1489–92 (2006).

[18] R. A. Street. *Hydrogenated amorphous silicon.* Cambridge University Press, Cambridge, New York (2005).

[19] F. Meillaud, A. Shah, C. Droz, E. Vallat-Sauvain, and C. Miazza. Efficiency limits for single-junction and tandem solar cells. In: *Solar Energy Materials and Solar Cells* **90** (18-19), pp. 2952 (2006).

[20] G. Conibeer, M. Green, R. Corkish, Y. Cho, E.-C. Cho, C. W. Jiang, T. Fangsuwannarak, E. Pink, Y. Huang, T. Puzzer, T. Trupke, B. Richards, A. Shalav, and K. L. Lin. Silicon nanostructures for third generation photovoltaic solar cells. In: *Thin Solid Films* **511-2**, pp. 654 (2006).

[21] A. M. Hartel, S. Gutsch, D. Hiller, and M. Zacharias. Fundamental temperature-dependent properties of the Si nanocrystal band gap. In: *Physical Review B* **85** (16), p. 165306 (2012).

[22] A. M. Hartel, S. Gutsch, D. Hiller, and M. Zacharias. Intrinsic nonradiative recombination in ensembles of silicon nanocrystals. In: *Physical Review B* **87** (3), p. 035428 (2013).

[23] C.-W. Jiang and M. Green. Silicon quantum dot superlattices: Modeling of energy bands, densities of states, and mobilities for silicon tandem solar cell applications. In: *Journal of Applied Physics* **99**, p. 114902 (2006).

[24] S. Janz, P. Löper, and M. Schnabel. Silicon nanocrystals produced by solid phase crystallisation of superlattices for photovoltaic applications. In: *Materials Science and Engineering B* **178** (9), pp. 542 (2013).

[25] S. Janz, P. Löper, and M. Schnabel. *Prototype PV cells with Si nanoclusters.* Pan Stanford Publishing, CRC Press LLC, Boca Raton, FL (2015).

[26] M. Schnabel, C. Weiss, P. Löper, P. R. Wilshaw, and S. Janz. Self-assembled silicon nanocrystal arrays for photovoltaics. In: *physica status solidi (a)* **212** (8), pp. 1649 (2015).

[27] P. Löper, R. Müller, D. Hiller, T. Barthel, E. Malguth, S. Janz, J. C. Goldschmidt, M. Hermle, and M. Zacharias. Quasi-Fermi-level splitting in ideal silicon nanocrystal superlattices. In: *Physical Review B* **84**, p. 195317 (2011).

[28] M. Schnabel, M. Canino, K. Schillinger, P. Löper, C. Summonte, P. R. Wilshaw, and S. Janz. Monolithic Si nanocrystal/crystalline Si tandem cells involving Si nanocrystals in SiC. In: *Progress in Photovoltaics: Research and Applications* pp. 1165–1177 (2016).

[29] C. Summonte, M. Allegrezza, M. Bellettato, F. Liscio, M. Canino, A. Desalvo, J. López-Vidrier, S. Hernández, L. López-Conesa, S. Estradé, F. Peiró, B. Garrido, P. Löper, M. Schnabel, S. Janz, R. Guerra, and S. Ossicini. Silicon nanocrystals in carbide matrix. In: *Solar Energy Materials and Solar Cells* **128**, pp. 138 (2014).

[30] K. Ding, U. Aeberhard, W. Beyer, O. Astakhov, F. Köhler, U. Breuer, F. Finger, R. Carius, and U. Rau. Annealing induced defects in SiC, SiO_x single layers, and SiC/SiO_x hetero-superlattices. In: *physica status solidi (a)* pp. 1960–1964 (2012).

[31] Y. Kurokawa, S. Miyajima, A. Yamada, and M. Konagai. Preparation of nanocrystalline silicon in amorphous silicon carbide matrix. In: *Japanese Journal of Applied Physics* **45**, pp. 1064 (2006).

[32] M. A. Ouadfel, A. Keffous, A. Brighet, N. Gabouze, T. Hadjersi, A. Cheriet, M. Kechouane, A. Boukezzata, Y. Boukennous, Y. Belkacem, and H. Menari. Si-rich a-$Si_{1-x}C_x$ thin films by d.c. magnetron co-sputtering of silicon and silicon carbide: Structural and optical properties. In: *Applied Surface Science* **265**, pp. 94 (2013).

[33] D. Song, E.-C. Cho, G. Conibeer, Y. Huang, C. Flynn, and M. A. Green. Structural characterization of annealed $Si_{1-x}C_x/SiC$ multilayers targeting formation of Si nanocrystals in a SiC matrix. In: *Journal of Applied Physics* **103**, p. 083544 (2008).

[34] M. Zacharias, J. Heitmann, R. Scholz, U. Kahler, M. Schmidt, and J. Bläsing. Size-controlled highly luminescent silicon nanocrystals: A SiO/SiO_2 superlattice approach. In: *Applied Physics Letters* **80**, pp. 661 (2002).

[35] Z. Y. Wan, S. J. Huang, M. A. Green, and G. Conibeer. Rapid thermal annealing and crystallization mechanisms study of silicon nanocrystal in silicon carbide matrix. In: *Nanoscale Research Letters* **6** (129), pp. 1 (2011).

[36] Y. Zeng, X. Chen, Q. Cheng, J. Zhao, W. Song, and N. Dai. Thermodynamics of the formation of face-centered-cubic silicon nanocrystals in silicon-rich SiC thin films annealed using rapid thermal annealing. In: *Applied Surface Science* **265**, pp. 286 (2013).

[37] X. Chen and P. Yang. Preparation and photovoltaic properties of silicon quantum dots embedded in a dielectric matrix: A review. In: *Journal of Materials Science: Materials in Electronics* pp. 1–14 (2015).

[38] M. Künle, S. Janz, O. Eibl, C. Berthold, V. Presser, and K.-G. Nickel. Thermal annealing of SiC thin films with varying stoichiometry. In: *Materials Science and Engineering B* **159-160**, pp. 355 (2009).

[39] M. Künle, T. Kaltenbach, P. Löper, A. Hartel, S. Janz, O. Eibl, and K.-G. Nickel. Si-rich a-SiC:H thin films: Structural and optical transformations during thermal annealing. In: *Thin Solid Films* **519** (1), pp. 151 (2010).

[40] M. Zacharias, J. Bläsing, P. Veit, L. Tsybeskov, K. Hirschman, and P. M. Fauchet. Thermal crystallization of amorphous Si/SiO_2 superlattices. In: *Applied Physics Letters* **74** (18), pp. 2614 (1999).

[41] S. Mirabella, R. Agosta, G. Franzò, I. Crupi, M. Miritello, R. Lo Savio, M. A. Di Stefano, S. Di Marco, F. Simone, and A. Terrasi. Light absorption in silicon quantum dots embedded in silica. In: *Journal of Applied Physics* **106**, p. 103505 (2009).

[42] M. Künle, S. Janz, K. G. Nickel, A. Heidt, M. Luysberg, and O. Eibl. Annealing of nm-thin $Si_{1-x}C_x$/SiC multilayers. In: *Solar Energy Materials and Solar Cells* **115**, pp. 11 (2013).

[43] J. López-Vidrier, S. Hernández, J. Samà, M. Canino, M. Allegrezza, M. Bellettato, R. Shukla, M. Schnabel, P. Löper, L. López-Conesa, S. Estradé, F. Peiró, S. Janz, and B. Garrido. Structural, optical and electrical properties of silicon nanocrystals embedded in Si_xC_{1-x}/SiC multilayer systems for photovoltaic applications. In: *Materials Science and Engineering B* **178**, pp. 639 (2013).

[44] C. Weiss, M. Rumpel, M. Schnabel, P. Löper, and S. Janz. Novel Silicon Nanocrystal Materials for Photovoltaic Applications. In: *Proceedings of the 28th European PV Solar Energy Conference and Exhibition* (2013).

[45] C. Weiss, M. Schnabel, A. Reichert, P. Löper, and S. Janz. Structural and optical properties of silicon nanocrystals embedded in silicon carbide: Comparison of single layers and multilayer structures. In: *Applied Surface Science* **351**, pp. 550 (2015).

[46] R. Gradmann, P. Loeper, M. Künle, M. Rothfelder, S. Janz, M. Hermle, and S. Glunz. Si and SiC nanocrystals in an amorphous SiC matrix: Formation and electrical properties. In: *Physica Status Solidi C* **8**, pp. 831 (2011).

[47] C. Summonte, S. Mirabella, R. Balboni, A. Desalvo, I. Crupi, F. Simone, and A. Terrasi. Growth and characterization of Si nanodot multilayers in SiC matrix. In: *Proceedings of the 23rd European Photovoltaic Solar Energy Conference*, pp. 730–3 (2008).

[48] C. Summonte, E. Centurioni, M. Canino, M. Allegrezza, A. Desalvo, A. Terrasi, S. Mirabella, S. Di Marco, M. A. Di Stefano, M. Miritello, R. Lo Savio, F. Simone, and R. Agosta. Optical properties of silicon rich oxides. In: *Physica Status Solidi C* **8**, pp. 996 (2011).

[49] Y. Kurokawa, S. Yamada, S. Miyajima, A. Yamada, and M. Konagai. Effects of oxygen addition on electrical properties of silicon quantum dots/amorphous silicon carbide superlattice. In: *Current Applied Physics* **10**, pp. 435 (2010).

[50] Y. Kurokawa, S. Tomita, S. Miyajima, A. Yamada, and M. Konagai. Effects of nitrogen on the electrical properties of Si quantum dots superlattice using a-SiC matrix. In: *Proceedings of the 24th European Photovoltaic Solar Energy Conference*, pp. 398–403 (2009).

[51] S. Godefroo, M. Hayne, M. Jivanescu, A. Stesmans, M. Zacharias, O. I. Lebedev, G. Van Tendeloo, and V. V. Moshchalkov. Classification and control of the origin of photoluminescence from Si nanocrystals. In: *Nature Nanotechnology* **3**, pp. 174 (2008).

[52] M. Jivanescu, A. Stesmans, and M. Zacharias. Inherent paramagnetic defects in layered Si/SiO_2 superstructures with Si nanocrystals. In: *Journal of Applied Physics* **104** (10), p. 103518 (2008).

[53] K. Ding, U. Aeberhard, O. Astakhov, U. Breuer, M. Beigmohamadi, S. Suckow, B. Berghoff, W. Beyer, F. Finger, R. Carius, and U. Rau. Defect passivation by hydrogen reincorporation for silicon quantum dots in SiC/SiO_x hetero-superlattice. In: *Journal of Non-Crystalline Solids* pp. 2145–2149 (2012).

[54] S. Yamada, Y. Kurokawa, S. Miyajima, and M. Konagai. Investigation of hydrogen plasma treatment for reducing defects in silicon quantum dot superlattice structure with amorphous silicon carbide matrix. In: *Nanoscale Research Letters* **9** (1), pp. 1 (2014).

[55] Y. Kurokawa, S. Tomita, S. Miyajima, A. Yamada, and M. Konagai. Effects of rehydrogenation on silicon quantum dots superlattice. In: *Proceedings of the 22nd European Photovoltaic Solar Energy Conference*, pp. 233–6 (2007).

[56] M. T. Künle. *Silicon carbide single and multilayer thin films for photovoltaic applications.* Dissertation, Eberhard-Karls-Universität Tübingen (2011).

[57] P. Löper. *Silicon Nanostructures for Photovoltaics.* Dissertation, Albert-Ludwigs-Universität Freiburg (2013).

[58] M. Schnabel. *Silicon Nanocrystals Embedded in Silicon Carbide for Tandem Solar Cell Applications.* Ph.d. thesis, University of Oxford (2015).

[59] J. Davies. *The physics of low-dimensional semiconductors.* Cambridge University Press, Cambridge, New York (1998).

[60] M. Levinshtein, S. Rumyantsev, and M. Shur. *Properties of Advanced SemiconductorMaterials GaN, AlN, SiC, BN, SiC, SiGe.* John Wiley & Sons, New York (2001).

[61] W. Wesch. Silicon carbide: Synthesis and processing. In: *Nuclear Instruments and Methods in Physics Research Section B: Beam Interactions with Materials and Atoms* **116** (1-4), pp. 305 (1996).

[62] G. L. Harris. *Properties of silicon carbide.* INSPEC, the Institution of Electrical Engineers, London, UK (1995).

[63] R. H. Klazes, M. H. L. M. van den Broek, J. Bezemer, and S. Radelaar. Determination of the optical bandgap of amorphous silicon. In: *Philosophical Magazine Part B* **45** (4), pp. 377 (1982).

[64] K. Mui, D. K. Basa, F. W. Smith, and R. Corderman. Optical constants of a series of amorphous hydrogenated silicon-carbon alloy films: Dependence of optical response on film microstructure and evidence for homogeneous chemical ordering. In: *Physical Review B* **35** (15), pp. 8089 (1987).

[65] R. Hull. *Properties of crystalline silicon.* EMIS datareviews series. INSPEC, the Institution of Electrical Engineers, London (1999).

[66] E. P. Donovan, F. Spaepen, D. Turnbull, J. M. Poate, and D. C. Jacobson. Heat of crystallization and melting point of amorphous silicon. In: *Applied Physics Letters* **42** (8), pp. 698 (1983).

[67] R. W. Olesinski and G. J. Abbaschian. The C-Si (Carbon-Silicon) system. In: *Bulletin of Alloy Phase Diagrams* **5** (5), pp. 486 (1984).

[68] S. W. King, J. Bielefeld, M. French, and W. A. Lanford. Mass and bond density measurements for PECVD a-SiC$_x$:H thin films using Fourier transform-infrared spectroscopy. In: *Journal of Non-Crystalline Solids* **357**, pp. 3602 (2011).

[69] H. R. Philipp and E. A. Taft. Optical constants of silicon in the region 1 to 10 eV. In: *Physical Review* **120** (1), pp. 37 (1960).

[70] R. Swanepoel. Determination of the thickness and optical constants of amorphous silicon. In: *Journal of Physics E: Scientific Instruments* **16** (12), pp. 1214 (1983).

[71] E. R. Shaaban, T. Lohner, P. Petrik, N. Q. Khánh, M. Fried, O. Polgár, and J. Gyulai. Determination of the complex dielectric function of ion implanted amorphous SiC by spectroscopic ellipsometry. In: *physica status solidi (a)* **195** (1), pp. 277 (2003).

[72] M. Smith, R. McMahon, M. Voelskow, D. Panknin, and W. Skorupa. Modelling of flash-lamp-induced crystallization of amorphous silicon thin films on glass. In: *Journal of Crystal Growth* **285** (1-2), pp. 249 (2005).

[73] P. M. Sarro. Silicon carbide as a new MEMS technology. In: *Sensors and Actuators A: Physical* **82** (1-3), pp. 210 (2000).

[74] P. Patnaik. *Handbook of inorganic chemicals.* McGraw-Hill (2003).

[75] R. A. Verrall, M. D. Vlajic, and V. D. Krstic. Silicon carbide as an inert-matrix for a thermal reactor fuel. In: *Journal of Nuclear Materials* **274** (1-2), pp. 54 (1999).

[76] J. Robertson. The electronic and atomic structure of hydrogenated amorphous Si-C alloys. In: *Philosophical Magazine Part B* **66** (5), pp. 615 (1992).

[77] W. C. O'Mara, R. B. Herring, and L. P. Hunt. *Handbook of semiconductor silicon technology.* Noyes, Park Ridge, NJ, USA (1990).

[78] A. Matsuda. Growth mechanism of microcrystalline silicon obtained from reactive plasmas. In: *Thin Solid Films* **337** (1-2), pp. 1 (1999).

[79] L. Calcagno, P. Musumeci, F. Roccaforte, C. Bongiorno, and G. Foti. Crystallisation mechanism of amorphous silicon carbide. In: *Applied Surface Science* **184** (1), pp. 123 (2001).

[80] S. Kühnapfel, D. Amkreutz, C. Klimm, and N. H. Nickel. Excimer laser crystallization of a-SiC$_x$ on glass. In: *Canadian Journal of Physics* **92** (7/8), pp. 709 (2014).

[81] M. G. Grimaldi, P. Baeri, M. A. Malvezzi, and C. Sirtori. Thermodynamic properties of amorphous silicon investigated by pulsed laser heating. In: *International Journal of Thermophysics* **13** (1), pp. 141 (1992).

[82] M. Ishimaru, I.-T. Bae, Y. Hirotsu, S. Matsumura, and K. E. Sickafus. Structrual relaxation of amorphous silicon carbide. In: *Physical Review Letters* **89** (5), p. 055502 (2002).

[83] L. L. Snead and S. J. Zinkle. Structural relaxation in amorphous silicon carbide. In: *Nuclear Instruments and Methods in Physics Research B* **191**, pp. 497 (2002).

[84] G. Ambrosone, U. Coscia, S. Lettieri, P. Maddalena, C. Minarini, V. Parisi, and S. Schutzmann. Crystallization of hydrogenated amorphous silicon-carbon films by means of laser treatments. In: *Applied Surface Science* **247** (1-4), pp. 471 (2005).

[85] J. Barbé, L. Xie, K. Leifer, P. Faucherand, C. Morin, D. Rapisarda, E. De Vito, K. Makasheva, B. Despax, and S. Perraud. Silicon nanocrystals on amorphous silicon carbide alloy thin films: Control of film properties and nanocrystals growth. In: *Thin Solid Films* **522** (0), pp. 136 (2012).

[86] S. W. King, M. French, J. Bielefeld, and W. A. Lanford. Fourier transform infrared spectroscopy investigation of chemical bonding in low-k a-SiC:H thin films. In: *Journal of Non-Crystalline Solids* **357**, pp. 2970 (2011).

[87] K. Meyer. *Physikalisch-chemische Kristallographie*, volume 2. VEB Deutscher Verlag für Grundstoffindustrie 368, Leipzig (1977).

[88] C. Spinella, S. Lombardo, and F. Priolo. Crystal grain nucleation in amorphous silicon. In: *Journal of Applied Physics* **84** (10), pp. 5383 (1998).

[89] F. Liu, F. Sommer, C. Bos, and E. J. Mittemeijer. Analysis of solid state phase transformation kinetics: models and recipes. In: *International Materials Reviews* **52** (4), pp. 193 (2007).

[90] P. Giffard. *Ostwald Ripening*. Tort (2011).

[91] I. M. Lifshitz and V. V. Slyozov. The kinetics of precipitation from supersaturated solid solutions. In: *Journal of Physics and Chemistry of Solids* **19** (1-2), pp. 35 (1961).

[92] N. Soltani, E. Saion, M. Erfani, K. Rezaee, G. Bahmanrokh, G. P. C. Drummen, A. Bahrami, and M. Z. Hussein. Influence of the Polyvinyl Pyrrolidone Concentration on Particle Size and Dispersion of ZnS Nanoparticles Synthesized by Microwave Irradiation. In: *International Journal of Molecular Sciences* **13** (10), p. 12412 (2012).

[93] E. V. Shevchenko, D. V. Talapin, H. Schnablegger, A. Kornowski, O. Festin, P. Svedlindh, M. Haase, and H. Weller. Study of Nucleation and Growth in the Organometallic Synthesis of Magnetic Alloy Nanocrystals: The Role of Nucleation Rate in Size Control of $CoPt_3$ Nanocrystals. In: *Journal of the American Chemical Society* **125** (30), pp. 9090 (2003).

[94] G. L. Olson and J. A. Roth. Kinetics of solid phase crystallization in amorphous silicon. In: *Materials Science Reports* **3** (1), pp. 1 (1988).

[95] I. Wu, A. Chiang, M. Fuse, L. Öveçoglu, and T. Y. Huang. Retardation of nucleation rate for grain size enhancement by deep silicon ion implantation of low-pressure chemical vapor deposited amorphous silicon films. In: *Journal of Applied Physics* **65** (10), pp. 4036 (1989).

[96] S. Inoue, K. Yoshii, M. Umeno, and H. Kawabe. Crystallization behaviour of amorphous SiC films prepared by r.f. sputtering. In: *Thin Solid Films* **151** (3), pp. 403 (1987).

[97] D. Song, E.-C. Cho, G. Conibeer, Y.-H. Cho, and Y. Huang. Fabrication and characterization of Si nanocrystals in SiC matrix produced by magnetron cosputtering. In: *Journal of Vacuum Science Technology B* **25**, pp. 1327 (2007).

[98] M. Rumpel. *Festphasenkristallisation von Siliciumcarbid Mehrfachschichtsystemen.* Bachelor thesis, Julius-Maximilians-Universität Würzburg (2013).

[99] A. Reichert. *Kristallisationsprozess von Silicium-Nanokristallen in einer Siliciumcarbid-Matrix.* Master thesis, Albert-Ludwigs-Universität Freiburg (2015).

[100] T. Fehrenbach. *Züchtung von Silicium-Nanokristallen durch Festphasen-Kristallisation einer amorphen* Si_xC_{1-x}*:H-Schicht.* Bachelor thesis, Albert-Ludwigs-Universität Freiburg (2016).

[101] S. Reber, W. Zimmermann, and T. Kieliba. Zone melting recrystallization of silicon films for crystalline silicon thin-film solar cells. In: *Solar Energy Materials & Solar Cells* **65**, pp. 409 (2001).

[102] T. Kieliba. *Zone-melting recrystallization for crystalline silicon thin-film solar cells.* Ph.d. thesis, Universität Konstanz (2006).

[103] S. Prucnal, T. Shumann, W. Skorupa, B. Abendroth, K. Krockert, and H. Möller. Solar Cell Emitters Fabricated by Flash Lamp Millisecond Annealing. In: *Proceedings of the 8th International Conference Ion Implantation and Other Applications of Ions and Electrons*, volume 120, pp. 30–34 (2011).

[104] W. Skorupa, W. Anwand, D. Panknin, M. Voelskow, R. A. Yankov, and T. Gebel. Advanced thermal processing of semiconductor materials in the millisecond range. In: *Vacuum* **78** (2-4), pp. 673 (2005).

[105] D. Hiller, M. Jivanescu, A. Stesmans, and M. Zacharias. Pb(0) centers at the Si-nanocrystal/SiO_2 interface as the dominant photoluminescence quenching defect. In: *Journal of Applied Physics* **107**, p. 084309 (2010).

[106] A. V. Vasin, S. P. Kolesnik, A. A. Konchits, V. I. Kushnirenko, V. S. Lysenko, A. N. Nazarov, A. V. Rusavsky, and S. Ashok. Effects of hydrogen bond redistribution on photoluminescence of a-SiC:H films under thermal treatment. In: *Journal of Applied Physics* **99** (11), p. 113520 (2006).

[107] M. Schnabel, P. Löper, M. Canino, S. A. Dyakov, M. Allegrezza, M. Bellettato, J. López-Vidrier, S. Hernández, C. Summonte, B. Garrido, P. R. Wilshaw, and S. Janz. Electrical and optical characterisation of silicon nanocrystals embedded in SiC. In: *Solid State Phenomena* **205-6**, pp. 480 (2014).

[108] M. Schnabel, C. Summonte, S. A. Dyakov, M. Canino, L. López-Conesa, P. Löper, S. Janz, and P. R. Wilshaw. Absorption and emission of silicon nanocrystals embedded in SiC: Eliminating Fabry-Pérot interference. In: *Journal of Applied Physics* **117** (4), p. 045307 (2015).

[109] J. Tauc, R. Grigorovici, and A. Vancu. Optical properties and electronic structure of amorphous germanium. In: *Physica Status Solidi B* **15** (2), pp. 627 (1966).

[110] A. Guinier, P. Lorrain, D. Lorrain, and J. Gillis. *X-Ray Diffraction in Crystals, Imperfect Crystals, and Amorphous Bodies*, volume 17. W.H. Freeman, San Francisco, California (1964).

[111] H. Klug. X-Ray Diffraction Procedure for Polycrystalline and Amorphous Materials. In: *New York: John Wiley and Sons* (1974).

[112] R. Feynman, R. Leighton, and M. Sands. *The Feynman Lectures on Physics, Volume I.* Basic Books, New York (2013).

[113] H. Kuzmany. *Solid-State Spectroscopy.* Springer-Verlag, Heidelberg (2009).

[114] S. Peter, S. Bernütz, S. Berg, and F. Richter. FTIR analysis of a-SiC_N:H films deposited by PECVD. In: *Vacuum* **98**, pp. 81 (2013).

[115] H. Wieder, M. Cardona, and C. R. Guarnieri. Vibrational spectrum of hydrogenated amorphous Si-C films. In: *Physica Status Solidi B* **92** (99), pp. 99 (1979).

[116] D. R. McKenzie. Infrared absorption and bonding in amorphous hydrogenated silicon-carbon alloys. In: *Journal of Physics D: Applied Physics* **18** (9), pp. 1935 (1985).

[117] D. K. Basa and F. W. Smith. Annealing and crystallization processes in a hydrogenated amorphous Si-C alloy film. In: *Thin Solid Films* **192** (1), pp. 121 (1990).

[118] R. A. C. M. M. van Swaaij, A. J. M. Berntsen, W. G. J. H. M. van Sark, H. Herremans, J. Bezemer, and W. F. van der Weg. Local structure and bonding states in a-$Si_{1-x}C_x$:H. In: *Journal of Applied Physics* **76** (1), pp. 251 (1994).

[119] Y. Tawada, K. Tsuge, M. Kondo, H. Okamoto, and Y. Hamakawa. Properties and structure of a-SiC:H for high-efficiency a-Si solar cell. In: *Journal of Applied Physics* **53** (7), pp. 5273 (1982).

[120] M. Cardona. Vibrational Spectra of Hydrogen in Silicon and Germanium. In: *physica status solidi (b)* **118** (2), pp. 463 (1983).

[121] D. V. Tsu, G. Lucovsky, and M. J. Mantini. Local anatomic structure in thin films of silicon nitride and silicon diimide produced by remote plasma-enhanced chemical-vapor deposition. In: *Physical Review B* **33** (10), pp. 7069 (1986).

[122] F. Giorgis, F. Giuliani, C. F. Pirri, E. Tresso, C. Summonte, R. Rizzoli, R. Galloni, A. Desalvo, and P. Rava. Optical, structural and electrical properties of device-quality hydrogenated amorphous silicon-nitrogen films deposited by plasma-enhanced chemical vapour deposition. In: *Philosophical Magazine Part B* **77** (4), pp. 925 (1998).

[123] G. Lucovsky, M. J. Manitini, J. K. Srivastava, and E. A. Irene. Low-temperature growth of silicon dioxide films: A study of chemical bonding by ellipsometry and infrared spectroscopy. In: *Journal of Vacuum Science and Technology B* **5** (2), pp. 530 (1987).

[124] P. Musumeci, R. Reitano, L. Calcagno, F. Roccaforte, A. Makhtari, and M. G. Grimaldi. Relaxation and crystallization of amorphous silicon carbide probed by optical measurements. In: *Philosophical Magazine B* **76** (3), pp. 323 (1997).

[125] P. Musumeci, L. Calcagno, and A. Makhtari. Relaxation phenomena in keV-ion implanted hydrogenated amorphous silicon carbide. In: *Materials Science and Engineering: A* **253** (1,Äì2), pp. 296 (1998).

[126] L. Calcagno, P. Musumeci, F. Roccaforte, C. Bongiorno, and G. Foti. Crystallization process of amorphous silicon-carbon alloys. In: *Thin Solid Films* **411** (2), pp. 298 (2002).

[127] S. Kerdiles, A. Berthelot, F. Gourbilleau, and R. Rizk. Low temperature deposition of nanocrystalline silicon carbide thin films. In: *Applied Physics Letters* **76** (17), pp. 2373 (2000).

[128] P. Löper, D. Stüwe, M. Künle, M. Bivour, C. Reichel, R. Neubauer, M. Schnabel, M. Hermle, O. Eibl, S. Janz, M. Zacharias, and S. W. Glunz. A membrane device for substrate-free photovoltaic characterization of quantum dot based p-i-n solar cells. In: *Advanced Materials* **24**, pp. 3124 (2012).

[129] H. Richter, Z. P. Wang, and L. Ley. The one phonon Raman spectrum in microcrystalline silicon. In: *Solid State Communications* **39** (5), pp. 625 (1981).

[130] R. Tsu, M. Izu, S. R. Ovshinsky, and F. H. Pollak. Electroreflectance and Raman scattering investigation of glow-discharge amorphous Si:F:H. In: *Solid State Communications* **36** (9), pp. 817 (1980).

[131] D. Bermejo and M. Cardona. Raman scattering in pure and hydrogenated amorphous germanium and silicon. In: *Journal of Non-Crystalline Solids* **32** (1-3), pp. 405 (1979).

[132] A. Morimoto, S. Oozora, M. Kumeda, and T. Shimizu. Raman studies on local structural disorder in silicon-based amorphous semiconductor films. In: *Solid State Communications* **47** (10), pp. 773 (1983).

[133] Z. Iqbal and S. Veprek. Raman scattering from hydrogenated microcrystalline and amorphous silicon. In: *Journal of Physics C: Solid State Physics* **15** (2), p. 377 (1982).

[134] C. Droz, E. Vallat-Sauvain, J. Bailat, L. Feitknecht, J. Meier, and A. Shah. Relationship between Raman crystallinity and open-circuit voltage in microcrystalline silicon solar cells. In: *Solar Energy Materials and Solar Cells* **81** (1), pp. 61 (2004).

[135] E. Vallat-Sauvain, C. Droz, F. Meillaud, J. Bailat, A. Shah, and C. Ballif. Determination of Raman emission cross-section ratio in hydrogenated microcrystalline silicon. In: *Journal of Non-Crystalline Solids* **352** (9), pp. 1200 (2006).

[136] E. Bustarret, M. Bensouda, M. C. Habrard, and J. C. Bruyere. Configurational statistics in a-$Si_xN_yH_z$ alloys: A quantitative bonding analysis. In: *Physical Review B* **38** (12), p. 8171 (1988).

[137] D. V. Tsu, B. S. Chao, S. R. Ovshinsky, S. Guha, and J. Yang. Effect of hydrogen dilution on the structure of amorphous silicon alloys. In: *Applied Physics Letters* **71** (10), pp. 1317 (1997).

[138] H. Touir, J. Dixmier, K. Zellama, J. F. Morhange, and P. Elkaim. Bimodal crystal size distribution in annealed r.f. magnetron silicon films: A memory effect of the local order inhomogeneities in the initial amorphous state. In: *Journal of Non-Crystalline Solids* **227-230** (Part 2), pp. 906 (1998).

[139] C. Smit, R. A. C. M. M. van Swaaij, H. Donker, A. M. H. N. Petit, W. M. M. Kessels, and M. C. M. van de Sanden. Determining the material structure of microcrystalline silicon from Raman spectra. In: *Journal of Applied Physics* **94** (5), pp. 3582 (2003).

[140] C. Weiss, M. Schnabel, S. Prucnal, J. Hofmann, A. Reichert, T. Fehrenbach, W. Skorupa, and S. Janz. Formation of silicon nanocrystals in silicon carbide using flash lamp annealing. In: *Journal of Applied Physics* **120** (10), p. 105103 (2016).

[141] D. Gracin, I. Bogdanović, V. Borjanović, M. Jakšić, Z. Pastuović, J. M. Dutta, B. Vlahović, and R. J. Nemanich. Quantitative analysis of a-$Si_{1-x}C_x$:H thin films by vibrational spectroscopy and nuclear methods. In: *Vacuum* **61** (2-4), pp. 303 (2001).

[142] A. Mattausch. *Ab initio-Theory of Point Defects and Defect Complexes in SiC*. Dissertation, Friedrich-Alexander-Universität Nürnberg (2005).

[143] S. Prucnal, J. M. Sun, A. Muecklich, and W. Skorupa. Flash Lamp Annealing vs Rapid Thermal and Furnace Annealing for Optimized Metal-Oxide-Silicon-Based Light-Emitting Diodes. In: *Electrochemical and Solid-State Letters* **10** (2), pp. 50 (2007).

[144] G. Lucovsky. Chemical effects on the frequencies of Si-H vibrations in amorphous solids. In: *Solid State Communications* **29** (8), pp. 571 (1979).

[145] E. Gat, M. El Khakani, M. Chaker, A. Jean, S. Boily, H. Pépin, J. Kieffer, J. Durand, B. Cros, F. Rousseaux, and S. Gujrathi. A study of the effect of composition on the microstructural evolution of a-Si_xC_{1-x}: H PECVD films: IR absorption and XPS characterizations. In: *Journal of Materials Research* **7** (09), pp. 2478 (1992).

[146] I. S. Grigoriev and E. Z. Meilikhov. *Handbook of physical quantities.* CRC Press LLC, Boca Raton, FL (1997).

[147] F. Lanckmans, B. Brijs, and K. Maex. The role of H in the Cu+ drift diffusion in plasma-deposited a-SiC:H. In: *Journal of Physics: Condensed Matter* **14** (13), p. 3565 (2002).

[148] K. Yoshii, Y. Suzaki, A. Takeuchi, K. Yasutake, and H. Kawabe. Crystallization behaviour of amorphous $Si_{1-x}C_x$ films prepared by r.f. sputtering. In: *Thin Solid Films* **199** (1), pp. 85 (1991).

[149] V. Cimalla, T. Wöhner, and J. Pezoldt. The Diffusion Coefficient of Silicon in Thin SiC Layers as a Criterion for the Quality of the Grown Layers. In: *Materials Science Forum* **338 - 342**, pp. 321 (2000).

[150] C. Summonte, A. Desalvo, M. Canino, M. Allegrezza, M. Rosa, M. Ferri, E. Centurioni, A. Terrasi, and S. Mirabella. Optical properties of silicon nanodots in SiC matrix. In: *Proceedings of the 25th European Photovoltaic Solar Energy Conference and Exhibition* (2010).

[151] H. Guenzler and H. M. Heise. *IR-Spektroskopie.* VCH Verlagsgesellschaft, Weinheim (1996).

[152] M. Di Ventra and S. T. Pantelides. Atomic-Scale Mechanisms of Oxygen Precipitation and Thin-Film Oxidation of SiC. In: *Physical Review Letters* **83** (8), pp. 1624 (1999).

[153] M. Kořínek, M. Schnabel, M. Canino, M. Kozák, F. Trojánek, J. Salava, P. Löper, S. Janz, C. Summonte, and P. Malý. Influence of boron doping and hydrogen passivation on recombination of photoexcited charge carriers in silicon nanocrystal/SiC multilayers. In: *Journal of Applied Physics* **114** (7), p. 073101 (2013).

[154] S. H. Baker, W. E. Spear, and R. A. G. Gibson. Electronic and optical properties of a-$Si_{1-x}C_x$ films prepared from a H_2-diluted mixture of SiH_4 and CH_4. In: *Philosophical Magazine Part B* **62** (2), pp. 213 (1990).

[155] M. Schnabel, M. Canino, S. Kühnhold-Pospischil, J. López-Vidrier, T. Klugermann, C. Weiss, L. López-Conesa, M. Zschintzsch-Dias, C. Summonte, P. Löper, S. Janz, and P. R. Wilshaw. Charge transport in nanocrystalline SiC with and without embedded Si nanocrystals. In: *Physical Review B* **91** (19), p. 195317 (2015).

[156] N. Ishii, M. Kumeda, and T. Shimizu. A simple molecular orbital calculation of ESR g-values for amorphous $Si_{1-x}C_x$, $Si_{1-x}Ge_x$ and $Ge_{1-x}C_x$. In: *Solid State Communications* **41** (2), pp. 143 (1982).

[157] T. Shimizu, M. Kumeda, and Y. Kiriyama. ESR studies on sputtered amorphous Si-C, Si-Ge and Ge-C films. In: *Solid State Communications* **37** (9), pp. 699 (1981).

[158] B. Sopori, M. I. Symko, R. Reedy, K. Jones, and R. Matson. Mechanism(s) of hydrogen diffusion in silicon solar cells during forming gas anneal. In: *Photovoltaic Specialists Conference, 1997., Conference Record of the Twenty-Sixth IEEE*, pp. 25–30 (1997).

[159] W. Beyer. Incorporation and thermal stability of hydrogen in amorphous silicon and germanium. In: *Journal of Non-Crystalline Solids* **198-200** (1), pp. 40 (1996).

[160] L. Pavesi and R. Turan. *Silicon nanocrystals: Fundamentals, synthesis and applications*. John Wiley & Sons (2010).

[161] M. V. Wolkin, J. Jorne, P. M. Fauchet, G. Allan, and C. Delerue. Electronic States and Luminescence in Porous Silicon Quantum Dots: The Role of Oxygen. In: *Physical Review Letters* **82** (1), pp. 197 (1999).

[162] S. Furukawa and T. Miyasato. Quantum size effects on the optical band gap of microcrystalline Si:H. In: *Physical Review B* **38** (8), pp. 5726 (1988).

[163] M. Rothfelder. *Spektrale Ellipsometrie zur optischen und strukturellen Charakterisierung von amorphen Siliciumkarbid-Schichtsystemen*. Master thesis, Albert-Ludwigs-Universität Freiburg (2010).

[164] S. G. Lee, Y. J. Kim, S. P. Lee, H.-S. Oh, L. Seung Jae, M. Kim, I.-G. Kim, J.-H. Kim, H.-J. Shin, D. Hong, H.-D. Lee, and H.-K. Kang. Low Dielectric Constant 3MS α-SiC:H as Cu Diffusion Barrier Layer in Cu Dual Damascene Process. In: *Japanese Journal of Applied Physics* **40** (4S), p. 2663 (2001).

List of Publications

Peer-reviewed Journal Articles (Main Author):

C. Weiss, M. Schnabel, A. Reichert, P. Löper, and S. Janz
Structural and optical properties of silicon nanocrystals embedded in silicon carbide: Comparison of single layers and multilayer structures
In: *Applied Surface Science* **351**, p. 550 (2015)

C. Weiss, M. Schnabel, S. Prucnal, A. Reichert, J. Hofmann, T. Fehrenbach, W. Skorupa, S. Janz
Formation of Silicon Nanocrystals in Silicon Carbide Using Flash Lamp Annealing
In: *Journal of Applied Physics* **120**, p. 105103 (2016)

Peer-reviewed Journal Articles (Co-Author):

D. Hiller, A. Zelenina, S. Gutsch, S. A. Dyakov, L. López-Conesa, J. López-Vidrier, S. Estradé, F. Peiró, B. Garrido, J. Valenta, M. Kořínek, F. Trojánek, P. Malý, M. Schnabel, **C. Weiss**, S. Janz, M. Zacharias
Absence of quantum confinement effects in the photoluminescence of Si_3N_4-embedded Si nanocrystals
In: *Journal of Applied Physics* **115** (20), p. 204301 (2014)

J. Laube, S. Gutsch, D. Hiller, M. Bruns, C. Kübel, **C. Weiss**, M. Zacharias
Formation of size controlled silicon nanocrystals in nitrogen free silicon dioxide matrix prepared by plasma enhanced chemical vapor deposition
In: *Journal of Applied Physics* **116** (22), p. 223501 (2014)

M. Schnabel, **C. Weiss**, M. Canino, T. Rachow, P. Löper, C. Summonte, S. Mirabella, S. Janz, P. R. Wilshaw
Boron diffusion in nanocrystalline 3C-SiC
In: *Applied Physics Letters* **104** (21), p. 213108 (2014)

A. Zelenina, A. Sarikov, D. M.Zhigunov, **C. Weiss**, N. Zakharov, P. Werner, P. L. López-Conesa, S. Estradé, F. Peiró, S. A. Dyakov, M. Zacharias
Silicon nanocrystals in SiN_x/SiO_2 hetero-superlattices: The loss of size control after thermal annealing
In: *Journal of Applied Physics* **115** (24), p. 244304 (2014)

N. Milenkovic, M. Drießen, **C. Weiss**, S. Janz
Porous silicon reorganization: Influence on the structure, surface roughness and strain
In: *Journal of Crystal Growth* **432**, p. 139-145 (2015)

M. Schnabel, M. Canino, S. Kühnhold-Pospischil, J. López-Vidrier, T. Klugermann, **C. Weiss**, L. López-Conesa, M. Zschintzsch-Dias, C. Summonte, P. Löper, S. Janz, and P. R. Wilshaw
Charge transport in nanocrystalline SiC with and without embedded Si nanocrystals
In: *Physical Review B* **91** (19), p. 195317 (2015)

M. Schnabel, **C. Weiss**, P. Löper, P. R. Wilshaw, and S. Janz. Self-assembled silicon nanocrystal arrays for photovoltaics
In: *physica status solidi (a)* **212** (8), p. 1649 (2015)

A. Zelenina, A. Sarikov, S. Gutsch, N. Zakharov, P. Werner, A. Reichert, **C. Weiss**, M. Zacharias
Formation of size-controlled and luminescent Si nanocrystals from SiO_xN_y/Si_3N_4 hetero-superlattices
In: *Journal of Applied Physics* **117** (17), p. 175303 (2015)

S. Gerke, H. W. Becker, D. Rogalla, F. Singer, N. Brinkmann, S. Fritz, A. Hammud, P. Keller, D. Skorka, D. Sommer, **C. Weiss**, S. Flege, G. Hahn, R. Job, B. Terheiden
Influence of post-hydrogenation upon electrical, optical and structural properties of hydrogen-less sputter-deposited amorphous silicon
In: *Thin Solid Films* **598**, p. 161-169 (2016)

Conference Contribution:

C. Weiss, M. Rumpel, M. Schnabel, P. Löper, and S. Janz
Novel Silicon Nanocrystal Materials for Photovoltaic Applications
In: *Proceedings of the 28th European PV Solar Energy Conference and Exhibition*

Conference Talks:

C. Weiss, M. Schnabel, A. Reichert, P. Löper, S. Janz
Solid Phase Crystallisation Processes of Silicon Nanocrystals Embedded in a Silicon Carbide Matrix
IEEE NMDC, Acicastello, Italy (2013)

C. Weiss, M. Schnabel, P. Löper, S. Janz
Crystallisation Process of Silicon Nanocrystals Embedded in Silicon Carbide
EMRS Spring Meeting, Lille, France (2014)

C. Weiss, A. Reichert, J. Hofmann, S. Janz
Preparation of Silicon Nanocrystals in Silicon Carbide by a Multilayer Approach
DPG conference, Regensburg, Germany (2016)

Conference Posters:

C. Weiss, M. Rumpel, M. Schnabel, P. Löper, S. Janz
Novel Silicon Nanocrystal Materials for Photovoltaic Applications
EU PVSEC, Paris (2013)

C. Weiss, M. Schnabel, A. Reichert, P. Löper, S. Janz
Structural and Optical Properties of Silicon Nanocrystals Embedded in Silicon Carbide: Comparison of Single- and Multilayer Structures
EMRS Spring Meeting, Lille, France (2015)

Danksagung

Ganz herzlich möchte ich Prof. Carsten Ronning danken, dass er die Betreuung meiner Dissertation vom fernen Jena aus übernommen hat. Dein interessierter und unvoreingenommener Blick auf meine Arbeit hat immer wieder für neue Ideen gesorgt.

Genauso herzlich bedanke ich mich bei Dr. Stefan Janz für die ausgezeichnete Betreuung am ISE. Danke für die große Freiheit, die ich hatte und deine stete Bereitschaft für ausführliche Quantenknödeldiskussionen. Deinem scheinbar unbegrenzter Optimismus konnte ich mich auch in komplizierteren Phasen der Doktorarbeit nicht entziehen.

Ich danke meinen Doktoranden-Kollegen Manuel Schnabel und Philipp Löper, die mir sowohl den Einstieg in die Welt der Nanokristalle als auch den Anfang in der neuen Stadt sehr erleichtert haben. Vielen Dank für die vielen Fragen, die ihr mir beantwortet habt; die langen Diskussionen, die wir geführt haben und für eure Leidenschaft für die Wissenschaft, die ansteckend war.

Ein herzlicher Dank und nochmal ein großes Lob geht an meine Bachelorstudenten Matthias Rumpel und Tobias Fehrenbach, sowie an meine Masterstudenten Andreas Reichert und Johannes Hofmann. Ihr wart – aller Statistik zum Trotz – alle vier ganz wunderbare, kluge, selbstständige, motivierte Traum-Studenten. Eure Arbeiten haben mir nicht nur inhaltlich bei meiner Doktorarbeit geholfen, sondern euer Dasein hat die Arbeitszeit schöner, lustiger und sinnvoller gemacht.

Genauso bedanke ich mich bei meiner HiWine Gina Kraft, die mir durch ihre erstaunliche Schnelligkeit, Zuverlässigkeit und Fröhlichkeit bei vielen Messungen eine große Hilfe war.

Ein Dank an das ganze Silicium-Epitaxie-Team, das immer stets bemüht war um die Integration von uns Nanokristall-Exoten.

Bei Christian Schetter und Harald Steidl bedanke ich mich herzlich dafür, dass sie immer sofort zur Stelle waren, wenn die Anlagen nicht so wollten, wie ich. Ohne euch hätte ich in vier Jahren Doktorarbeit nicht viel zustande bekommen.

Ich danke Björn Debowski für den kompetenten und liebevollen Umbau des Sinterofens, der mir über vier Jahre zuverlässig sehr gute Dienste geleistet hat.

Dank an Jutta Zielonka für die vielen Schichtdickenmessungen am REM und an Michaela Winterhalder fürs Lasern und für viele schöne Kaffeepausen.

Ich danke unseren Chemikern Toni Leimenstoll, Felix Schätzle, Philipp Barth, Mira Kwiatkowska und Rainer Neubauer für die unzähligen Reinigungen meiner Proben.

Ein ganz großer Dank auch an das ganze Mittagspausen-Laufteam. Laut meiner Rechnung habe ich während meiner Doktorarbeit ca. 180 schöne Stunden mit euch im Mooswald verbracht und dort Energie für den Rest des Tages gesammelt.

Ich danke auch meinen geliebten Mitbewohnern aus der Riesen-WG. Ihr wart mir vor allem im Doktorarbeits-End-Zustand eine große Hilfe durch eure Gelassenheit, was mein unregelmäsiges Erscheinen und die sporadische Erfüllung des Putzplans angeht und dadurch, dass ich quasi zu jeder Tages- und Nachtzeit jemanden antreffen konnte, der mich ohne viel zu fragen mit einem Bier und einer entspannten Unterhaltung versorgt hat.

Ganz herzlich danke ich meinem Freund, der meinem Tun am ISE gegenüber immer sehr wohlwollend ist und sich auch hin und wieder geduldig erklären lässt, was wir dort tun. Danke, dass du mich in der Schreibphase sehr unterstützt hast durch deine Geduld, dein Einfühlungsvermögen, motivierendes Zureden und viel gutes Essen.

Ich möchte meinen lieben Eltern danken, die das ganze Projekt "Physikstudium" von Anfang bis Ende finanziell und mental unterstützt haben. Ihr seid das Fundament in meinem Leben, auf dem ich fröhlich Luftschlösser, Baumhäuser und Zelte bauen kann.

Herzlichen Dank an die Evangelische Studienstiftung Villigst für die finanzielle Unterstützung durch ein Promotionsstipendium.

Ehrenwörtliche Erklärung

Ich erkläre hiermit ehrenwörtlich, dass ich die vorliegende Arbeit selbständig, ohne unzulässige Hilfe Dritter und ohne Benutzung anderer als der angegebenen Hilfsmittel und Literatur angefertigt habe. Die aus anderen Quellen direkt oder indirekt übernommenen Daten und Konzepte sind unter Angabe der Quelle gekennzeichnet.

Bei der Auswahl und Auswertung folgenden Materials haben mir die nachstehend aufgeführten Personen in der jeweils beschriebenen Weise unentgeltlich geholfen:

1. M.Sc. Andreas Reichert im Rahmen seiner unter meiner Betreuung angefertigten Masterarbeit, durch die gemeinsame Bearbeitung der im Abschnitt 4.1 dargestellten Fragestellung,
2. B.Sc. Tobias Fehrenbach im Rahmen seiner unter meiner Betreuung angefertigten Bachelorarbeit, durch die gemeinsame Bearbeitung der im Abschnitt 4.3 dargestellten Fragestellung,
3. B.Sc. Johannes Hofmann im Rahmen seiner von mir aktuell betreuten Masterarbeit, durch die gemeinsame Bearbeitung der im Abschnitt 4.4.3 dargestellten Fragestellung.
4. Dr. Stefan Janz als Betreuer meiner Doktorarbeit am Fraunhofer ISE.

Weitere Personen waren an der inhaltlich-materiellen Erstellung der vorliegenden Arbeit nicht beteiligt. Insbesondere habe ich hierfür nicht die entgeltliche Hilfe von Vermittlungs- bzw. Beratungsdiensten (Promotionsberater oder andere Personen) in Anspruch genommen. Niemand hat von mir unmittelbar oder mittelbar geldwerte Leistungen für Arbeiten erhalten, die im Zusammenhang mit dem Inhalt der vorgelegten Dissertation stehen.

Die Arbeit wurde bisher weder im In- noch im Ausland in gleicher oder ähnlicher Form einer anderen Prüfungsbehörde vorgelegt.

Die geltende Promotionsordnung der Physikalisch-Astronomischen Fakultät ist mir bekannt.

Ich versichere ehrenwörtlich, dass ich nach bestem Wissen die reine Wahrheit gesagt und nichts verschwiegen habe.

Freiburg, den 10. Februar 2017 ....

Lebenslauf

Persönliche Daten

Name	Weiss
Vorname	Charlotte
Geburtsdatum	05.12.1985
Geburtsort	Nagold
Nationalität	Deutsch

Ausbildung

1992-1996	Grundschule Nagold-Kernen
1996-2000	Otto-Hahn-Gymnasium, Nagold
2000-2005	Martin-Gerbert-Gymnasium, Horb am Neckar
2005	Allgemeine Hochschulreife Abiturnote: 1,4
10/2005-06/2012	Friedrich-Schiller-Universität, Jena Studium der Physik
09/2008-07/2009	École superieure de physique et de chimie industrielles Paris, Frankreich Auslandsstudium (Erasmus)
13.06.2012	Physik Diplom, Friedrich-Schiller-Universität, Jena Gesamtnote: 1,2
10/2012-01/2017	Doktorarbeit am Fraunhofer-Institut für Solare Energiesysteme ISE Freiburg
07/2013-06/2016	Promotionsstipendium des Evangelischen Studienwerkes Villigst
seit 07/2016	Wissenschaftliche Mitarbeiterin am Fraunhofer-Institut für Solare Energiesysteme ISE, Freiburg

Freiburg, den 10. Februar 2017 ....